AN INVESTIGATION OF A TWO-DIMENSIONAL PROPULSIVE LIFTING SYSTEM

Thesis by

Carl A. Shollenberger

In Partial Fulfillment of the Requirements

For the Degree of

Doctor of Philosophy

California Institute of Technology

Pasadena, California

1971

(Submitted May 19, 1971)

ACKNOWLEDGEMENTS

The author expresses his gratitude to Dr. P. B. S. Lissaman and Professor Lester Lees for their guidance in the completion of this work. Additionally, he thanks Professor Gordon Harris for his constructive suggestions pertaining to the experimental investigation. He also recognizes the financial support of the experimental study by the National Aeronautics and Space Administration, Ames Research Center.

ABSTRACT

Several aspects of the nonhomogeneous flow associated with a system combining lifting and propulsive requirements of an aircraft are considered in detail by analytical and experimental methods. The basic geometry of the problem is that of two lifting surfaces with an actuator disk located between them. The resulting flow consists of two regions of different total energies.

Propulsive lift systems are prototypes of many similar multi-energy flow problems. The principles governing flow with energy addition are examined. Basic equations and boundary conditions are developed for the complete inviscid and incompressible analysis for the two-dimensional case. The corresponding flow singularities are discussed and the integral equations which completely specify the system are derived.

The two special cases of small and large energy addition are considered in detail including solutions.

A numerical procedure is developed to solve the full problem including allowance for the wake deflection. Appropriate vorticity forms are used to represent the entire system. Wake vorticity is provided the freedom to move in the plane. An iterative scheme is presented which rapidly converges to a solution for the magnitude and location of the system vorticity distributions. Forces and moments are evaluated on the propulsive lift system.

Analytical results are given from the numerical solution for various values of the geometric and energy parameters. Comparison of the numerical result with the solutions for extreme values of

energizing is given.

Results from a wind tunnel study of the two-dimensional propulsive-lift system provide a check on the importance of real effects. Comparison of the analytical and experimental results is given in detail. The experimentally determined wake development is observed to be similar to the predicted shape. In addition, the lift augmentation is similar for the theoretical and experimental cases. Further, the airfoil pressure distributions and resulting pitching moments are seen to exhibit the behavior expected from the calculations.

TABLE OF CONTENTS

PART	TITLE	PAGE
I.	INTRODUCTION	1
II.	THEORETICAL ANALYSIS	5
	A. Principal Assumptions and Considerations	5
	B. Basic Equations and Boundary Conditions	8
	C. Equivalent Singularities in the Flow	12
	D. Some Areas of Special Interest	16
	1. Trailing Edge	16
	2. Leading Edge	17
	3. Downstream Conditions	17
	E. Linearized Solution	20
	F. Solution for Large Energy Addition	25
	G. Numerical Solution of the Nonlinear Problem	28
	1. General Procedure	28
	2. Vorticity Distributions	32
	3. Calculation of Vorticity Strengths	37
	4. Wake Shape Calculation	40
	5. Special Points of the Numerical Solution	41
	6. Force and Moment Evaluation	42
	7. Convergence Test	44
	8. Control Points and End Points	44
	9. Performance of the Procedure	45
	H. Presentation of Results	47

Table of Contents (Cont'd)

Part	Title	Page
	1. Numerical Solution	47
	2. Wake Deflection	50
	3. Comparison of Solutions	51
	4. Variations in Airfoil Geometry	53
III.	EXPERIMENTAL INVESTIGATION	55
	A. Wind Tunnel Model	55
	B. Experimental Measurements	59
	C. Presentation of Results	63
	D. Comparison of Experimental and Calculated Results	70
	REFERENCES	72
	LIST OF FIGURES	74
	FIGURES	77

I. INTRODUCTION

Incorporation of the propulsive and lifting requirements of an aircraft into a single integrated unit appears to be a natural evolutionary step in aviation development. With the development of efficient and compact engines, new aircraft configurations are now feasible which combine the lifting and propulsive functions that have traditionally been isolated. An example of this trend is the location of the thrust engines in spanwise positions within the aircraft wing. This proposal requires analysis which takes into account the interaction between the lift and thrust producing components. This is in contrast to conventional arrangements where the relationship of the two functions is largely ignored.

The propulsive lift system offers numerous possible advantages over other wing and engine arrangements. These include beneficial interaction between the high energy wake and the wing, lower wetted surface area than conventional engine nacelles, high subsonic cruise speeds, and structural advantages. Consequently desirable V/STOL characteristics may be obtained by the use of a propulsive lift system.

This is the foundation for the development of the propulsive wing. The basic concept is but one of many ideas conceived to employ the large thrust available from the turbine engine. Associated devices are ducted propellers and fan-in-wing designs. Several propulsive lift configurations have been investigated. Common to all of these proposals is the interaction of the energized jet wake with the wing-like components of the systems.

The history of propulsive lift system development is rather brief. Theoretical attention has been given to ducted propellers and fan-in-wing designs, and a good presentation of these analyses is presented in references 1 and 2. However only very approximate theoretical and experimental results are available for either of these problems. Also, there is evidently a total lack of theoretical analysis on the present problem. Considerable attention has been devoted in reference 3 to configuration studies of possible application of propulsive wings. Figure 1 illustrates an aircraft design which employs the propulsive lift system.

References 4, 5 and 6 give further details of various features of propulsive wing systems. Furthermore, reference 7 considers a particular propulsive wing concept and considers some geometric and aerodynamic factors. Additionally wind tunnel results for this model are presented and analyzed. However the data included are limited, and no attempt is presented to describe the system analytically.

We observe that the application in figure 1 has highly significant three-dimensional characteristics as would most applications of propulsive lift systems. The present analysis is primarily concerned with a two-dimensional system but a few remarks about the three-dimensional system are necessary before proceeding. Many analyses of a wing in a propeller slipstream have been proposed. This problem is similar to the propulsive wing since the interaction of the high energy wake with a solid surface is involved. In reference 8, Jameson gives a linear analysis of the problem which neglects

the wake deflection and deformation. Also Levinsky et al. have considered what they term an exact analysis in reference 9. However both developments have neglected the important matter of the downstream wake shape. It has not been demonstrated that any self similar wake shape exists in this nonhomogeneous flow. This point of difficulty is avoided in the two-dimensional case where we can determine the downstream behavior simply.

These analyses of the three-dimensional problem illustrate the basic difficulty in solving this type of multi-energy problems. The downstream deflection of the wake and its correspondingly changing shape must be included to analyze the problem completely. The lack of advance knowledge of the wake boundary location makes application of the wake boundary conditions difficult. Two boundary conditions are applicable on the wake boundary of unknown location. The first, a kinematic condition, requires flow to be tangential to the wake boundary. This simply prevents flow through the wake boundary which is a streamline. The second boundary condition is a dynamic condition that specifies pressure continuity through the wake boundary.

As a result of these two boundary conditions, two integral equations are required to specify the system vorticity. The first results from the kinematic boundary condition and is similar to the integral equation for the vorticity of a single isolated airfoil. The second integral relation results from the dynamic condition of pressure continuity across the wake boundary. The solution of this

set of equations specifies the vorticity of the system and its location.

Attempts to eliminate this difficulty by assumption of the jet shape have proven useful in thin jet analysis. In references 10 and 11 Spence considers the thin jet assumption and determines a boundary condition to specify a single wake vorticity. Here the kinematic condition of tangential flow is eliminated by assuming the jet to lie directly behind the airfoil. The thinness of the wake allows a single vorticity to adequately represent the two boundary vorticities.

Similar attempts of simplification are of little use in the present problem since the jet is in general thick with a width of the same order as the airfoil separation. Consequently representation of the jet by a single centerline vorticity is less adequate for the thick jet than in the thin wake case. Similarly we will see that assumptions about the location of the jet boundary are of little use except in the case of high wake energizing.

With these considerations in mind we confine ourselves presently to a more restrictive problem than the three-dimensional case. Since no satisfactory solution exists for the two-dimensional problem, it is likely that some basic influences of the various parameters of this problem can be determined by considering this limit. We also note that the two-dimensional problem is a model of the general class of nonhomogeneous flows. Consequently techniques and considerations relevant to this problem apply to all flows which have regions of different total energy.

II. THEORETICAL ANALYSIS

The basic geometry of the problem we now consider is shown in figure 2. It includes two lifting surfaces which in general can be of arbitrary shape and are separated by a distance h. Somewhere between these surfaces an actuator surface is located. The outside flow of course is not energized while the flow which passes through the disk receives additional energy. Consequently we have multi-energy flow in the region aft of the airfoils.

A. Principal Assumptions and Considerations

Two-dimensional propulsive lifting systems are prototypes of the nonhomogeneous class of flows. We consider an inviscid and incompressible approach to the analysis of these systems. Clearly justification is required for each of these assumptions. It is noted however that this approach has been found useful in the analysis of the jet flap and classical propeller analysis which are problems of somewhat similar characteristics. The present problem is similar to the jet flap since it is a lifting element influenced by a downstream wake. In contrast the propeller, although nonlifting, has a thick wake similar to the propulsive lift system.

Viscous effects may indeed be important considerations to this problem as the unusual pressure distributions that can be anticipated to result from the interaction of the various components of the system, may induce separation of the flow from the lifting surfaces. Even without separation entrainment of flow by the jet wake may have a significant effect.

The assumption of incompressibility implies low flow velocities in the system. It must be realized that significant compressibility effect may be encountered even at low flight speeds if the energy addition to the wake is large. In addition, applications of the propulsive lift systems would likely involve high subsonic cruise speeds. Thus we see that real effects may be important, but in the absence of any idealized solution we proceed to consider the inviscid and incompressible case which is a practical case for low speed flight.

An idealized actuator disk is assumed as the position of discontinuity in total head. Here energy is supplied to the portion of the flow passing through the disk in the form of a pressure difference which is subsequently converted into kinetic energy. At the actuator line the pressure is discontinuous while the velocity is continuous through the disk. Uniform energy addition is assumed so that all the flow in the energized region has the same total energy. This is necessary for the flow to be irrotational. The actuator line may be any line perpendicular or oblique to the flow. The actual location of the actuator between the lifting surfaces is not important since the field equation and boundary conditions can be specified independently of this location.

Two parameters may be used to describe the energy addition to the flow. The more natural measure is the change in total head across the actuator, ΔH. When normalized by the free stream dynamic pressure this becomes the energy addition parameter,

$$C_H = \frac{\Delta H}{\frac{1}{2} \rho U^2} \quad . \tag{1}$$

A more commonly used, but less suitable parameter for this problem is the jet momentum coefficient. This is simply the jet momentum normalized by the dynamic pressure and the airfoil chord

$$C_J = \frac{\rho_J \delta_J V_J^2}{\frac{1}{2} \rho U^2 c} \quad . \tag{2}$$

Here ρ_J, δ_J, and V_J are the jet density, thickness, and velocity respectively.

Either of these parameters fully describes the energy supplied at the actuator. We will consider the relation between them later but note that zero energy addition does not correspond to zero jet momentum. The parameter C_J is often used in jet flap theory for the case of zero jet mass but finite jet momentum, J, or

$$\delta_J = \frac{J}{\rho_J V_J^2} \tag{3}$$

$$\rightarrow 0 \quad \text{as} \quad V_J \rightarrow \infty \quad .$$

Hence for jet flap analysis, a momentum source of zero mass is analyzed. In the present problem the jet always contains a finite mass as well as momentum, and thus the parameter C_J of the usual jet flap analysis sense does not adequately describe the wake.

B. Basic Equations and Boundary Conditions

We have assumed that the flow both in the jet and in the outer flow is incompressible. Further, by Kelvin's theorem we know that for both of the flows $\zeta = 0$ since the flows are inviscid and incompressible. Thus the outside flow is irrotational since we have a uniform flow at upstream infinity for which $\zeta = 0$. Similarly the wake flow is irrotational since we have specified uniform energy addition through the actuator disk. Thus we are assured of irrotational flow in both regions of the problem.

Consequently we have incompressible and irrotational flow in all parts of the flow, and we can define a velocity potential and stream function so that the velocity outside the wake is

$$\vec{V}_o = \nabla \phi_o \tag{4}$$

and the velocity inside the wake is

$$\vec{V}_i = \nabla \phi_i \tag{5}$$

As a further consequence of the incompressibility and irrotationality of both regions we know that the velocity potential and stream function satisfy Laplace's equation. Hence we have the field equations

$$\nabla^2 \phi_o = 0 \tag{6}$$

$$\nabla^2 \phi_i = 0 \tag{7}$$

Now we consider the boundary conditions. We have the usual

condition of uniform flow at infinity in each region. The conditions of the wake at downstream infinity are important and are fully discussed in section D. Briefly, the wake far downstream approaches a uniform but higher than free-stream value of velocity.

The jet angle decreases downstream as a result of decreasing influence of the wing surfaces. The induced vertical velocity is

$$v \sim \frac{-1}{x} .$$

Consequently the jet angle far downstream is

$$\alpha_J \sim \frac{-1}{x} .$$

This shows that the jet asymptotically approaches $y = -\infty$ since

$$y_J \sim \int_0^\infty v\, dx$$

$$\sim \int_0^\infty \frac{1}{x}\, dx$$

which is unbounded. Thus although the jet slope $\to 0$ as $x \to \infty$, the jet location is approaching $y = -\infty$.

At all solid surfaces the flow must satisfy the inviscid boundary condition of tangential flow

$$\phi_n = 0 , \qquad (8)$$

However the flow conditions on the free boundaries of the jet wake introduce the difficulty to this problem. We have two regions of flow with special conditions at their interface. First we have the kinematic condition given above, since the flow must be tangential

to the jet boundary as a result of its being a streamline in the flow. A second, dynamic condition must be introduced to assure no pressure difference between the two regions. Outside the wake Bernoulli's equation for incompressible flow gives

$$P_s + \frac{1}{2}\rho V_o^2 = H_o \quad . \tag{9}$$

Similarly inside the jet we have

$$P_s + \frac{1}{2}\rho V_i^2 = H_o + \Delta H \tag{10}$$

where ΔH is the change in total pressure change as the flow passes through the actuator.

The static pressure is continuous across the jet boundary and hence, elimination of H_o yields

$$\frac{1}{2}\rho V_i^2 = \frac{1}{2}\rho V_o^2 + \Delta H \quad . \tag{11}$$

This then is the dynamic condition to be satisfied on the jet boundaries. The various boundary conditions are indicated in figure 3.

It should be observed that we have prescribed the field equation and the boundary conditions of the entire system without specification of the actual location of the actuator disk other than requiring it to be between the solid surfaces. Consequently we see that kinematically, the energizing position is unimportant. Of course the detailed pressure distribution on the lifting surfaces is dependent on the actuator position. However in general the net force on this propulsive lift system will be totally independent of the actuator location since the external flow field is not dependent on this position.

This result is due to only a total pressure change occurring as flow passes through the actuator. If, for example, mass were also injected at this position, the location of mass addition would be important to the flow solution. It is easily seen that slanting of the actuator does not result in any change in the net force since the difference in the forces on the solid surfaces is canceled by the change in the actuator force and direction. Thus we conclude that both the wake and outer flows and the net force on the system are completely independent of the actuator position.

C. Equivalent Singularities in the Flow

The entire propulsive lifting system can be replaced by a uniform flow with embedded singularities. This equivalent representation results from the field equation and boundary conditions.

First we have the usual set of singularities used to represent a two-dimensional lifting body. These are distributions of sources and vorticity located so that they are within or on the boundary of the surface. The strengths of these singularities are such that the resultant flow satisfies the kinematic boundary condition on each of the surfaces. For the case of flat plates, we require only vorticity on the chordline of the plates.

The nature of the wake singularities is determined by further examination of the dynamic boundary condition. Simple rearrangement of equation 11 yields

$$V_i - V_o = \frac{\Delta H/\rho}{\overline{V}} \quad , \tag{12}$$

where $\overline{V}$ is the average of the velocities on the two sides of the jet boundaries. Hence we see that there is a discontinuity in the velocity across the wake boundary. This indicates that a vortex sheet can be used to replace this interface. The strength of the sheet at any point along the boundary is simply

$$\gamma = \frac{\Delta H/\rho}{\overline{V}} \quad . \tag{13}$$

The location of the vortex sheet is an important consideration. The wake kinematic condition gives the jet shape. The tangential flow condition is,

$$\frac{d\, y_w}{d\, x} = \frac{v}{U + u} \tag{14}$$

where y_w is the ordinate of the wake boundary and x is in the direction of the main stream flow. Integration with respect to x yields

$$y_w(x) = y_a + \int_{x_a}^{x} \frac{v(x)}{U + u(x)}\, dx \quad . \tag{15}$$

Here (x_a, y_a) is the position of the trailing edge of the airfoils. Equation 15 specifies the boundary of the wake. Of course two wake boundaries exist and the upper and lower interfaces are each specified by application of this equation. The velocity perturbations u and v are not known and hence the wake shape is unknown. Thus we cannot specify the position of the wake vorticity which is located on the wake boundary.

We have replaced the entire propulsive lift system with an appropriate set of singularities at the proper locations. Consider the case of a flat plate system. The velocity at any point in the plane resulting from an embedded vorticity element is given by application of the Biot-Savart law as

$$dV = \frac{\gamma \sin \theta\, d\ell}{4 \pi r^2} \tag{16}$$

where r is the distance between the point of induced velocity and the vorticity element. Also γ is the vorticity strength, $d\ell$ is the length of the element and θ is the angle between the vorticity element and the line connecting the element and the point in the plane.

From this we determine the u and v velocity components resulting from the airfoil and wake vorticity as.

$$u(x, y) = \int_o^\infty \gamma_u F_x \, ds + \int_o^\infty \gamma_\ell F_x \, ds \tag{17}$$

and

$$v(x, y) = \int_o^\infty \gamma_u F_y \, ds + \int_o^\infty \gamma_\ell F_y \, ds \quad . \tag{18}$$

Here subscripts u and v designate the upper and lower parts of the system. Also F_x and F_y are geometric functions which are independent of the embedded vorticity strength or.

$$F_x = F_x(x, y, s) \tag{19}$$

and

$$F_y = F_y(x, y, s) \quad . \tag{20}$$

In these relations s is a coordinate along the lifting surface and wake boundary.

Now we use the kinematic and dynamic boundary conditions, equations 13 and 14, to develop a set of integral relations. First the kinematic condition yields

$$\int_o^\infty \gamma_u F_y \, ds + \int_o^\infty \gamma_\ell F_y \, ds = \left[U + \int_o^\infty \gamma_u F_x \, ds + \int_o^\infty \gamma_\ell F_x \, ds\right] \frac{dy}{dx} \quad . \tag{21}$$

This applies to each lifting surface, or

$$\begin{aligned} y &= y_{s_u}(x) \qquad 0 \le x \le c_u \\ y &= y_{s_\ell}(x) \qquad 0 \le x \le c_\ell \quad . \end{aligned} \tag{22}$$

Similarly equation 21 applies along each wake boundary or

$$y = y_{w_u}(x) \qquad \forall x \geq c_u$$
$$y = y_{w_\ell}(x) \qquad \forall x \geq c_\ell \qquad (23)$$

Also from the dynamic boundary condition of pressure continuity across the jet boundary we obtain

$$\gamma_w(x_w, y_w)\left[(U + \int_0^\infty \gamma_u F_x\, ds + \int_0^\infty \gamma_\ell F_x\, ds)^2 + (\int_0^\infty \gamma_u F_y\, ds + \int_0^\infty \gamma_\ell F_y\, ds)^2\right]^{\frac{1}{2}} = \frac{\Delta H}{\rho}. \qquad (24)$$

This applies over the wake boundary as indicated by 23 above.

Relations 21 and 24 are integral equations which define the singularities and their locations. Solution of these equations results in specification of the strengths of all vortex sheets representing both the airfoils and the wake boundaries. In addition the wake boundary locations are determined by these equations.

D. Some Areas of Special Interest

Particular attention must be given to three parts of the propulsive lift system.

1. Trailing Edge

A condition analogous to the Kutta condition for ordinary airfoils is necessary at the trailing edges of the lifting surfaces. We require the flow at the trailing edges to leave the surfaces smoothly without a discontinuity in direction of flow. This is justified by the usual argument (see reference 12 for example) concerning the influence of viscosity. As a result of this requirement we specify that the velocity is finite at the trailing edges if these edges are cusps. An infinite velocity is required for the flow to leave a cusp trailing edge in an abrupt manner. Specification of a finite velocity ensures no flow around the trailing edge and as a consequence the flow departs smoothly.

Compliance with this Kutta condition can be met if we require that the vorticity is continuous at the trailing edge. Only a discontinuity in vorticity at the trailing edge and the beginning of the jet wake can produce an infinite velocity. Thus we require the airfoil vorticity to approach the wake vorticity value at the trailing edge to satisfy the Kutta condition for the propulsive lift system.

Reference 13 examines the Kutta condition for a considerably simplified geometry and suggests that a less restrictive condition than specified above may be appropriate. However this analysis concerns a vortex sheet between two unbounded flow regions with

one region of stagnated flow. Hence this analysis does not directly apply and for the present the usual Kutta condition will be used.

2. Leading Edge

The leading edge flow can be expected to display a behavior similar to an ordinary airfoil at angle of attack. For a flat plate we anticipate a leading edge vorticity distribution

$$\gamma \sim \frac{1}{\sqrt{x}} ,$$

since there is flow around the leading edge of the airfoil. The jet influence only induces a velocity at the airfoil so as to alter the effective angle of attack. Consequently, the behavior at the leading edge will not be expected to change in character because of the presence of the jet.

3. Downstream Conditions

The wake conditions far downstream of the lifting system can be fully determined. For the two-dimensional propulsive lift system, the wake must become parallel to the free-stream flow. Stratford in reference 14 obtained this result for the jet flap. We see this by considering a two-dimensional jet which is continuously moving downward at a finite rate. Of course all the flow above and below the wake also is moving downward since there is no flow through the wake. Further, the flow above and below the wake cannot flow around the ends of the wake as in the three-dimensional case. As a consequence we have an infinite mass of fluid per unit span transversing downwards. We have a vertical momentum per unit span of

$$J_v = Mv .$$

Application of the momentum theorem shows that for this case we have infinite lift per unit span. Hence, $v \to 0$ as $x \to \infty$. Thus we conclude that the jet boundaries must assume a position parallel with the free-stream. As previously discussed $\alpha_J \to 0$ although the jet boundary location approaches $y = -\infty$. We will continue the discussion of the asymptotic behavior of the wake in Section H.

The flow inside and outside the wake is irrotational and hence

$$\frac{\partial u}{\partial y} = \frac{\partial v}{\partial x} \quad .$$

Now far downstream $\frac{\partial}{\partial x} \to 0$ and thus $\frac{\partial u}{\partial y} \to 0$. Therefore the flows must be uniform inside and outside the wake. Outside the wake region we know the flow is at the mainstream value, U. Across the free boundary there is a jump in the velocity. From equation 12 we determine the jet velocity at downstream infinite to be

$$V_{i_\infty} = \sqrt{U^2 + 2\Delta H/\rho} \quad . \tag{25}$$

This with equation 13 gives the value of the wake vorticity at downstream infinity as

$$\gamma_\infty = \sqrt{U^2 + 2\Delta H/\rho} - U \quad . \tag{26}$$

Now it is possible to relate the parameters C_H and C_J. If the jet thickness is δ_∞ at downstream infinity, the jet momentum coefficient is

$$C_J = \frac{\rho(U^2 + 2\Delta H/\rho)\delta_\infty}{\frac{1}{2}\rho U^2 c} \tag{27}$$

or,

$$C_J = 2(1 + \Delta H / \tfrac{1}{2} \rho U^2) \frac{\delta_\infty}{c} \quad . \tag{28}$$

Thus using the definition of C_H

$$C_J = 2(1 + C_H) \frac{\delta_\infty}{c} \quad . \tag{29}$$

As noted previously, zero C_H does not correspond to zero C_J since there is always momentum in the wake.

In many theoretical studies C_J is used in the thin wake limit where $\delta \to 0$. Clearly we have

$$C_J = \frac{O(2 C_H \delta_\infty)}{c} \qquad \frac{\delta_\infty}{c} \ll 1 \quad .$$

Thus for all finite values of C_H we have the corresponding C_J equal to zero. This is the result of the zero thickness wake concept where we have a momentum source with no jet mass flow. By contrast the present case considers an actuator which adds momentum and energy to a finite mass of fluid. This is a more realistic representation of the actual thick jet wake.

E. Linearized Solution

The difficulties in obtaining a solution for the problem discussed thus far are twofold. These are the unknown wake shape and the dynamic boundary condition. Both of these difficulties introduce nonlinearity into the solution of the problem so that the solution is not a simple linear function of energy addition and angle of attack. First the jet boundary deflection introduces nonlinearity into the problem because its shape changes with variation of C_H and α. The wake shape is not known in advance and hence the correct position for application of the dynamic boundary condition is not specified. The dynamic condition involves the square of the local velocity and hence introduces the second nonlinearity. We observe that both of these difficulties must be removed in order to obtain a solution analogous to linear airfoil theory or linear jet flap theory.

Of course the lifting members of the system present nonlinearity to the system as in the case of thick airfoil analysis. However this can be handled in a manner similar to thin airfoil theory by placing the singularities that represent the lifting surfaces on mean lines and linearizing the tangential flow conditions. The approximation has proven useful in airfoil theory for thin airfoils at small angles of attack.

We now consider a linearization of the boundary conditions that will apply for small angle of attack and small energy additions. Writing the velocity components as U + u and v, where u and v are perturbations, equation 11 becomes

$$2U(u_i - u_o) + u_i^2 + v_i^2 - u_o^2 - v_o^2 = \frac{2\Delta H}{\rho} \quad . \tag{30}$$

The subscripts i and o refer to the properties inside and outside the jet. Neglecting second order terms, this is

$$u_i - u_o = \frac{\Delta H}{\rho U} \quad . \tag{31}$$

This indicates that there is a vortex sheet of constant strength at the jet boundaries. Now we further assume that the jet deflection is small for the present case and apply the above condition on mean lines directly behind the airfoils on the lines $y = \pm h/2$.

Finally, the usual linearization of the tangential flow condition on the airfoil is used.

$$y' = \frac{v}{U} \quad . \tag{32}$$

We thus have the problem shown in figure 4.

Proceeding to solve the linearized problem posed above, we observe that the boundary conditions can be separated into symmetrical and antisymmetrical parts. These are solved separately and then superimposed. This division of the problem is shown in figure 5. We consider a system with lifting surfaces of flat plate airfoils of equal chords and zero stagger.

The antisymmetrical part is just the linearized biplane problem. This was solved by Glauert in reference 15 by conformal mapping. The exact result for flat plate airfoils is

$$C_{L_A} = 4\pi B \sin\alpha \tag{33}$$

where the factor B is

$$B = \frac{\sqrt{(p^2-m^2)(m^2-q^2)}}{mc}$$

The terms p, m and q are related to the separation of the flat plates and their chord by

$$h = 2p\left[E' - \frac{p^2-m^2}{p^2}K'\right]$$

$$c = 2p\left[E(k,\tau) - \frac{m^2}{p^2}F(k,\tau)\right]$$

where

$$\tau = \sqrt{\frac{p^2-m^2}{p^2-q^2}}$$

$$k' = q/p$$

$$E' = \int_o^1 \sqrt{\frac{1-k'^2x^2}{1-x^2}}\,dx$$

$$K' = \int_o^1 \frac{dx}{\sqrt{(1-x^2)(1-k'^2x^2)}}$$

$$E(k,\tau) = \int_o^\tau \sqrt{\frac{1-k^2x^2}{1-x^2}}\,dx$$

$$F(k,\tau) = \int_o^\tau \frac{dx}{\sqrt{(1-x^2)(1-k^2x^2)}}$$

The factor B is shown in figure 6 as a function of h/c.

The symmetric part of the problem is readily solved numerically in a manner similar to the method used in reference 16 to analyze a flat plate in ground effect. We place a constant vorticity at $y = \pm\frac{h}{2}$ from x = c to downstream infinity. The magnitude of this

vorticity is given by the boundary condition of equation 31. Then we superimpose the additional vorticity

$$\gamma_a = N_o \sqrt{\frac{c-x}{x}} + \sum_{i=1}^{n-1} N_i \sin(i\theta) + \frac{\Delta H}{\rho U}, \quad x \le c \tag{34}$$

where

$$\theta = \text{ARCCOS}\left[\frac{c-2x}{c}\right] .$$

This vorticity represents the airfoil and is located on $y = \pm \frac{h}{2}$. Now we calculate the velocity induced at each of n control points on the airfoils. Compliance with the boundary condition of equation 32 gives a set of n linear equations for the coefficients N_o through N_{n-1}. Solution of these equations gives the airfoil vorticity. Notice that the Kutta condition has been satisfied since $\gamma_o \to \frac{\Delta H}{\rho U}$ as $x \to c$.

Since the system is completely symmetrical about its centerline, no net normal force on the device results from the symmetrical solution of the problem. However the leading edge singularity produces a nose thrust. The first vorticity distribution of γ_a is of the form of a flat plate at angle of attack

$$\gamma_{a_o}(x) = N_o \sqrt{\frac{c-x}{x}} . \tag{35}$$

Thus at the leading edge, $x \to 0$, we have the velocity

$$u \sim \frac{N_o}{\sqrt{x}} .$$

Application of the Blasius theorem to a vanishingly small circle at the leading edge yields a leading edge thrust of

$$C_T = 2\pi N_o^2 \quad . \tag{36}$$

We observe that N_o is linear in C_H because of the linearized dynamic boundary condition, equation 31. Hence we write $N_o = \bar{N}_o C_H$, where $\bar{N}_o$ is a function of $\frac{h}{c}$ only. The lift on the symmetric system is then

$$\begin{aligned} C_{L_s} &= C_T \sin\alpha \\ &= 2\pi \bar{N}_o^2 C_H^2 \sin\alpha \quad . \end{aligned} \tag{37}$$

Some values of $\bar{N}_o$ are given in table 1 for a flat plate airfoil system.

Now we have the total lift coefficient for the linear system as

$$C_L = \left[2\pi(2B + \bar{N}_o^2 C_H^2) + C_H \frac{h}{c}\right] \sin\alpha \quad . \tag{38}$$

The third term above is the force on the actuator resulting from the pressure discontinuity there.

F. Solution for Large Energy Addition

The case of the high energy wake is an interesting limit of the propulsive lifting device. Here the wake system dominates the entire flow to the extent that the free-stream flow is not important compared to velocities induced by the jet. Hence in this limit we have the system operating in stationary fluid. The energy addition is so large that there is no jet deflection and the wake boundaries are straight lines directly behind the airfoils. Thus the system is now a two-dimensional channel extending to downstream infinity in the chordwise direction as shown in figure 7.

We solve this flow problem in a manner similar to that outlined in reference 17. The channel is positioned with walls at $y = \pm \frac{h}{2}$ from $x = 0$ to $x = +\infty$. As $x \to \infty$, the flow within the channel approaches a uniform velocity value, U_∞, and everywhere outside the channel the flow velocity approaches zero. On the channel wall the velocity potential, ϕ, and x are related by

$$x = \frac{-h}{2\pi}\left[1 - e^{\frac{-2\pi\phi}{U_\infty h}}\right] + \frac{\phi}{U_\infty} \qquad (39)$$

Hence the velocity on the channel wall is

$$u = \frac{U_\infty}{1 - e^{-2\pi\phi/U_\infty h}} \qquad (40)$$

Note the correct behavior of u as $x \to \infty$ ($\phi \to \pm\infty$). On the outer wall surface at downstream infinity

$$u \to 0 \text{ as } \phi \to -\infty$$

$$u \to U_\infty \text{ as } \phi \to \infty$$

Thus equation 39 does provide the desired flow field.

We are concerned with the forces on the system. The pressure on the surfaces is easily determined from Bernoulli's equation and consequently the forces normal to the surfaces can be readily calculated. However, since the channel is symmetric about its centerline, there is no net force normal to the channel.

Consider now the behavior at the leading edge of the system. Here ϕ and x are very small. Thus from equation 39 we have

$$x \cong \frac{\pi \phi^2}{U_\infty^2 h} \quad \text{for} \quad \phi \ll 1 \quad . \tag{41}$$

Similarly equation 40 becomes

$$u \cong \frac{U_\infty^2 h}{2 \pi \phi} \quad . \tag{42}$$

Eliminating ϕ from these equations to obtain u(x), yields

$$u \cong \frac{U_\infty}{2} \sqrt{\frac{h}{\pi x}} \quad \text{for } x \ll 1 \quad . \tag{43}$$

We recognize the familiar square root leading edge singularity. The thrust associated with this velocity singularity is given by equation 34 as

$$T = \frac{\rho U_\infty^2 h}{4} \tag{44}$$

for each leading edge. Twice this thrust value is exerted on the total system.

The resulting lift is then

$$L = \frac{1}{2} \rho U_\infty^2 \sin\alpha \quad . \tag{45}$$

Equation 25 gives the value of U_{i_∞} for $U = 0$ as

$$U_{i_\infty} = \sqrt{\frac{2 \Delta H}{\rho}} \quad . \tag{46}$$

Thus the lift is

$$L = \Delta H \, h \sin\alpha \quad , \tag{47}$$

and the lift coefficient is

$$C_L = C_H \frac{h}{c} \sin\alpha \quad . \tag{48}$$

This obviously does not apply for small values of C_H. However, we can obtain the value of the slope of the C_L versus C_H curve as.

$$\frac{\partial C_L}{\partial C_H} = \frac{h}{c} \sin\alpha \quad . \tag{49}$$

We thus expect a linear dependence of C_L on C_H for large energy addition. This is a valuable check on any solution which predicts the performance of the propulsive lift system.

G. Numerical Solution of the Nonlinear Problem

A solution of the integral equations 21 and 24 can be determined by an iterative numerical method. The solution specifies the location and magnitude of both the airfoil and wake vorticity. We now consider the general methodology of the procedure and then concentrate on the details of various aspects of the solution. A flat plate propulsive lifting system is analyzed and later we will extend the discussion.

1. General Procedure

The method we now consider is based on the concepts we have discussed in the previous sections. We saw that the propulsive lift system can be completely replaced by embedded singularities in the free-stream flow. Hence we position the proper singularities at the correct locations to satisfy the various boundary conditions to obtain a nonlinear numerical solution.

We begin by assuming some initial state for the wake vorticity, both in strength and position. A simple approximate starting solution which works well is the linear solution of section E. We know that the airfoil vorticity is located on the chordlines of the flat plates. This vorticity is represented by various blocks of vorticity which will be of the correct form and will be discussed in detail subsequently.

The velocity induced by the airfoil vorticity on numerous airfoil control points iscalculated and stored in a matrix of influence coefficients. Then the velocity induced by the wake on the airfoil control points is determined. Now we satisfy the kinematic flow condition, equation 18, on the airfoils at each control point by specifying

the correct magnitude of vorticity which represent the airfoils. This involves the solution of a set of linear algebraic equations and corresponds to a solution of the integral equation 21. This completes the first part of one step in the iterative process.

The second part is devoted to determining the magnitude and position of the wake vorticity. We represent the wake by embedded vorticity. The vorticity representation is similar to the airfoil representation and consists of numerous blocks of the proper form. The magnitude of the vorticity in the wake is our first concern. We determine this by calculation of the velocity induced by the airfoil and wake vorticity at numerous wake control points. This permits determination of the strength of the wake vorticity at each wake control point. The wake vorticity strength for the $(\nu+1)^{th}$ iterative step follows from the dynamic wake boundary condition of equation 13 as

$$\gamma^{(\nu+1)}(x, y_w(x)) = \frac{\Delta H/\rho}{\bar{V}^{(\nu)}(x, y_w(x))} \qquad \nu = 0, 1, 2, \ldots . \qquad (50)$$

This corresponds to the solution of equation 24. The ν superscript refers to quantities determined from the ν^{th} step. The initial starting solution corresponds to $\nu = 0$.

Since we know the strength of the airfoil and wake vorticity, all that remains to be determined to fully specify the system is the wake boundary position. This results from the wake kinematic flow condition equation 14. We determine the y coordinate of the various wake control points for the $(\nu+1)^{th}$ iterative step by

$$y_w^{(\nu+1)}(x) = y_a + \int_{x_a}^{x} \frac{v^{(y)}(x')}{U + u^{(y)}(x')}\, dx' \qquad \nu = 0, 1, 2, \ldots . \quad (51)$$

This corresponds to solution of equation 21.

We observe that we have completed one cycle of an iterative process which can be repeated until a solution of sufficient convergence is obtained. This method proceeds so that $\gamma^{(\nu)}(x)$ and $\gamma^{(\nu+1)}(x)$ as well as $y_w^{(\nu)}(x)$ and $y_w^{(\nu+1)}(x)$ are nearly equal for a reasonably small ν. This indicates that the boundary conditions are closely satisfied at all control points. Thus we have obtained a method of solution by rather straightforward application of the ideas of the previous sections. We have started from an initial state which we expect approximates the actual solution. By continuously moving the wake vorticity in successive steps to points nearer to the proper wake location, we have determined a numerical solution.

Above we have mentioned that "blocks" of vorticity have been employed to represent the vortex sheets we know are present in the flow. Four differently shaped distributions are actually required to represent the airfoil and wake adequately as shown in figure 8. The first of these representations is a trapezoidal distribution. Trapezoids are used to represent much of the airfoils and wakes.

The second distribution is of the form of the loading on a flat plate airfoil at angle of attack. This is the singular part of the airfoil vorticity. The regular part of the airfoil vorticity is approximated by trapezoids. The flat plate loading is used on each of the airfoils since we observe that the influence of the other airfoil and the wake system is to effectively change the angle of attack of the

lifting flat plates. We thus expect the airfoil vorticity to have much the same character as an isolated flat plate at an angle of attack. This distribution produces the leading edge square root singularity we anticipate.

At the trailing edge the lifting flat plate vorticity approaches zero. The trapezoidal distribution is forced to approach the value of the wake vorticity just aft of the trailing edge as given in equation 26. This satisfies the Kutta condition we have specified.

Aft of the trailing edges trapezoidal elements are again used to represent the wake vorticity. We continue this for a distance of several chords downstream. Then at a point far downstream of the airfoils, the vorticity is forced to approach a constant value. This is accomplished with the use of the third distribution. This distribution is used to avoid a discontinuity in vorticity at the point where the wake is first represented by constant vorticity. The upstream vorticity is matched to the constant value of vorticity by causing the difference to decay to zero downstream. This requires a rapidly decreasing function and we choose the function $1/x$ to accomplish this matching. In practice, the mismatch is small and this distribution is not significant.

This leads us to the final vorticity distribution which is simply a constant strength vortex sheet. We have seen this to be the nature of the wake vorticity far downstream. This distribution starts at some point far aft of the airfoils and continues to downstream infinity. The induction of the far wake from both the upper and lower wake vorticity must be considered simultaneously since one of them will

produce infinite velocity everywhere if considered singly.

All vorticity is placed at its actual location in the flow instead of on a mean line as in linear theory. The vorticity location on the airfoils is fixed during all iterations but the wake vorticity is located on straight line segments which are allowed to move at each iterative step. In contrast to many numerical procedures, the control points of this scheme move with each iteration. This results from the changing wake shape and consequent change in location for the application of the boundary conditions.

This full nonlinear analysis is carried throughout the solution. For example, the force and moment evaluation is performed by determining the velocities on the airfoil surfaces. This accounts for the difference of the local velocities from the free-stream value. Also, the leading edge thrust is included in the computation.

Required inputs to the procedure are the surface geometry, energy addition, and an initial approximate solution. A constant vorticity located directly downstream of the lifting surfaces serves adequately for this starting solution. The geometry of the lifting surfaces is limited here to flat plates but can include plates of different length and different angles of attack. Other airfoil geometries are a simple extension of the present analysis and will be discussed briefly in section H.

2. Vorticity Distributions

As outlined above and shown in figure 8 , four basic distributions of vorticity are used to represent the propulsive lifting system. The velocity induction at any point in the plane is required for each

of these four distributions. The complex conjugate velocity induced at (x_p, y_p) by a vorticity distribution $\gamma(z')$ located between z_1 and z_2 is

$$q = \frac{i}{2\pi} \int_{z_1}^{z_2} \frac{\gamma(z')}{z_p - z'} \, dz' \quad . \tag{52}$$

The remainder of this subsection is concerned with the detailed induction functions of the various distributions. We give each vorticity algebraically and then prescribe the velocity it induces at an arbitrary point in the plane, (x_p, y_p). The induction is found by equation 52. The coordinate system we employ throughout the analysis is the free-stream system with positive x in the downstream direction. We place the leading edge of the upper airfoil at the origin. Often an auxiliary coordinate system is involved in the calculation of the induced velocities. This results from the location of the vorticity between arbitrary points in the plane. Since we have carried the nonlinear analysis through the entire procedure, we require expressions for the induced velocity caused by vorticity located anywhere in the plane.

First we consider the trapezoidal distribution of vorticity located on the line connecting (x_1, y_1) and (x_2, y_2)

$$\gamma_t(x) = \Gamma_{t_1} + (\Gamma_{t_2} - \Gamma_{t_1}) \left(\frac{x - x_1}{x_2 - x_1} \right) \qquad x_1 \le x \le x_2 \quad . \tag{53}$$

The velocity components induced at the point (x_1, y_1) are

$$u_t' = \frac{1}{2\pi} \left[\Gamma_{t_1} \theta + (\Gamma_{t_2} - \Gamma_{t_1}) \left(\frac{x'}{\xi} \theta - \frac{y'}{\xi} \ln R \right) \right] \tag{54}$$

$$v_t' = \frac{1}{2\pi} \left[\Gamma_{t_1} \ln R + (\Gamma_{t_1} - \Gamma_{t_2}) \left(\frac{x'}{\xi} \ln R - \frac{y' \theta}{\xi} + 1 \right) \right] \tag{55}$$

where, we have the auxiliary terms

$$R = \frac{\sqrt{(y'^2 - x'(\xi - x'))^2 + y'^2 \xi^2}}{x^2 + y^2}$$

$$\theta = \arctan\left[\frac{y'\xi}{y'^2 - x'(\xi - x')}\right]$$

$$\xi = \sqrt{(x_2 - x_1)^2 + (y_2 - y_1)^2}$$

and, the auxiliary coordinates

$$x' = (x_p - x_1)\cos\phi_t + (y_p - y_1)\sin\phi_t$$

$$y' = (y_p - y_1)\cos\phi_t - (x_p - x_1)\sin\phi_t$$

$$\phi_t = \arctan\left[\frac{y_2 - y_1}{x_2 - x_1}\right] .$$

These velocity components are in the primed coordinate system, rotated by an angle ϕ_t from the free-stream system, and must be transformed to the free-stream system by

$$u = u'\cos\phi_t - v'\sin\phi_t$$

$$v = v'\cos\phi_t + u'\sin\phi_t .$$

The second vorticity representation employed is of the form of the loading of a lifting flat plate, or,

$$\gamma_f(x'') = \Gamma_f \sqrt{\frac{1 - x''}{x''}} \qquad 0 \le x'' \le 1 . \qquad (56)$$

This distribution is located on the chordline of each airfoil which is on the abscissa of the double primed system where

$$x'' = \frac{1}{c}\left[(x-x_f)\cos\phi_f - (y-y_f)\sin\phi_f\right]$$

$$y'' = \frac{1}{c}\left[(y-y_f)\cos\phi_f - (x-x_f)\sin\phi_f\right]$$

$$\phi_f = \arctan\frac{y_b-y_f}{x_b-x_f} .$$

In the free-stream coordinate system the airfoil is located between the points (x_f, y_f) and (x_b, y_b). Thus c, the chord, is

$$c = \sqrt{(x_b-x_f)^2+(y_b-y_f)^2} .$$

In the double primed system the velocity components at (x_p, y_p) are

$$u_f'' = \Gamma_f \sqrt[4]{\frac{(1-x'')^2+y''^2}{x''^2+y''^2}}\left(\cos\frac{\theta}{2}\cos\frac{\delta}{2} + \sin\frac{\theta}{2}\sin\frac{\delta}{2}\right) \quad (57)$$

$$v_f'' = \Gamma_f\left[1 - \sqrt[4]{\frac{(1-x''^2)+y''^2}{x''^2+y''^2}}\left(\cos\frac{\theta}{2}\sin\frac{\delta}{2} - \sin\frac{\theta}{2}\cos\frac{\delta}{2}\right)\right] \quad (58)$$

where

$$\theta = \begin{cases} \arctan\left(\frac{y''}{x''}\right) + \pi & x'' \le 0 \\ \arctan\left(\frac{y''}{x''}\right) & x'' \ge 0 \end{cases}$$

$$\delta = \begin{cases} \arctan\left(\frac{-y''}{1-x''}\right) & x'' \le 1 \\ \arctan\left(\frac{-y''}{1-x''}\right) - \pi & x'' \ge 1 \end{cases} .$$

In these expressions the branch of the arctangent function between $-\pi/2$ and $\pi/2$ is used. On the line $y'' = 0$, u_f'' is zero. The velocity components must also be transformed in the free-stream system by

$$u = u'' \cos \phi_f - v'' \sin \phi_f$$

$$v = v'' \cos \phi_f + u'' \sin \phi_f \quad .$$

The third vorticity distribution is a 1/x representation to account for any difference between γ_∞ and the vorticity of the farthest downstream trapezoidal element. This is

$$\Gamma_D = \Gamma_\eta - \gamma_\infty \qquad \eta = n + m + 1 \quad .$$

Hence for the distribution

$$\gamma(x) = \Gamma_D \frac{x_\eta}{x} \qquad x \geq x_\eta \tag{60}$$

located on the abscissa, the velocity induced at (x_p, y_p) is

$$u = \frac{-\Gamma_D x_\eta}{2\pi(x^2 + y^2)} \left[x\,\theta - y \ell n \frac{R}{x_\eta} \right] \tag{61}$$

$$v = \frac{-\Gamma_D x_\eta}{2\pi (x^2 + y^2)} \left[y\,\theta + x \ell n \frac{R}{x_\eta} \right] \tag{62}$$

where

$$R = \sqrt{(x_\eta - x)^2 + y^2}$$

$$\theta = \arctan\left(\frac{-y}{x_\eta - x}\right) \quad .$$

Far downstream the vorticity approaches a constant value given by equation 26. Consequently the velocity induced by two lines of constant vorticity of strength γ_∞ is required. The lines are $y = \pm \delta_\infty/2$ from x = D to downstream infinity. The value of δ_∞ changes with each iteration as the wake deforms, and is not equal

to the airfoil separation, h.

The velocity induced by this constant distribution at (x_p, y_p) is then

$$u = \frac{\gamma_\infty}{2\pi} (\theta_1 - \theta_2) \tag{63}$$

$$v = \frac{\gamma_\infty}{2\pi} \ell n \left(\frac{R_1}{R_2}\right) \tag{64}$$

where, we have the auxiliary terms

$$\theta_1 = \arctan\left(\frac{y_p - \delta_\infty/2}{x_p - D}\right)$$

$$\theta_2 = \arctan\left(\frac{y_p + \delta_\infty/2}{x_p - D}\right)$$

$$R_1 = \sqrt{(x_p - D)^2 + (y_p - \delta_\infty/2)^2}$$

$$R_2 = \sqrt{(x_p - D)^2 + (y_p + \delta_\infty/2)^2} \quad .$$

The four vorticity distributions are superimposed to yield a general representation of the airfoil and wake systems.

3. Calculation of Vorticity Strengths

The induction functions of the previous subsection provide easy calculation of the velocity induced at any point in the plane by the embedded vorticity representing the airfoil and wake systems. We now use these induction functions to determine the airfoil and wake vorticity strengths from the appropriate boundary conditions.

The kinematic boundary condition on the airfoils is

$$v = (1+u)\, y' \quad . \tag{65}$$

Here the velocity components are normalized with respect to the free-stream velocity. The velocity components, u and v, are composed of two parts. First there is u_a and v_a resulting from the airfoil vorticity. Secondly, we have u_w and v_w induced by the wake systems. Thus the tangential flow condition becomes

$$v_a - u_a y' = (1+u_w)y' - v_w \quad . \tag{66}$$

Since the airfoil control points and vorticity locations remained fixed for all iterations, the effect of the various vorticity distributions on the lifting surfaces can be determined and stored for use during the entire process. These influence coefficients are stored in a matrix, C, defined so that

$$v_{a_i} - u_{a_i} y'_{ij} = C_{ij}\, \gamma_{a_j} \quad . \tag{67}$$

Here y'_i is the slope of the surface at the i^{th} control point and γ_{a_j} is the value of the j^{th} vorticity distribution on the airfoils. Also u_{a_i} and v_{a_i} are the airfoil induced velocity components at the i^{th} airfoil control point.

The first n-1 terms of γ_a are the magnitudes of the vorticity elements on the upper surface. These include a flat plate vorticity distribution and 2(n+1) trapezoidal distribution values as shown in figure 10. Similarly the second n-1 elements of the vector γ_a correspond to the vorticity on the lower airfoil. There are n-1 control points on each airfoil. Thus C is a 2(n-1) by 2(n-1) matrix of influence coefficients for use in satisfying the tangential flow condition on the airfoil surfaces.

If we satisfy the condition of equation 66 at each of the control points on the two airfoils we have the system of equations

$$C_{ij}\,\gamma_{a_j} = (1 + U_i)y_i' - V_i \quad . \tag{68}$$

This is a system of 2(n-1) linear equations to determine the present iteration's values of γ_{a_j} on the airfoils. We have thus defined the vorticity on the two airfoils for this step. This completes the first phase of each iterative step and now attention is given to the calculation of the wake vorticity and shape.

The wake representation is shown in figure 11. There are m control points on each of the two wake boundaries. The vorticity representation is formed by m trapezoids, a 1/x decaying function, and a constant vorticity as indicated.

Now velocity components induced at each of the 2m control points on the wakes are calculated and stored in the vectors U and V. These include the induction from both the airfoil and wake systems. At each control point the magnitude of the velocity is determined by

$$\overline{U}_i = \sqrt{(1+U_i)^2 + V_i^2} \quad . \tag{69}$$

The dynamic boundary condition on the wake is used to determine the corresponding value of vorticity at each wake control point

$$\gamma_{c_i} = \frac{-\Delta H/\rho}{\overline{U}_i} \quad . \tag{70}$$

All control points on the wake and on the airfoils are located at the midpoints between the endpoints of vorticity distributions. Hence in the wake the value of the vorticity at each endpoint is determined by

averaging the values at adjacent control points or

$$\gamma_{w_i} = \frac{\gamma_{c_i} + \gamma_{c_{i+1}}}{2} \quad . \tag{71}$$

This procedure produces a smooth vorticity distribution in contrast to the results obtained by extrapolation of the vorticity values at the adjacent control point and end point.

Two exceptions to this procedure exist. First at the trailing edge of the airfoils extrapolation is used to determine the vorticity. This satisfies the Kutta condition for this problem. The second exception is at the last element of the vorticity distribution downstream. Here extrapolation is again used to determine the final value of wake vorticity. The difference between this value and γ_∞ is Γ_D for the $1/x$ distribution.

4. Wake Shape Calculation

The new wake coordinates can be calculated by

$$y_w^{(\nu+1)}(x) = y_a + \int_{x_a}^{x} \frac{v^{(\nu)}(x')}{1+u^{(\nu)}(x')}\, dx' \tag{72}$$

where x_a and y_a are the coordinates of the trailing edge of the airfoil. Since line segments are used to represent the wake, the ordinate of the i^{th} segment is

$$y_{w_i}^{(\nu+1)} = y_a + \sum_{j=1}^{i} \frac{V_j^{(\nu)}}{(1+U_j)^{(\nu)}} (x_j - x_{j-1}) \quad . \tag{73}$$

This gives the wake shape for the $(\nu+1)$th iteration.

All of the above steps are completed for both the upper and lower wake systems. At this point the new vorticities and wake shapes

have been determined and hence this step of the process is completed. If desired, the process is repeated to obtain the next iteration.

5. Special Points of the Numerical Solution

In section D we discussed three areas of importance to this problem; the leading edge, the trailing edge, and downstream infinity. The proper conditions for each of these areas have been incorporated into the present solution.

At the leading edge we have the anticipated square root singularity provided by the flat plate vorticity distribution. Of course the value of γ_{a_i} will differ from the isolated flat plate value of $\sin\alpha$ because of the influence of the other airfoil and the wake system. However we have provided the proper singularity to account for the leading edge flow.

Use of the wake dynamic condition to determine the vorticity at the trailing edge of the airfoils has assured compliance with the Kutta condition for this problem. This results from requiring the vorticity on the airfoils to approach the wake vorticity value. This precludes the possibility of a discontinuity in vorticity with a resulting infinite velocity at the trailing edge. Consequently the flow leaves the trailing edge smoothly, as desired.

Asymptotic behavior far downstream has been represented by parallel lines of constant vorticity. We know this approximates the actual behavior well but note that the actual wake continues to deflect downward. However the far downstream wake has little effect on the lifting surfaces since the inductions of the opposing vorticities partially

cancel each other. Further comparison of the downstream wake influence is included in section H.

6. Force and Moment Evaluation

After the convergence of the iterative procedure, the forces and moments on the propulsive lift device are determined. We desire to carry the nonlinear analysis throughout the evaluation and thus we take account of the variation of the local velocity over the airfoils. The velocity at each control point on the lifting surfaces, UB, is calculated. Then the force resulting from the vorticity on each segment of the airfoils is calculated.

First due to the lifting flat plate distribution we have for the i^{th} segment

$$C_{F_{f_i}} = UB_i \gamma_{a_i} \left[\theta_{i+1} - \theta_i + \sin \theta_{i+1} - \sin \theta_i\right] \tag{74}$$

where

$$\theta_i = \arccos (1-2x_i) \quad . \tag{75}$$

Next the force resulting from the triangular distributions is found to be,

$$C_{F_{t_i}} = UB_i \left[\gamma_{a_i} + \gamma_{a_{i+1}}\right] R_i \tag{76}$$

where R_i is the length of the i^{th} segment of the airfoil.

The total normal force coefficient is then

$$C_F = \sum_{i=1}^{n-1} (C_{F_{f_i}} + C_{F_{t_i}}) \quad . \tag{77}$$

Also there is a leading edge force on each airfoil given by equation 36 as

$$C_N = \frac{\pi}{2} \gamma_{a_i}^2 \quad . \tag{78}$$

Now the system lift and thrust coefficients can be determined as

$$C_L = C_N \sin\alpha + C_F \cos\alpha \tag{79}$$

$$C_T = C_N \cos\alpha - C_F \sin\alpha \quad . \tag{80}$$

Note that the actuator force is not included in these calculations since it can easily be added.

In a completely analogous manner the pitching moment is now calculated for the system. From the flat plate loading term we have the moment about the leading edge for the i^{th} segment as.

$$C_{m_{f_i}} = UB_i \gamma_{a_i} \left[\theta_{i+1} - \theta_i - \frac{\sin 2\theta_{i+1}}{2} + \frac{\sin 2\theta_i}{2} \right] \tag{81}$$

θ_i is as given above. Due to each trapezoidal element we have

$$C_{m_{t_i}} = \frac{UB_i \gamma_i}{3} (r_{i+1} - r_i)(2r_{i+1} + r_i) \quad . \tag{82}$$

Here r_i is the distance from the leading edge of the airfoil to the i^{th} endpoint. The leading edge force of course does not contribute to the pitching moment.

$$C_m = \sum_{i=1}^{n-1} (C_{m_{f_i}} + C_{m_{t_i}}) \quad . \tag{83}$$

Again we have not included the effect of the actuator force on the system characteristics.

7. Convergence Test

A criterion is required to determine when the iterative process should be halted. A convergence test is constructed for this procedure by comparing the values of the corresponding vorticities during successive iterations. Thus we form

$$E^{(\nu+1)} = \sum_{i=1}^{k} \frac{\left| \gamma_i^{(\nu+1)} - \gamma_i^{(\nu)} \right|}{\gamma_\infty} , \quad k = 2\,(m+n-1) \quad . \qquad (84)$$

If E^{ν} becomes smaller than a specified number the procedure is considered to have converged and the iterative process is stopped. Of course this neglects any change in the wake shape between successive steps. However since the wake shape is calculated from the induction of the vorticity, it is indirectly accounted for by this test.

A second provision is made for stopping the procedure. This is simply at the completion of some maximum number of iterations if convergence has not occurred. By this method we guard against excessive numbers of steps.

8. Control Points and End Points

The present procedure does not appear to be highly sensitive to the selection of control points and the end points of the segments of the airfoil and wake vorticity distributions. Typical usage was ten equal length segments on each airfoil with a control point in the center of each segment. In the wake the segments were usually larger. An efficient distribution was twenty segments dividing five chords of the wake behind the lifting surfaces. Further downstream than five chords the constant distributions were used. The end points

were more closely spaced near the airfoils than downstream since the vorticity varies significantly in the vicinity of the airfoils. Again the control points are chosen as the segment midpoints.

The solution will have improved accuracy with increasing numbers of airfoil and wake segments. This results from a better vorticity representation and more uniform compliance with the boundary conditions since more control points would be used. However, practical considerations limit the number of segments. Computation time is more of a limiting factor than storage capacity by virtue of the construction of the procedure.

9. Performance of the Procedure

The overall operating characteristics of this method are highly dependent on the parameters of energy addition, airfoil separation, and angle of attack. In general the process converges in about ten to fifteen iterations. Exceptions are cases of small lifting surface separation which require more steps. Here convergence was assumed when $E^{(\nu)} < 0.001\ \gamma_\infty$.

On the IBM System/360, Model 75 computer, the process requires approximately five seconds per iterative step. This is with the use of ten airfoil segments and twenty wake segments for each of the upper and lower systems.

A satisfactory starting solution appears to be the linear solution of section E. The initial solution is also an important factor in determining the number of iterations required before convergence.

Slowest convergence was observed for cases with low values of h/c and high values of C_H. However the angle of attack appears to be the least important parameter to the performance of the procedure. Solutions have been obtained for angles of attack greater than 70 degrees.

H. Presentation of Results

We now consider the solution obtained by the various methods discussed previously. Consideration of these results may provide insight into the propulsive lifting system problem.

1. Numerical Solution

The procedure of section G has provided efficient means for solution of the complete nonlinear problem. It is tedious to present detailed results of these solutions since three parameters (C_H, h/c, α) are required to specify even the simplest geometry. Thus we consider a particular solution in some detail and then examine the effects of varying some of the parameters.

The solution case we consider is that of two equal chord flat plates without stagger and at 10° angle of attack. The airfoil separation is one quarter of a chord and $C_H = 2.0$. The calculated wake shape is shown in figure 12. Notice that the wake contracts slightly and deflects downward before aligning with the free-stream flow several chords aft of the airfoils. The end points of the wake vorticity distributions are also indicated.

Figure 13 shows the upper and lower vorticity distributions for this particular solution. Observe the behavior at the three points of special consideration of section D. At the leading edge the square root singularity accounts for flow about the leading edges. The velocity here is infinite but has integrable lift.

The trailing edge vorticity is continuous but the vorticity increases sharply to the wake value. This rapid rise is characteristic of the jet flap pressure distribution near the trailing edge. Note also

that γ_ℓ is somewhat larger than γ_u at the same station. This results in a net clockwise vorticity which is in the proper sense to account for the curvature of the jet as expressed by the jet flap boundary condition

$$u^+ - u^- = \frac{c C_J}{2} \frac{d^2 y}{dx^2} .$$

Finally, far downstream we see the asymptotic representation in figure 13 is parallel lines of constant vorticity. The 1/x decay of vorticity is also shown. Notice that the value of γ is very nearly equal to γ_∞ at five chord lengths behind the trailing edges of the airfoils. As a consequence Γ_D is quite small.

Also note the unusual loading of the airfoils shown in figure 13. We expect this to produce high pitching moments and distribute the lift unevenly between the two surfaces.

Having considered this case in detail we turn to some more general results. Figure 14 displays the performance of systems of three different airfoil separations. This figure refers to parallel flat plates with no stagger and 10° angle of attack. We see that these lift curves approach a linear relationship with C_H for large energizing of the wake and that the slopes of these curves increase with increasing h/c. For smaller C_H these curves vary significantly from this linear behavior.

The thrust of the system is shown in figure 15. The same system as considered in figure 14 is used. We observe a sharp increase in the thrust of the system as the energy addition becomes larger. In all of these figures the actuator force is neglected since

it can easily be added and does not contribute to the understanding of the problem.

Figures 16 and 17 show a rapid change of lift on each airfoil with increasing C_H. The upper airfoil has greater lift than the lower airfoil at zero energizing but its lift decreases as additional energy is added until its load is actually downward. In contrast the lower wing lift increases rapidly and becomes very heavily loaded. The net lift of the system varies to a much lesser extent than that of either of the airfoils because of cancellation.

The reason for the behavior just described is apparent. The effect of the wake systems and the lower airfoil is to induce a downward velocity at the upper airfoil and hence lessen its effective angle of attack. Of course a decrease in lift results. Conversely, the wake and upper airfoil induce an upward velocity at the lower airfoil tending to increase its effective angle of attack and lift. Any practical design using the propulsive wing at sizeable C_H will certainly need to account for this behavior. Separation is likely to occur without careful design. Also structural and flying qualities of the design will be dependent on this behavior.

Pitching moments resulting from these lift distributions are shown in figures 17 and 18. We observe that the behavior is to be expected considering the distribution shown in figure 13. Additionally we note that since the pitching moments are of different sign for large C_H, the net system moment is much smaller than either of the separate airfoil moments. This eliminates the possible difficulty of large pitching moments for the total system.

2. Wake Deflection

The influence of the far wake on the system and the validity of the approximate representation of the numerical solution merits attention. We know that the actual wake continues to deflect far downstream. This is largely as a result of the influence of the concentrated vorticity at the airfoils which induces a downward velocity. The far field representation of the lifting system is a point vortex so that at the wake

$$v \cong \frac{\Gamma_c}{2\pi x} .$$

Hence the wake deflection is

$$\frac{y_w}{c} \cong \int_o^x \frac{v}{U} d(\frac{x}{c})$$

$$\cong \frac{\Gamma}{2\pi U} \ell n (\frac{x}{c}) .$$

Now Γ is related to the lift by

$$\Gamma = \frac{C_L U}{2} .$$

Thus we have the asymptotic wake deflection as

$$y_w \cong \frac{c\, C_L}{4\pi} \ell n (\frac{x}{c}) .$$

This is plotted on figure 12 and we observe that the wake solution is centered about this line. We also note that in the area where the wake is represented by parallel lines of constant vorticity, the centerline has a small slope. Thus we expect that the parallel lines of constant vorticity will represent the actual wake closely.

To verify this we calculate the velocity induced by vorticity on curved lines as given by y_w above and separated by $\delta_\infty = 0.25c$. This vorticity originates at $x/c = 6.0$ and extends to downstream infinity. The evaluation of the velocity was accomplished numerically and the result is shown in figure 20. Also the comparable velocity induced by a system of straight parallel lines of vorticity is indicated. We find that the parallel representation is remarkably close to the deflected vorticity. Therefore we conclude that the straight parallel wake shape approximates the far downstream wake quite effectively.

3. Comparison of Solutions

Some aspects of the solution provided by the numerical method can be investigated by the use of three associated solutions. First, the solution for $C_H = 0$ obviously corresponds to the unpowered biplane. The solution to this problem was given by Glauert in reference 15. At all angles of attack and airfoil separations the values of B, as defined in equation 30, agree well with the values determined from the numerical solution. This does not provide a test for the wake representation but does imply that the airfoil vorticity representation is adequate.

Other characteristics of Glauert's solution were found in the numerical method. The aerodynamic center was shown to be aft of the quarter chord point as in the exact solution. Also the upper airfoil was seen to carry more lift than the lower airfoil as anticipated.

The second check case is the large C_H limit as discussed in section F. We cannot use for comparison the lift found in section F since it obviously is in serious error at $C_H = 0$. However the slope

of the C_L versus C_H curve for large energy additions is relevant. The slope indicated by equation 49 is shown on the lift curve of figure 14. We observe that this is the slope attained by the nonlinear solution for large C_H. We also note that the h/c dependence of equation 49 seems to be verified. Thus we find good agreement for the case of large C_H.

Finally, we consider the solution for small C_H and α of section E. This is compared with the nonlinear solution in figure 21. We see that the linear solution differs from the nonlinear solution, but this difference is most significant for large C_H. At large energy additions the strength of the wake vorticity of the linearized solution is much too large. The difference in far downstream vorticity between the two solutions is

$$\Delta\gamma_\infty = \gamma_{\infty_{linear}} - \gamma_{\infty_{nonlinear}}$$

$$= U\left[\frac{C_H}{2} - \sqrt{1+C_H} + 1\right] \quad .$$

For small C_H we see that $\Delta\gamma_\infty$ is small but as C_H increases $\Delta\gamma_\infty$ becomes large. This explains the extra lift predicted by the linearized theory at large energy additions.

The difference between the two solutions at small C_H can be attributed to the importance of the wake deflection. Apparently this deflection contributes significantly to the lift even at small energy levels. Better agreement between the linear and nonlinear solutions could be obtained for smaller angles of attack where the wake deflection would be less important. Also there is a slight wake contraction

but the effect is relatively small compared with the wake deflection downward.

4. Variations in Airfoil Geometry

The previous discussion was limited to two parallel flat plate airfoils of equal chords. This basic case can be easily extended to include numerous general geometries.

First the case of unequal length parallel airfoils is the simplest variation. This geometry is handled in the same manner as equal chord systems with vorticity placed only on the chord lines of the flat plate airfoils of different lengths. Identical vorticity functions are used as before and conditions at the trailing edges are the same.

Figure 22 shows a typical result for an unequal chord airfoil system. All lift coefficients are based on the lower airfoil chord. As we anticipate the unequal chord lift is less than the equal chord lift at $C_H = 0$. However, the unequal chord system benefits from more rapidly increasing C_L as C_H increases and eventually achieves a greater lift than the equal chord system. This performance results from the absence of a large upper airfoil to carry sizeable negative lift at high energy additions. The lower airfoil of the unequal chord system benefits from the wake system in a manner similar to the equal chord system. Consequently, the net result is an improved performance from the unequal chord system. Of course for $c_u/c_l > 1$ we expect the opposite behavior with poorer performance than the equal chord system.

The case of nonparallel airfoils is again a simple extension of the present procedure. Since the method is nonlinear, the only modification necessary is placement of the airfoil vorticity in its correct position.

We see that we can immediately extend the present procedure to include flat plate airfoils of quite general positions. Two further extensions of interest are airfoils with thickness and camber. These effects are considerably more complicated to incorporate in the present method than the flat plate systems. However, conceptually the only modification necessary is provision for the correct types of singularities. Although feasible, this does not appear to greatly extend the understanding of the present problem and hence is not considered here.

III. EXPERIMENTAL INVESTIGATION

In order to investigate the validity of some of the assumptions and idealizations of the previous part, a wind tunnel study was conducted. This study provided a useful check on various aspects of the model we have considered thus far.

The wake representation is one important factor to be examined. We know that the vortex sheets at the wake boundary of the theoretical model will not be present in the real flow case. Influences of viscosity such as entrainment and mixing have been ignored in the analytic study. Thus effects of viscosity on the wake system must be observed to determine the limitations of the analytical wake model.

Additionally, the adequacy of the lifting surface representation merits investigation. Again, real effects may be significant. The theoretical calculation predicts high airfoil loadings with unusual pressure distributions. As a result the flow may separate from the airfoil surfaces. Also the lifting surfaces, because of physical considerations, must be thick airfoils instead of flat plate airfoils. Therefore we obtain a check on the importance of thickness of the airfoils.

A. Wind Tunnel Model

An apparatus to closely simulate the analytical models discussed previously is difficult to construct. The method of uniform, two-dimensional energy addition chosen was injecting numerous small streams of high energy air between two lifting surfaces. Obviously this produces the undesirable side effect of mass addition to the internal airstream. However, precaution was taken to keep the mass addition small in relation to the mass of the air passing between the lifting

surfaces.

The ejectors obtained for this experiment, loaned from NASA Ames Research Center, are shown in Figure 23. Nine-hundred and twenty individually supplied tubes are attached to the common manifold. Each tube is fitted with a nozzle. The nozzles have throats of about 0.018 inch in diameter. This fine grid of ejectors provides a uniform energy addition after a mixing region of several nozzle diameters downstream.

Flow blockage by the ejectors was found to have a small influence for the zero C_H case since removal of the ejectors resulted in only minor surface pressure changes. The ejectors blocked 17% of the total internal flow area. The total nozzle area of about 0.002 square foot provided for large energy additions by high velocity air, while the total ejector mass addition remained small. Typically the ejector mass addition was about one percent of the mass flow between the airfoils.

Ideally the wind tunnel model lifting surfaces would have been flat, or at least thin airfoils. This would have allowed direct comparison of the experimental and analytical results. However, the rather bulky manifold tube of the ejector assembly prevented the use of a thin airfoil section. In fact, a twenty percent thick airfoil was required to house the manifold tube. A laminar flow airfoil, NACA 653020 was selected since its maximum thickness point occurs near the midchord and consequently the manifold could be located at this position. The energy addition was made at the midchord in order that the initial mixing of the high energy air with the flow between the air-

foils would not disturb the uniform head flow conditions at the leading or trailing edges.

The model cross section is shown in Figure 25 and the model assembly in Figures 23 and 24. The airfoil chords are 0.98 foot and the airfoil is 0.44 foot. The model span is 2.31 feet with the resulting aspect ratio of 2.4. This aspect ratio was limited by the ejector assembly dimensions and the wind tunnel size. In an effort to increase the effective aspect ratio and obtain as nearly two-dimensional flow as possible, end plates were placed on both sides of the model. The end plates started approximately one chord upstream and extended four chords downstream aft of the model.

An additional feature of the model is apparent from Figure 24. This is the location of nine vanes between the upper and lower airfoils. These vanes were employed to minimize the spanwise flow which was observed before their placement.

The wind tunnel used for this study was the Merrill Wind Tunnel at the Graduate Aeronautical Laboratory of the California Institute of Technology. The test section measures 46 by 32 inches and 9 feet in length. The tunnel is a closed return, constant operating tunnel capable of speeds of over 100 feet per second. However, in order to obtain C_H values of interest, a speed of twenty feet per second was used in the tests.

The effect of the wind tunnel top and bottom walls might be expected to be significant. However, the influence of these walls can be estimated by placing wake system images above and below the actual

wake system. These images induce insignificant velocity at the airfoil locations for two reasons. First, the vorticity representing the various wake image boundaries are of opposite direction and also of nearly equal strength. Therefore, the induced velocity of the pair nearly cancels. Secondly, the image systems are at a distance of about three chords from the airfoils at their nearest point. This distance results in small induced velocity at the airfoils when compared to the velocity induced by the wake system immediately behind the airfoils. Due to these factors, the wall influences are expected to be small.

B. Experimental Measurements

The most important parameter of this experiment is the energy addition intensity. The coefficient C_H is the most convenient parameter to use in comparison of the experimental results with the calculated values and consequently we consider the measurement of this factor.

A direct approach to this measurement is through the equivalent actuator thrust. We determine the momentum supplied by the ejectors and then we can find the corresponding value of ΔH. We assume that the flow in the manifold and through the ejectors is isentropic and that the air behaves as a perfect gas and consequently we can determine the exit velocity at the nozzles by the relation

$$V_e = a_s \frac{2}{\gamma - 1}\left[\left(1 - \frac{p_e}{p_s}\right)^{\frac{\gamma-1}{\gamma}}\right]^{\frac{1}{2}} ,$$

where p_s and a_s are the supply pressure and speed of sound, p_e the exit pressure and γ is the ratio of the specific heats of air. The exit pressure of the nozzles is assumed to be atmospheric pressure. Of course the airfoil system causes the exit pressure to be somewhat different from atmospheric pressure. However this variation was measured from the airfoil surfaces and found to be less than 0.001 atmosphere of pressure and therefore is neglected.

Now the momentum that passes through the ejectors is

$$MV_{flux} = \dot{M}_e V_e ,$$

where $\dot{M}_e$ is the mass flux through the ejectors. This mass flux was determined by measuring the volume flow through the supply line,

$\dot{V}_s$, at supply pressure. Then by simple mass conservation

$$\dot{M}_e = \rho_s \dot{V}_s ,$$

where ρ_s is the supply air density. In terms of standard cubic feet per unit time, $\bar{\dot{V}}_s$, measured by a Fischer-Porter flow meter, this becomes

$$\dot{M}_e = \rho_o \dot{V}_s \left(\frac{p_s}{p_o}\right) ,$$

where p_o is one atmosphere of pressure and ρ_o is the density of air at standard temperature and pressure.

Finally then

$$MV_{flux} = \rho_o \bar{\dot{V}}_s a_s \left(\frac{p_s}{p_o}\right)\left[\frac{2}{\gamma-1}\left(1 - \left(\frac{p_e}{p_s}\right)^{\frac{\gamma-1}{\gamma}}\right)\right]^{\frac{1}{2}} .$$

Here the supply speed of sound is given by

$$a_s = 1117\sqrt{\frac{T_s}{288}} ,$$

where T_s is the supply air temperature. The values of p_s were obtained from the low velocity supply line.

We now have the necessary relations to determine the simulated value of C_H as

$$C_H = \frac{2 \bar{\dot{V}}_s a_s}{U^2 b h_a}\left(\frac{p_s}{p_o}\right)\left[\frac{2}{\gamma-1}\left(1 - \left(\frac{p_o}{p_s}\right)^{\frac{\gamma-1}{\gamma}}\right)\right]^{\frac{1}{2}} .$$

Here b is the model span, h_a is the ejector height and U is the free-

stream velocity. This relation shows the necessity of using relatively slow test speeds in order to obtain C_H values of interest.

The measurement of C_H for this study was determined from the volume flow and ejector pressure ratio using the above relation. This was used for procedural considerations rather than direct measurement in the jet. Checks of the wake energy levels showed them to correspond closely with the values measured from the high pressure air supply conditions.

In order to determine the pressure distributions on the airfoils, 80 static pressure taps were incorporated into the model surfaces. This was accomplished by embedding copper tubing in spanwise slots cut into the surfaces of the model. One sixty-fourth inch diameter holes were drilled in the tubing at desired spanwise positions. The static pressures were measured individually by a single micromanometer.

The dependency of the flow on Reynolds number wake checked by tests at various wind tunnel speeds. In the case of zero energy addition by the ejectors, the pressure distribution on the airfoil surfaces was found to be nearly identical over a range of Reynolds number of 1.3×10^5 to 6.5×10^5. Indication of flow separation from the airfoils would have been evident over this range and was not found. For nonzero C_H the Reynolds number variation check was also conducted and again no sign of significant viscous behavior was observed.

Examination of the wake was conducted by two methods. First extensive total head surveys were made at seven positions downstream

of the model trailing edges. Also, a hot wire anemometer was employed to survey various stations downstream. Particular use was made of the hot wire anemometer in areas near the trailing edges where the static pressure could vary significantly from the value far from the jet.

C. Presentation of Results

The following results were obtained at a test speed of 20 feet per second. The Reynolds number based on the model chord was 1.3×10^5. Runs were conducted at zero and ten degrees angles of attack of the airfoils. The chord lines of the airfoils were always kept parallel. Runs at zero degrees were primarily devoted to checks on the flow symmetry and the effects of the substantial thickness of the airfoils on the air flow between them. All other runs were conducted at ten degrees. Although higher angles of attack would be of interest, the tunnel size prohibited such tests. Impingement of the high energy jet and wind tunnel blockage would certainly become dominant at higher angles of attack.

First checks of the two-dimensionality of the flow resulted in the placement of nine flow straightening vanes in the aft portion of the model as pictured in figure 24. Previous to this modification, some spanwise flow was observed by the use of tufts. This flow was apparently the result of some secondary flow or an imperfection in the model construction. The vanes corrected this situation to a high degree.

The next check performed concerned the two-dimensionality of the exit flow. At ten degrees angle of attack the wake was surveyed at a distance of 1.5 inches behind the upper trailing edge. Comparison of this survey at three spanwise positions is shown in figure 26. These results made it apparent that the exit flow was two-dimensional (or at least uniform in a spanwise direction) even within the neighborhood of the end plates.

The decrease and increase of velocity at the top of the curve was evidently caused by the flow retardation of the boundary layer on the airfoil. This decrease and increase was a characteristic of the velocity curves for all values of C_H. The curve of figure 26 does not display the same decrease at the bottom of the jet since here the probe was somewhat further aft of the bottom trailing edge due to the angle of attack. Hot wire anemometer measurements perpendicular to the chordlines of the airfoils, displayed this decrease in the vicinity of both trailing edges. This characteristic of the velocity curves was not found in measurements further downstream. In these areas the flow had mixed so that no velocity was less than the free-stream value.

As a final check on the two-dimensionality of the model, static pressures were measured at various spanwise positions. Again the model exhibited two-dimensional behavior. Unquestionably the flow at the end plates was not two-dimensional. However, the above checks indicated that a large part of the model approximated the desired flow.

Wake surveys were conducted at seven downstream positions by use of a total head probe for each of six values of C_H at $\alpha = 10°$. A typical display of the resulting wake velocities is given in figure 27. The straight vertical lines represent a free-stream velocity of 20 feet per second at the downstream location examined. The solid curves indicate velocity above the free-stream value according to the scale shown. The broken line of this figure is the wake boundary calculated by the numerical procedure of Section IIA for this C_H and α.

Also indicated on this figure is the center of momentum for the jet. This was calculated from the wake surveys as the position y_c where

$$\int_{-\infty}^{y_c} \rho u^2 \, dy = \int_{y_c}^{\infty} \rho u^2 \, dy \quad .$$

Thus there is equal jet momentum flux above and below this line. This line indicates the mean downward movement of jet momentum as the wake proceeds downstream.

Figure 28 shows the experimental wake boundary shape. The wake boundary shown by the solid line was determined from points where the measured wake velocity was five percent higher than the free-stream velocity. This method of determining the wake boundary lessened error due to the sensitivity of the measuring equipment. As before the numerically predicted shape is indicated by the broken line.

The second set of experimental measurements was the surface pressure measurement. These pressures were measured from taps in the tube embedded in the model surfaces. The static pressures were quite small even though their corresponding coefficients of pressures were sizable due to the low free-stream velocity. The low pressures involved required special precautions for accurate measurement. Also particular attention was given to minimize effects of long scale unsteadyness due to changing wind tunnel and air supply conditions. All of the following pressures were measured at the midspan of the model.

As an introduction to the characteristics to be anticipated from the pressure distributions of this airfoil geometry, Figures 29 and 30 give the zero energy addition case. The pressure distribution shown for a single airfoil was obtained from Reference 18. The analytic biplane solution shown in these figures was determined numerically by the Douglas Neumann method for a two-dimensional biplane in unbounded flow as described in Reference 19. By comparison with the single airfoil pressure distribution, we note that the pressure distributions for the biplane are significantly altered by the neighboring airfoil. For cases of nonzero C_H we expect many of the same characteristics that these figures display to be amplified.

The experimentally determined pressure distributions of Figures 29 and 30 agree well with the analytical solution with the exception of the upper surface of the lower airfoil near the leading edge. Here the suction peak expected from the analytic solution is not observed experimentally. This discrepancy was seen not to be due to the effects of viscosity. The adequacy of the analytic representation in this area of the lower airfoil is likely the reason for the disagreement. The position of the stagnation point is critical here and may account for the apparent inaccuracy of the analytic solution.

Figure 31 shows a typical lower airfoil pressure distribution for moderate C_H. We observe that the lower surface pressure distribution is much like that of a single airfoil at angle of attack as shown in Figure 29. This was observed to be true for the range of C_H values tested. Further, the lower surface pressure distribution was found to have a weak dependence on intensity of energy addition. However, the

upper surface of the lower airfoil was observed to be strongly affected by changes in C_H. The basic shape of the pressure curve is similar for all moderate C_H values.

The increase and decrease in C_P of the upper surface at approximately x = 0.1 c in Figure 31 was found for all values of C_H. At first it might appear that this dip in the pressure resulted from separation of the flow from the lower airfoil as it becomes more heavily loaded with increasing C_H. However, after study of this area with China clay and tufts, it became evident that separation of the flow was not occurring. Comparison with tests at $\alpha = 0$ showed that the sudden decrease in C_P was due to the acceleration of the flow between the airfoils. The rather thick airfoils are seen to produce a Venturi effect at all values of C_H. The acceleration modifies the pressure distribution in a manner observed in Figure 31.

Pressure distributions of the upper airfoil are presented in Figure 32. Again, we notice that the external surface, the upper surface in this case, has a pressure distribution similar to an isolated airfoil. The pressure distribution of this surface has little dependence on the other airfoil or the parameter C_H. However, again the internal, or lower surface, is strongly influenced by the other airfoil and the energy addition. The pressure on the lower surface is observed to reach its lowest value at the point of energizing.

The same rapid change in pressure at approximately x = 0.1 c is again observed as for the upper surface of the lower airfoil. In the case of the lower surface of the upper airfoil, however, the decrease in C_P due to the accelerating flow is not as prominent. This is because

the pressure is decreasing from its high value as the flow stagnates near the leading edge.

We also observe that much of the upper airfoil carries a downward load for the case shown in Figure 32. At about x = 0.2 c the lower surface pressure becomes less than the upper surface pressure. Hence, from that point aft to the trailing edge, the load is downward. Forward of this point the load is in the upward direction.

The loadings of the airfoils are more clearly shown in Figures 33 and 34. We see that the load on the lower airfoil steadily increases with increasing energy addition. In contrast, we note that the upper airfoil, although having positive lift at $C_H = 0$, becomes heavily loaded in the negative direction as C_H increases. Also, we see that the point where the loading crosses the axis between positive and negative lift moves forward as C_H increases for the upper airfoil. The rapid decrease and following increase in the loading of the lower airfoil is apparent and results from the acceleration of the flow between the airfoils as discussed above.

The total airfoil lift is shown in Figure 35. This lift was determined by integration of the surface pressures measured on the airfoils. As in the numerical calculations, the lift resulting from the force on the actuator is not included. The calculated lift for flat plate airfoils with the airfoil separation and angle of attack of the model is also indicated in Figure 35.

Of course, due to the significant differences in the experimental and theoretical airfoil geometries, we expect different lifts at $C_H = 0$. However, the quantity of importance is the lift augmentation as energy

is added to the flow. Figure 36 displays the rate of lift increase with increasing C_H. Here the numerical result of the lift slope shows rapid decrease to the limit value for large energy addition.

The experimental lift slope determined from the slope of lines connecting neighboring points of Figure 35 has extreme scatter. Consequently a least squares fit of the points shown in Figure 35 was accomplished and the slope of this curve is shown in Figure 36 as the experimental value.

Of nearly equal importance as the system lift is the pitching moment resulting from the pressure distributions discussed earlier. Figures 37 and 38 show the measured and predicted pitching moments for the two lifting surfaces. These are nose down moments about the leading edge of each surface. We observe that each of the airfoils develops quite large pitching moments as C_H increases. However, since the moments are of opposite directions, we expect that the net moment is much smaller. This is verified in Figure 39 where the total pitching moment for the two surfaces is shown.

D. Comparison of Experimental and Calculated Results

The previous section provides considerable experimental data for use in comparison with the calculations of part II. We consider these points now.

First, the wake shape experimentally determined compares well with the shape of the numerical solution. Of course the effects of viscosity are quite evident in the experimental tests in the form of considerable mixing of the wake. However this primarily occurred relatively far downstream and we anticipate this to have rather insignificant influence on the airfoils.

The surface pressure distributions are significantly altered by the thickness of the airfoils and consequently do not lend themselves to direct comparison. Nevertheless we notice the similarity in the observed and predicted behavior. The lower airfoil was seen to be more heavily loaded as energy addition increased. Further, the upper airfoil exhibited rapidly decreasing lift with increasing C_H until this airfoil became loaded negatively. Moreover the forward part of the upper airfoil was observed to carry positive lift while the aft portion was loaded negatively. All of these characteristics are exactly as anticipated from the numerical solution.

Additionally, the model lift curve, although of lower lift than predicted for flat plate airfoils, does exhibit the correct shape. The lift at zero energy addition is the difficulty here. The considerable thickness of the airfoils lessened the lift of the biplane system. Also viscous effects may account for some of the discrepancy in the lift

at zero energy addition.

Due to the discrepancy of the lift at $C_H = 0$, the lift slope is more significant than the actual lift. We observe good agreement between the predicted and experimentally determined augmented lift slope.

The pitching moments found experimentally make it apparent that the pressure distributions are similar in nature for the experimental model as predicted by the numerical procedure. We expect differences in these moments due to the considerable thickness of the experimental model. We observe that the cancellation of the moments for the upper and lower airfoils fortuitously removes the problem of large pitching moments for either of the lifting surfaces separately.

REFERENCES

1. McCormick, Barnes W., Aerodynamics of V/STOL Flight, Academic Press Inc., New York, 1967, Chapter 9.
2. Kuchemann, Dietrich and Weber, Johanna, Aerodynamics of Propulsion, McGraw-Hill Inc., New York, 1953, Chapter 6.
3. Winborn, Byron R., "The ADAM III V/STOL Concept," Journal of Aircraft, Vol. 7, No. 6, March-April 1970, pp. 175.
4. Davidson, J. K., "Aerodynamics of the Propulsive Wing," Air Force V/STOL Tech. and Planning Conf., Sept. 23-25, 1969.
5. Havey, C. Todd, "ADAM II Propulsion System and Internal Aerodynamics," SAE #670353, April 1967.
6. Winborn, Byron R., "The Propulsive Wing Turbofan V/STOL," SAE #650203, April 1965.
7. Beissnor, F. L., "Results of Initial High Speed Wind Tunnel Test on ADAM II," LTV Report 2-53310/4R-5003, February 1964.
8. Jameson, Antony, "The Analysis of Propeller-Wing Flow Interaction," NASA Symposium on Analytical Methods in Aircraft Aerodynamics, October 1969.
9. Levinsky, E. S. et al., "Lifting-Surface Theory for V/STOL Aircraft in Transition and Cruise I," Journal of Aircraft, Vol. 6, No. 6, November-December 1969, pp. 488-495.
10. Spence, D. A., "The Lift Coefficient of a Thin, Jet-flapped Wing," Proc. Royal Soc., A. Vol. 238, pp. 46-68, 1965.

References (Cont'd)

11. Spence, D. A., "Some Simple Results for Two-Dimensional Jet-Flap Aerofoils," Aeronautical Quarterly, Nov. 1958, pp. 395-406.

12. Thwaites, Bryan, Incompressible Aerodynamics, Oxford University Press, London, 1960, pp. 177.

13. Orszag, S. A., and Crow, S. C., "Instability of a Vortex Sheet Leaving a Semi-Infinite Plate," Studies in Applied Mathematics, Vol. XLIX, No. 2, June 1970.

14. Stratford, B. S., "Early Thoughts on the Jet Flap," Aeronautical Quarterly, Vol. 7, Feb. 1956, pp. 45.

15. Glauert, H., The Elements of Aerofoil and Airscrew Theory, Second Edition, Cambridge University Press, Cambridge, 1948, pp. 173.

16. Braunss, Günter, Licke, Wolfgang, "The Lift Distribution on a Flat Plate Near the Ground," Zeitschrift für Flugwissenschaften, 10 (1962), Heft 7.

17. Lamb, Horace, Hydrodynamics, Sixth Edition, Cambridge University Press, Cambridge, 1932, pp. 74.

18. Abbott, Ira H., von Doenhoff, Albert E., and Stivers, Louis S., "Summary of Airfoil Data," NACA Rept. No. 824, 1945.

19. Hess, J. L. and Smith, A. M. O., "Calculation of Potential Flow About Arbitrary Bodies," in Progress in Aeronautical Sciences, Vol. 8, Pergamon Press, New York, 1966.

LIST OF FIGURES

Fig. No.	Title	Page
1	Propulsive Wing Concept	77
2	Basic Geometry	78
3	Boundary Conditions	79
4	Linearized Boundary Conditions	80
5	Parts of Linear Solution	81
6	Biplane Lift	82
7	Large Energy Addition	83
8	Vorticity Distributions	84
9	Numerical Representation	85
10	Airfoil Representation	86
11	Wake Representation	87
12	Wake Shape	88
13	Vorticity Distribution	89
14	Lift Curve	90
15	System Thrust	91
16	Lower Airfoil Lift	92
17	Upper Airfoil Lift	93
18	Lower Airfoil Pitching Moment	94
19	Upper Airfoil Pitching Moment	95
20	Induced Wake Velocity	96
21	Comparison of Solutions	97
22	Unequal Chord System Lift	98
23	Experimental Apparatus	99
24	Wind Tunnel Model	100

List of Figures (Cont'd)

Fig. No.	Title	Page
25	Model Cross Section	101
26	Spanwise Uniformity	102
27	Wake Velocities	103
28	Wake Shape	104
29	Lower Airfoil Pressure Distribution	105
30	Upper Airfoil Pressure Distribution	106
31	Lower Airfoil Pressure Distribution	107
32	Upper Airfoil Pressure Distribution	108
33	Lower Airfoil Load Distribution	109
34	Upper Airfoil Load Distribution	110
35	Total Lift	111
36	Lift Slope	112
37	Lower Airfoil Pitching Moment	113
38	Upper Airfoil Pitching Moment	114
39	Total Pitching Moment	115

TABLE 1

Normalized Leading Edge Singularity Strength

h/c	$\bar{N}_o$
0.125	0.077
0.250	0.116
0.500	0.169
0.750	0.207
1.000	0.238
1.250	0.264
1.500	0.286
1.750	0.307
2.000	0.325

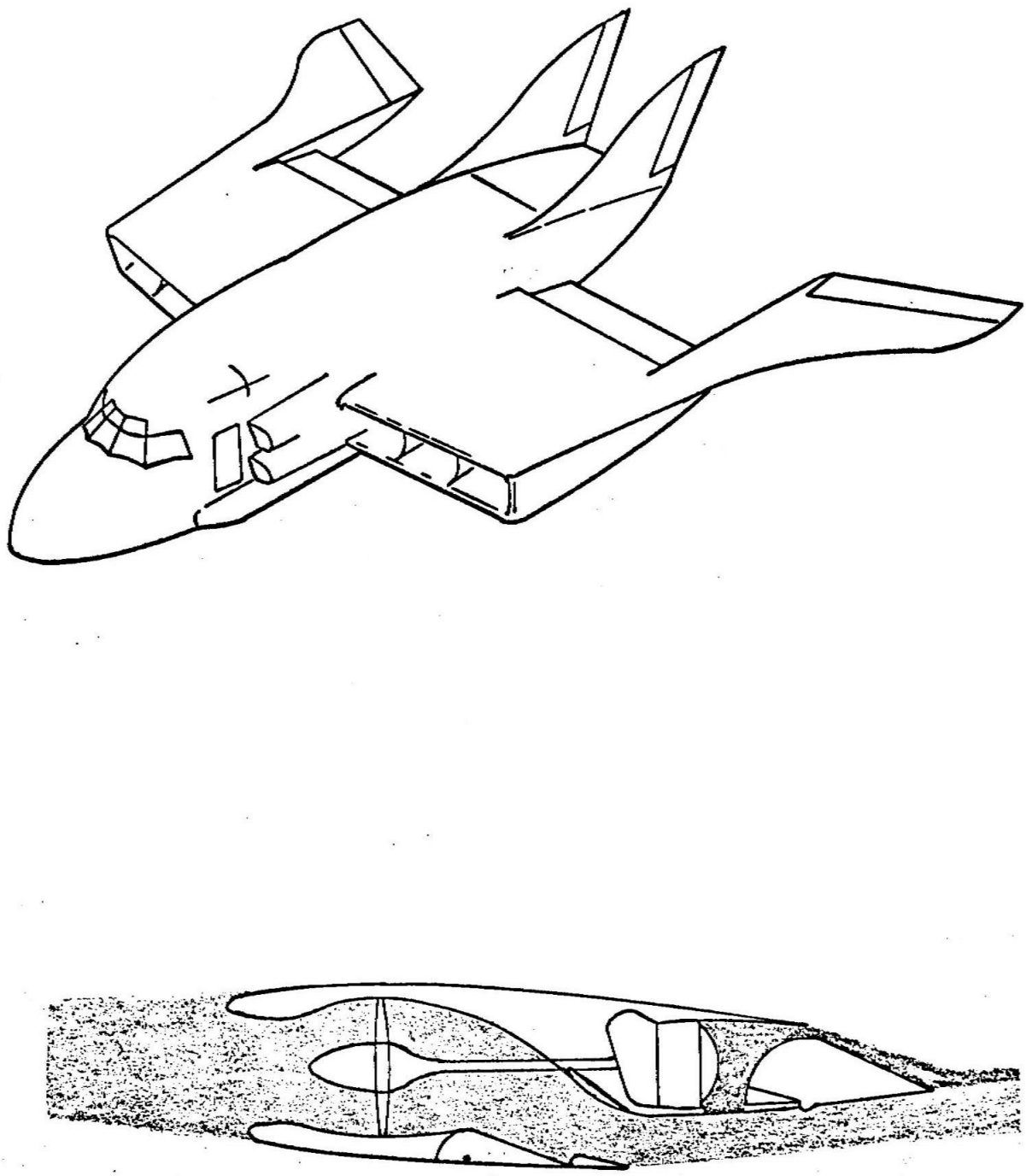

PROPULSIVE WING CONCEPT
figure 1

BASIC GEOMETRY

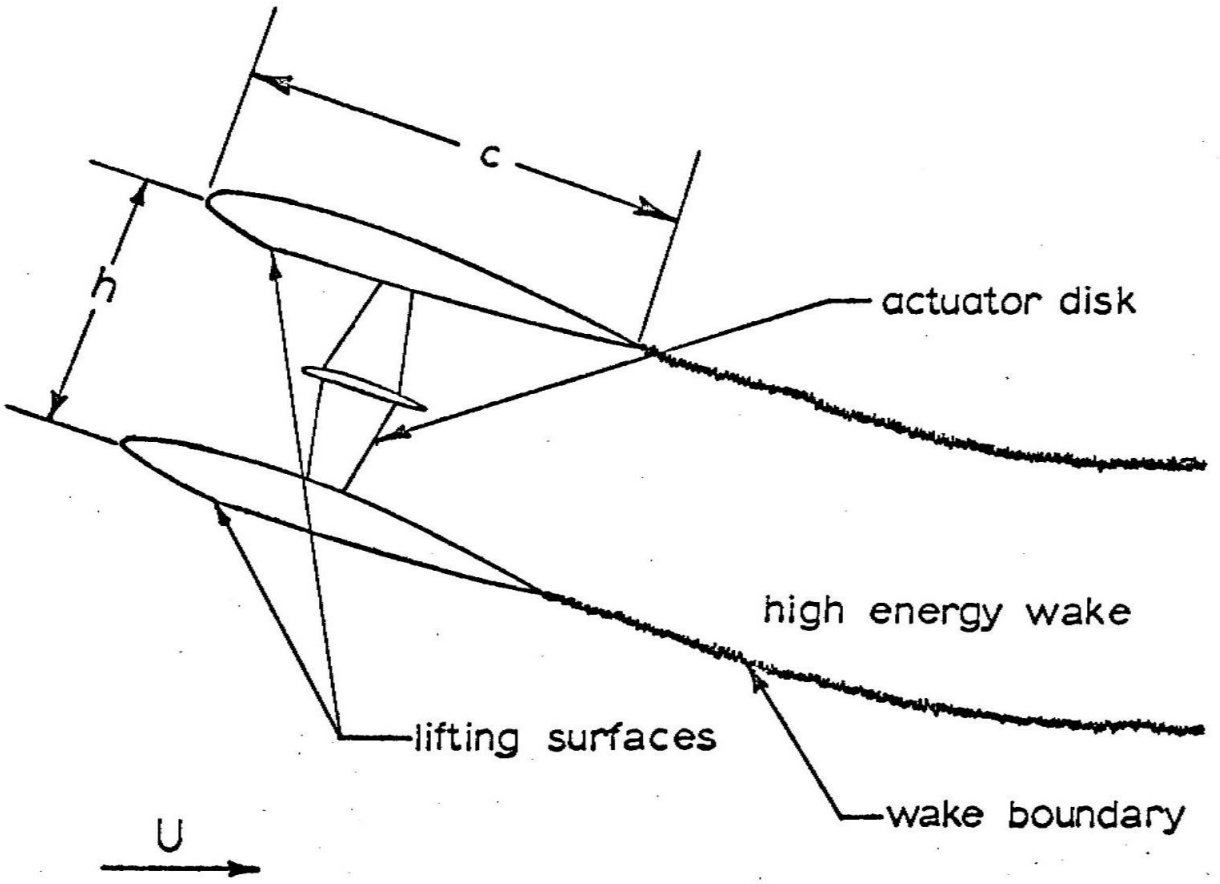

figure 2

BOUNDARY CONDITIONS

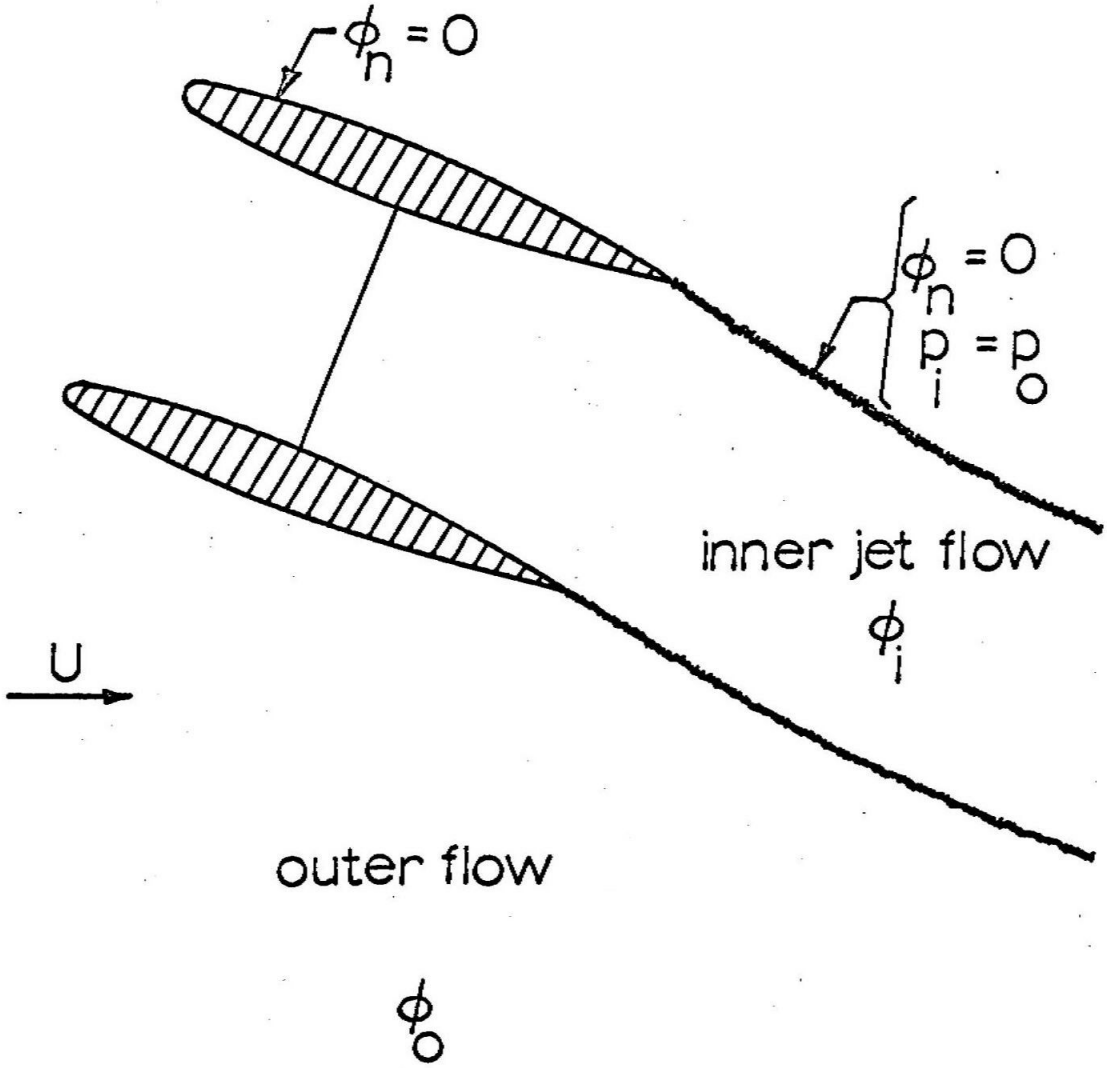

figure 3

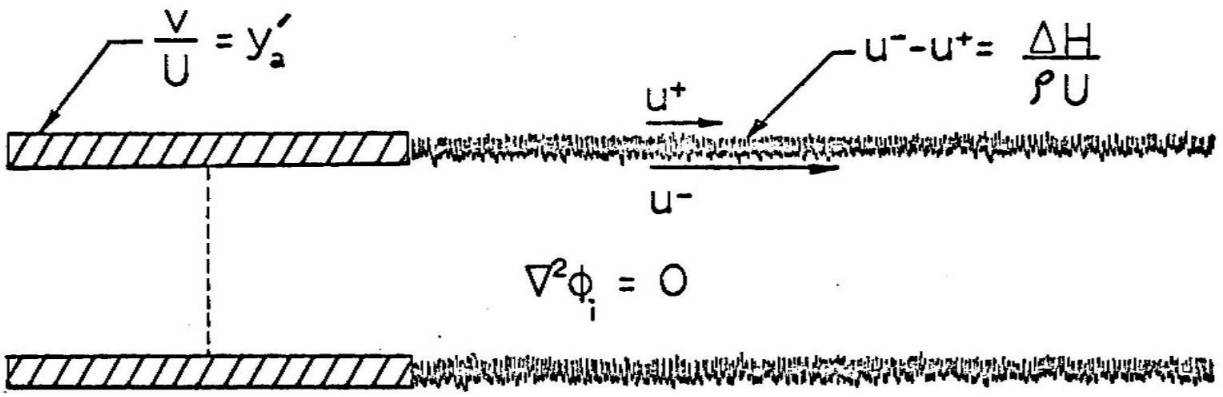

$$\nabla^2 \phi_o = 0$$

LINEARIZED BOUNDARY CONDITIONS

figure 4

PARTS OF LINEAR SOLUTION

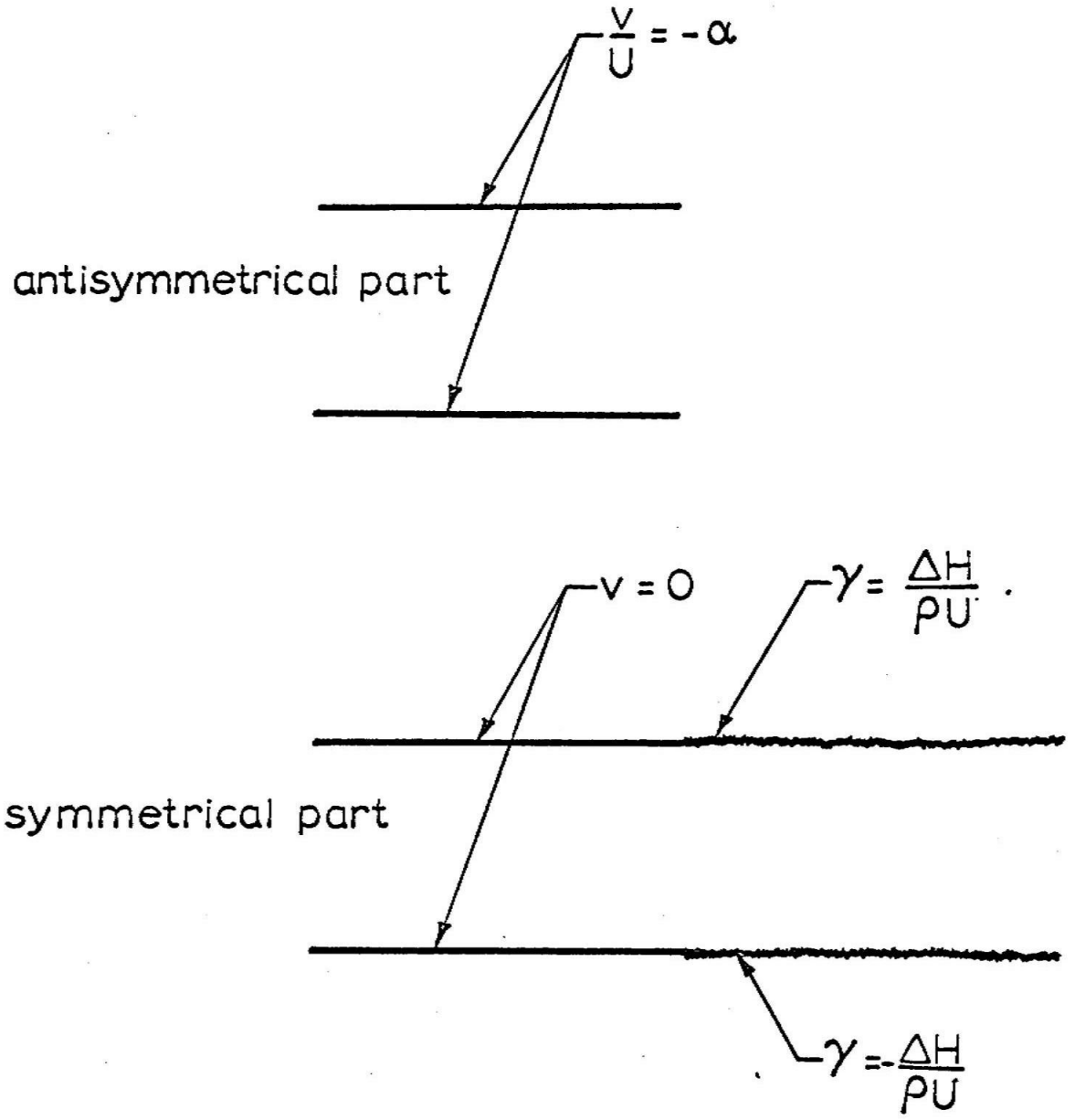

figure 5

BIPLANE LIFT

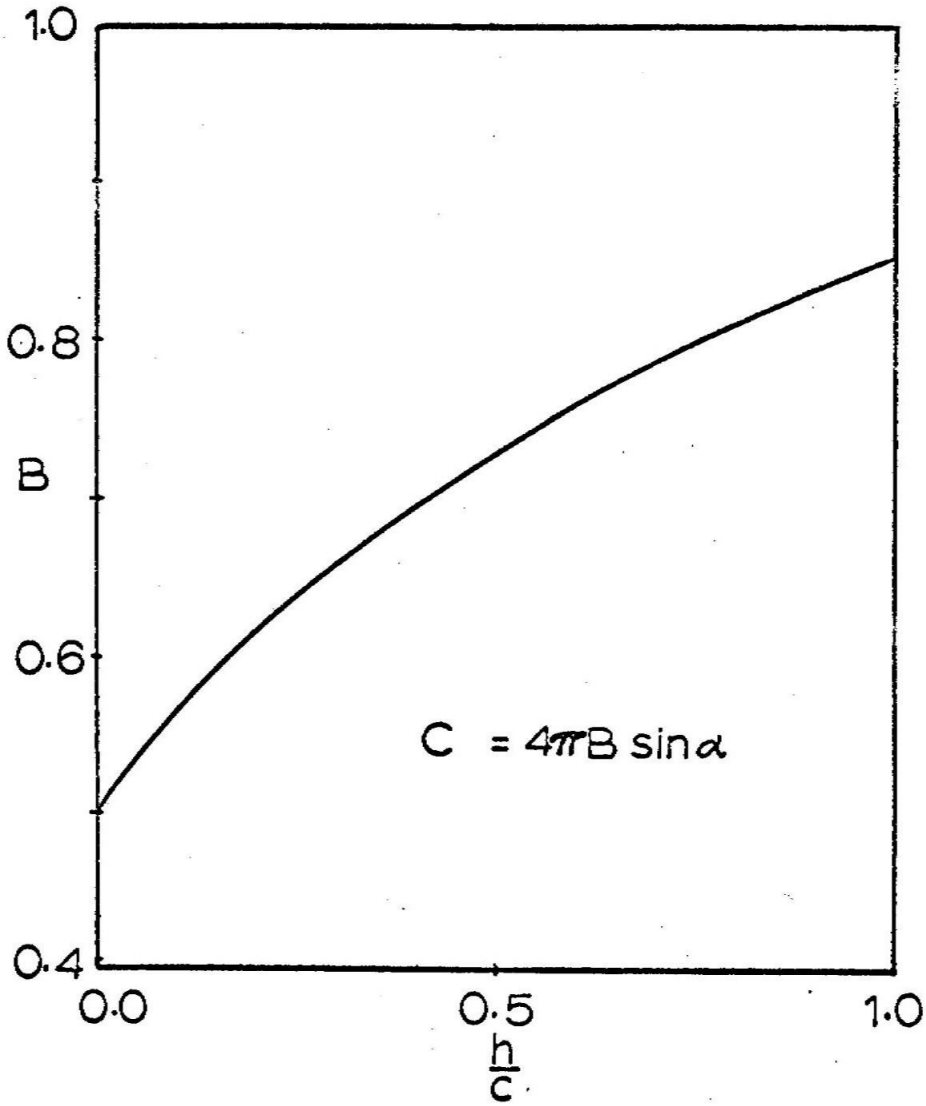

figure 6

LARGE ENERGY ADDITION

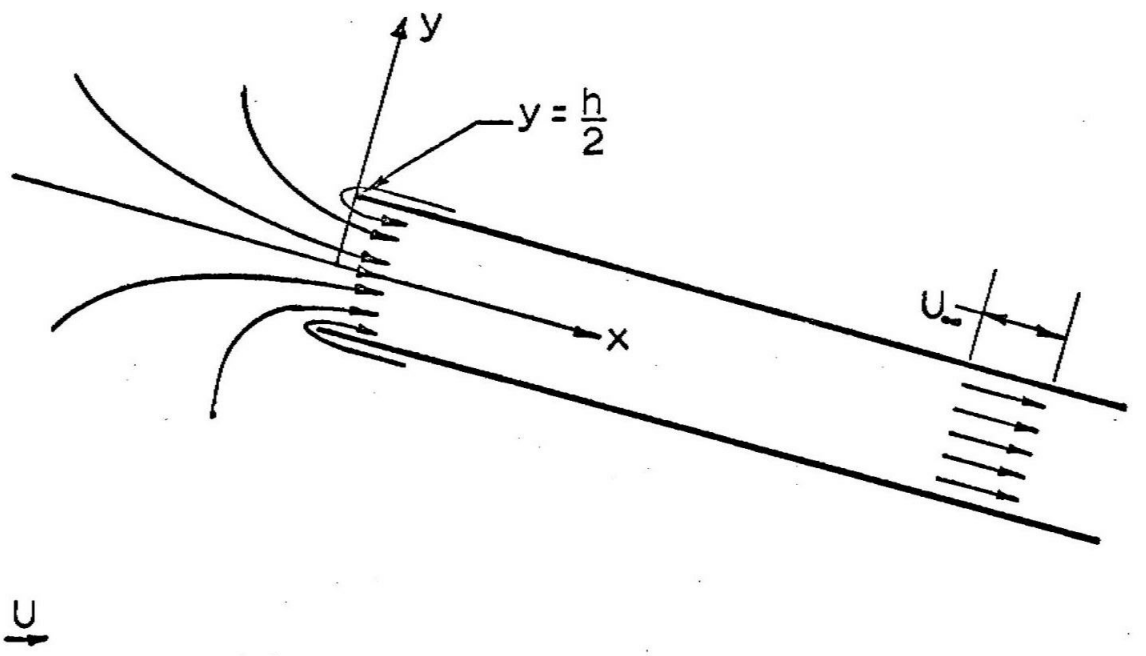

figure 7

VORTICITY DISTRIBUTIONS

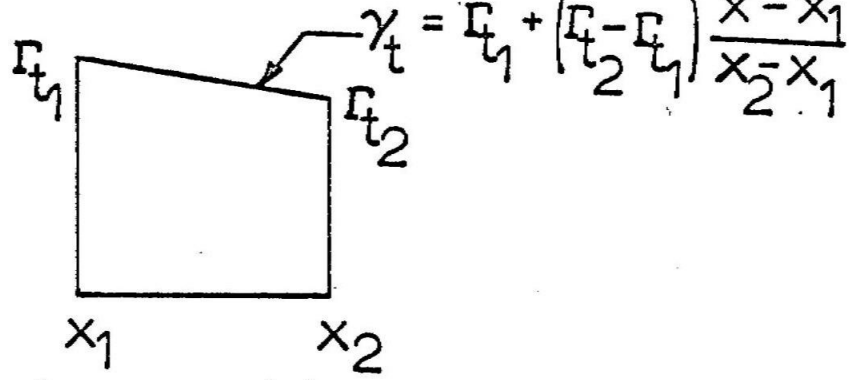

(1) trapezoid

(2) lifting flat plate distribution

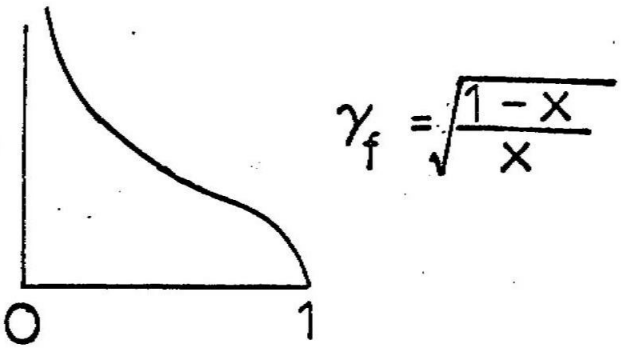

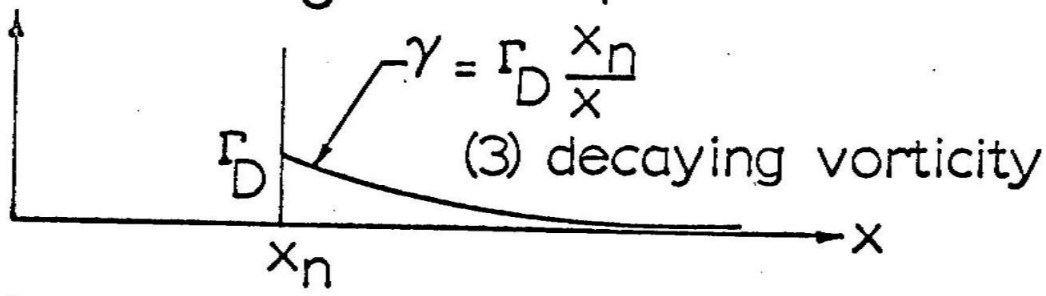

(3) decaying vorticity

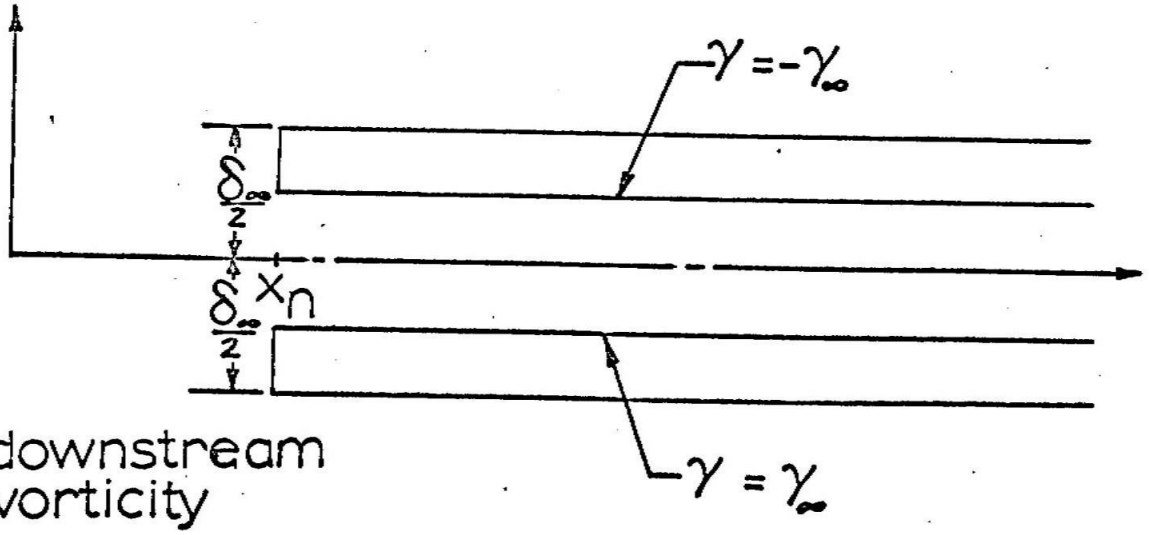

(4) downstream vorticity

figure 8

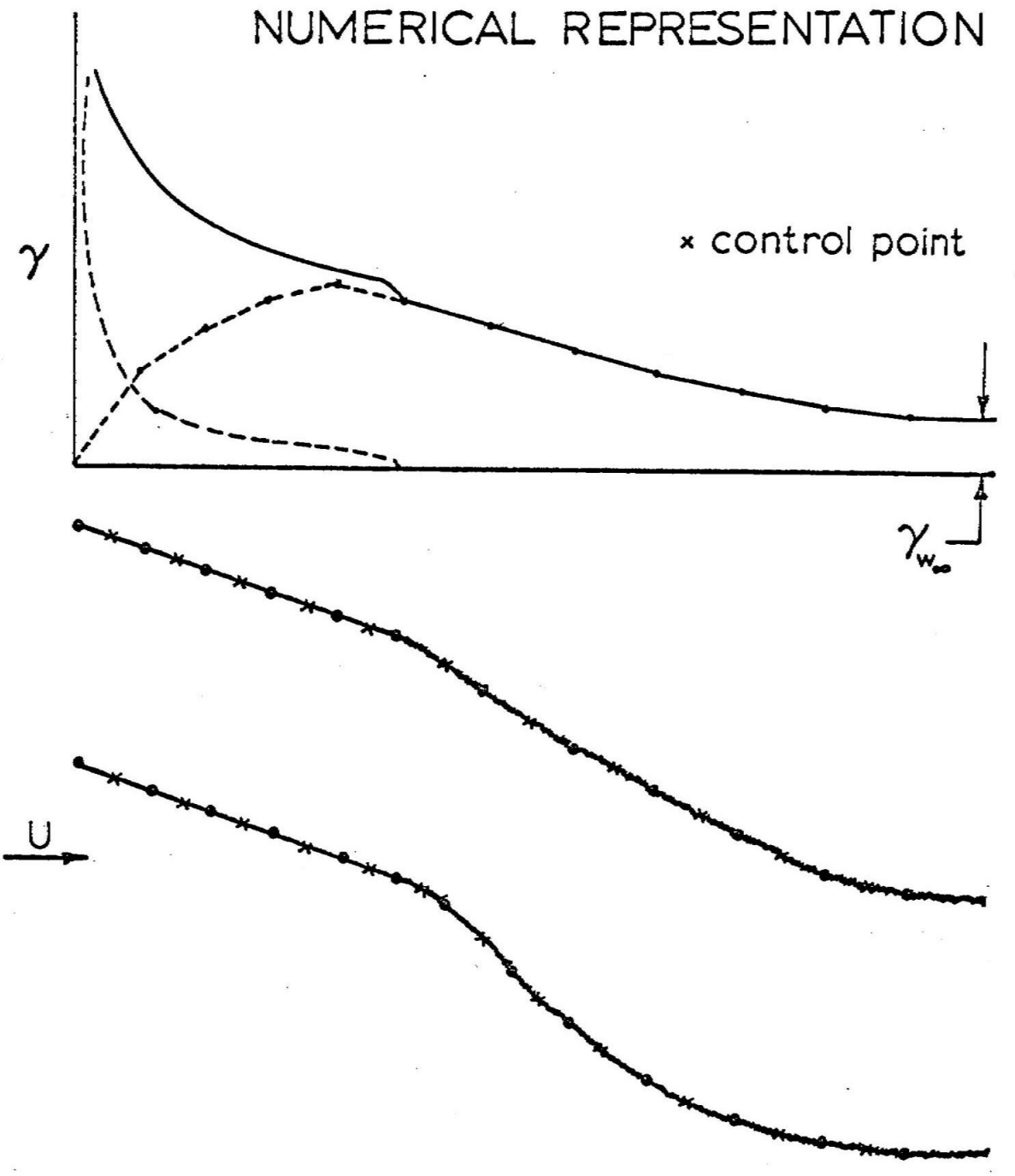

figure 9

AIRFOIL REPRESENTATION

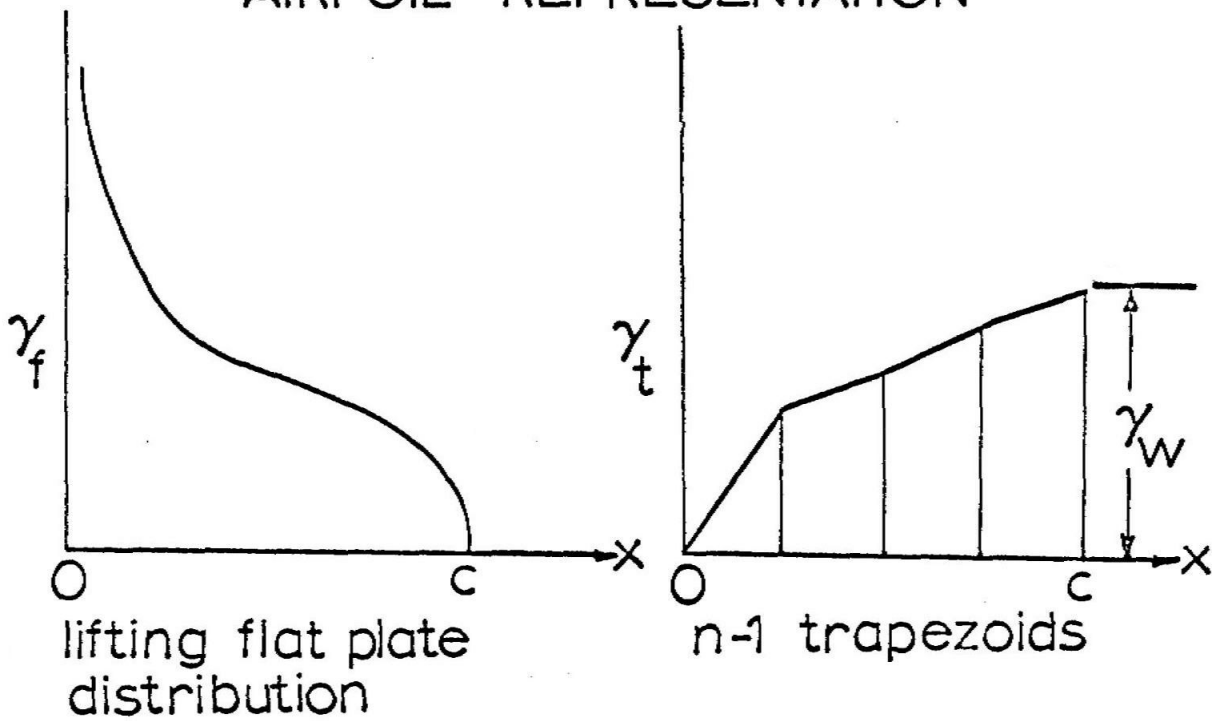

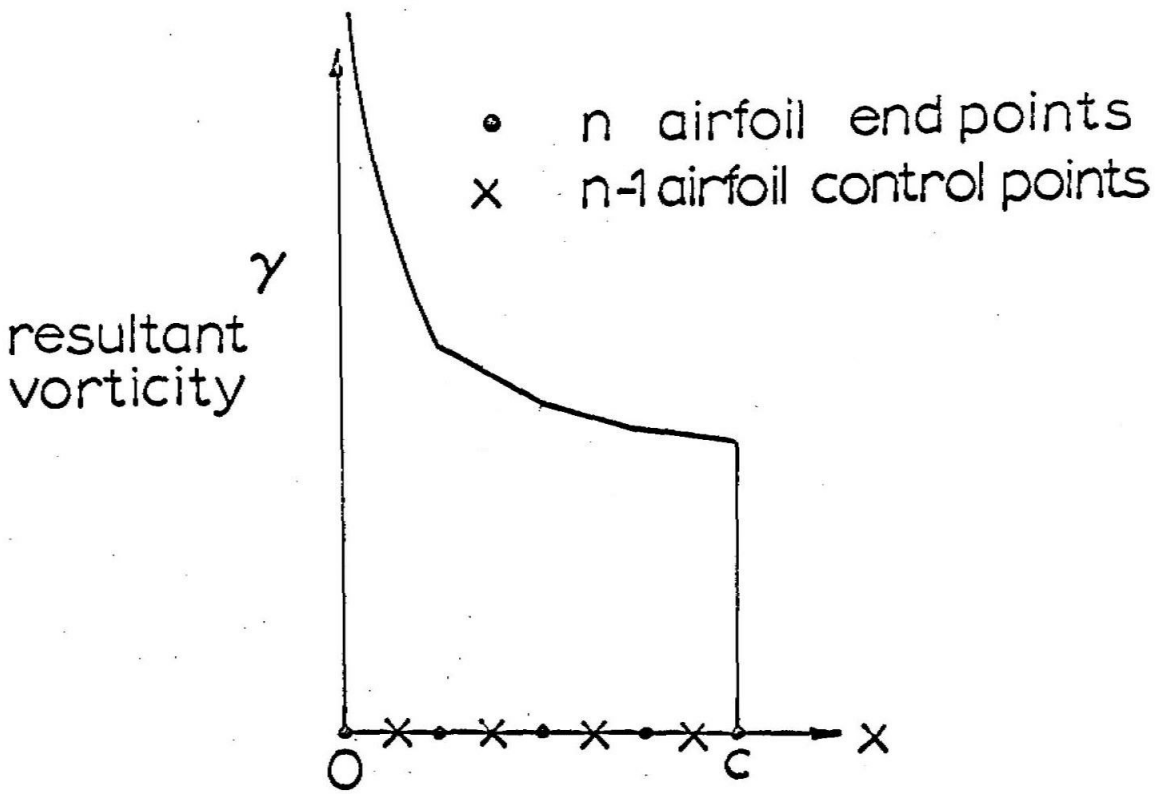

figure 10

WAKE REPRESENTATION

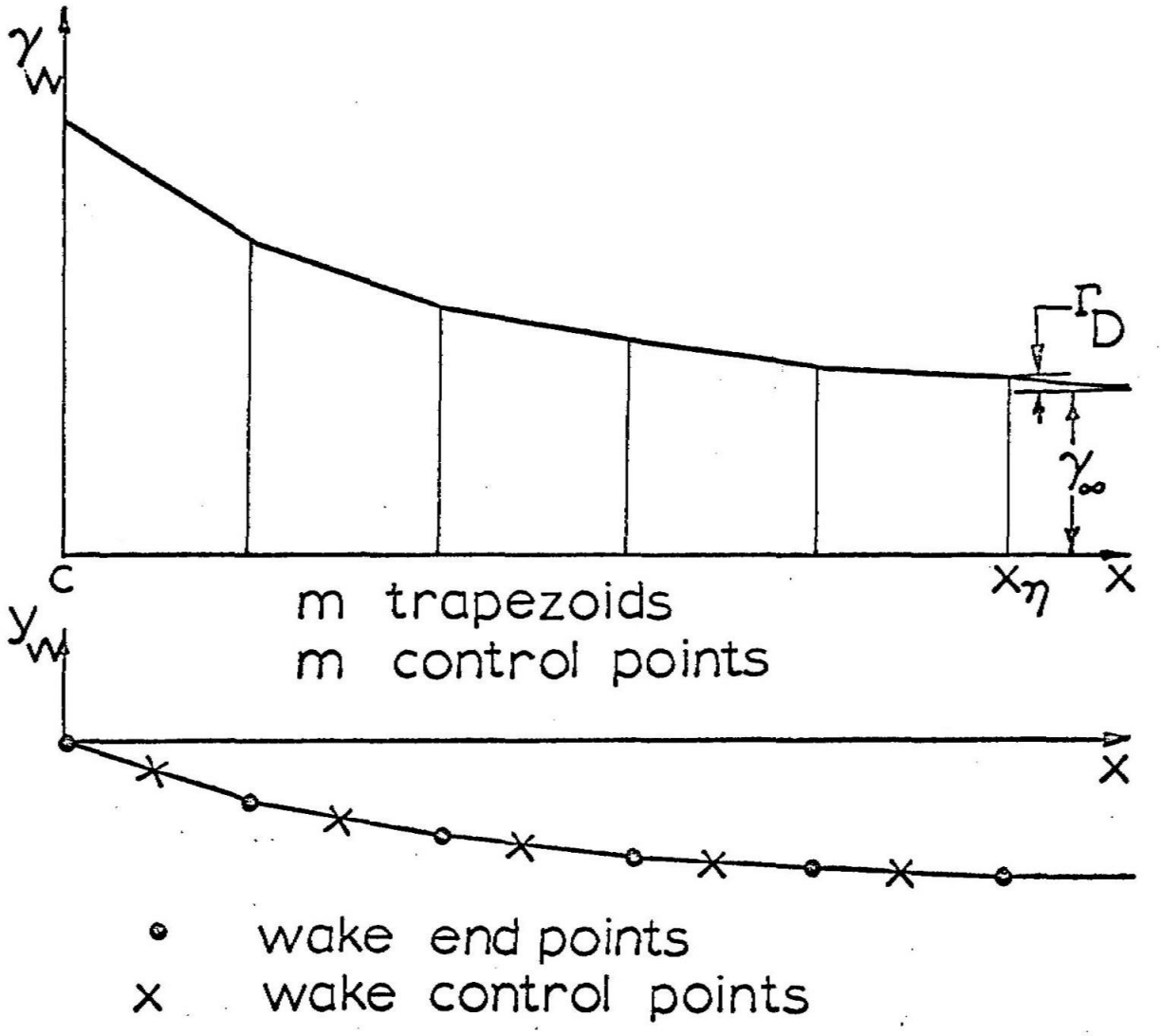

figure 11

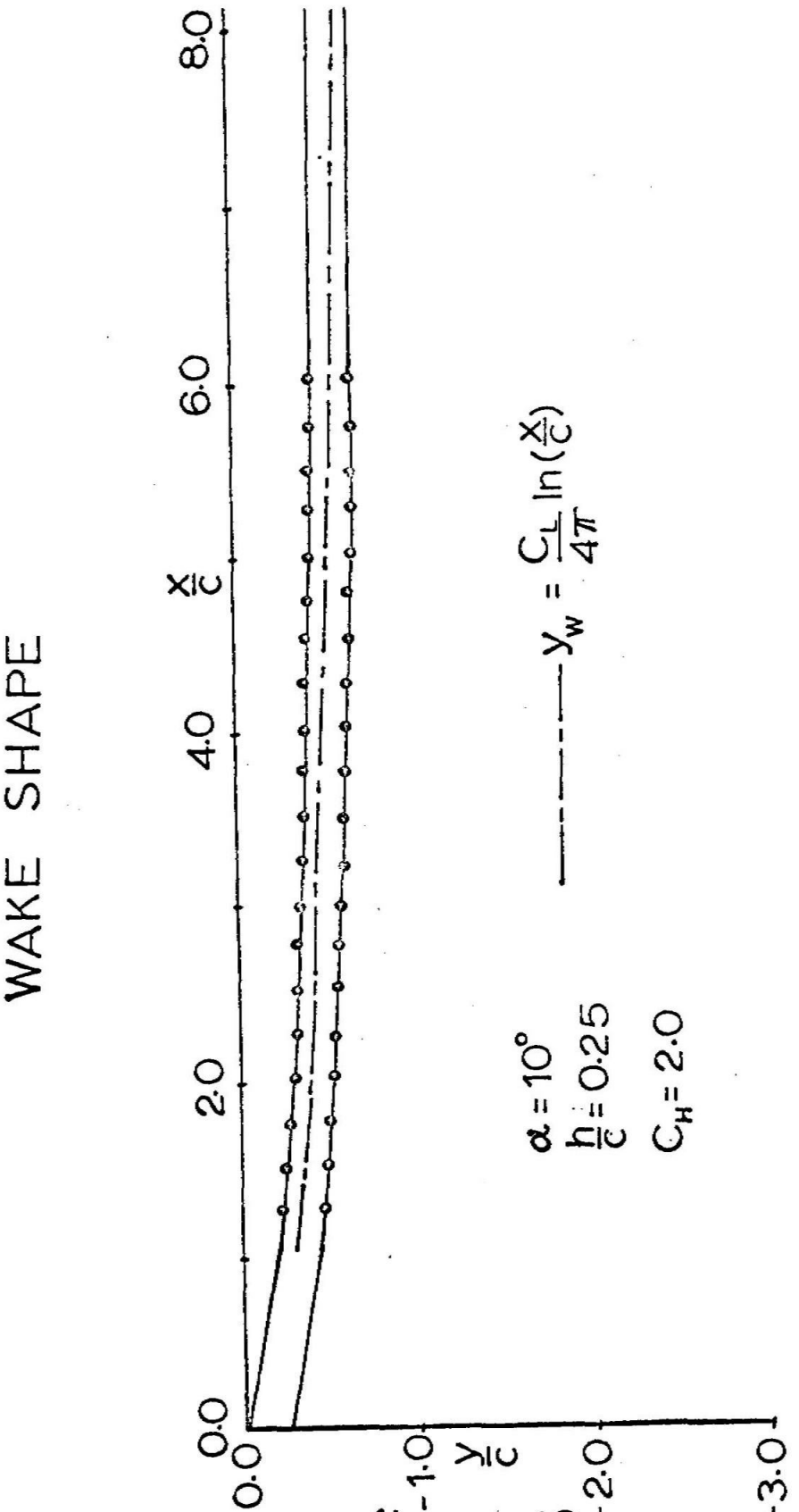
WAKE SHAPE
0.0
2.0
4.0
6.0
8.0
x/c
0.0
-1.0
-2.0
-3.0
y/c
$y_w = \frac{C_L}{4\pi} \ln(\frac{x}{c})$
$\alpha = 10°$
$\frac{h}{c} = 0.25$
$C_H = 2.0$

figure 12

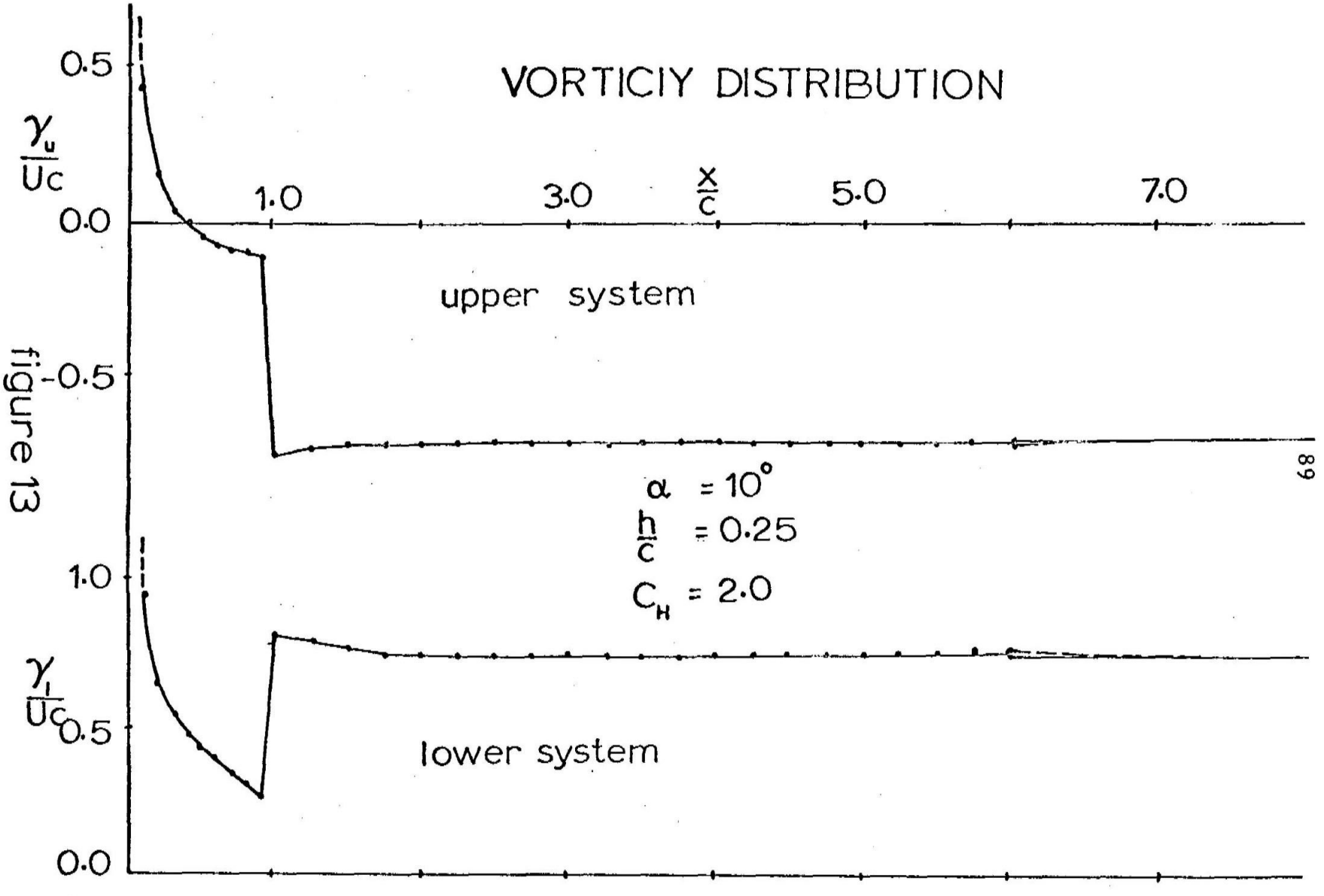
VORTICIY DISTRIBUTION
0.5
$\frac{\gamma_u}{U_c}$
0.0
1.0
3.0
$\frac{x}{c}$
5.0
7.0
upper system
-0.5
$\alpha = 10^\circ$
$\frac{h}{c} = 0.25$
$C_H = 2.0$
1.0
$\frac{\gamma_l}{U_c}$
0.5
lower system
0.0

figure 13

LIFT CURVE

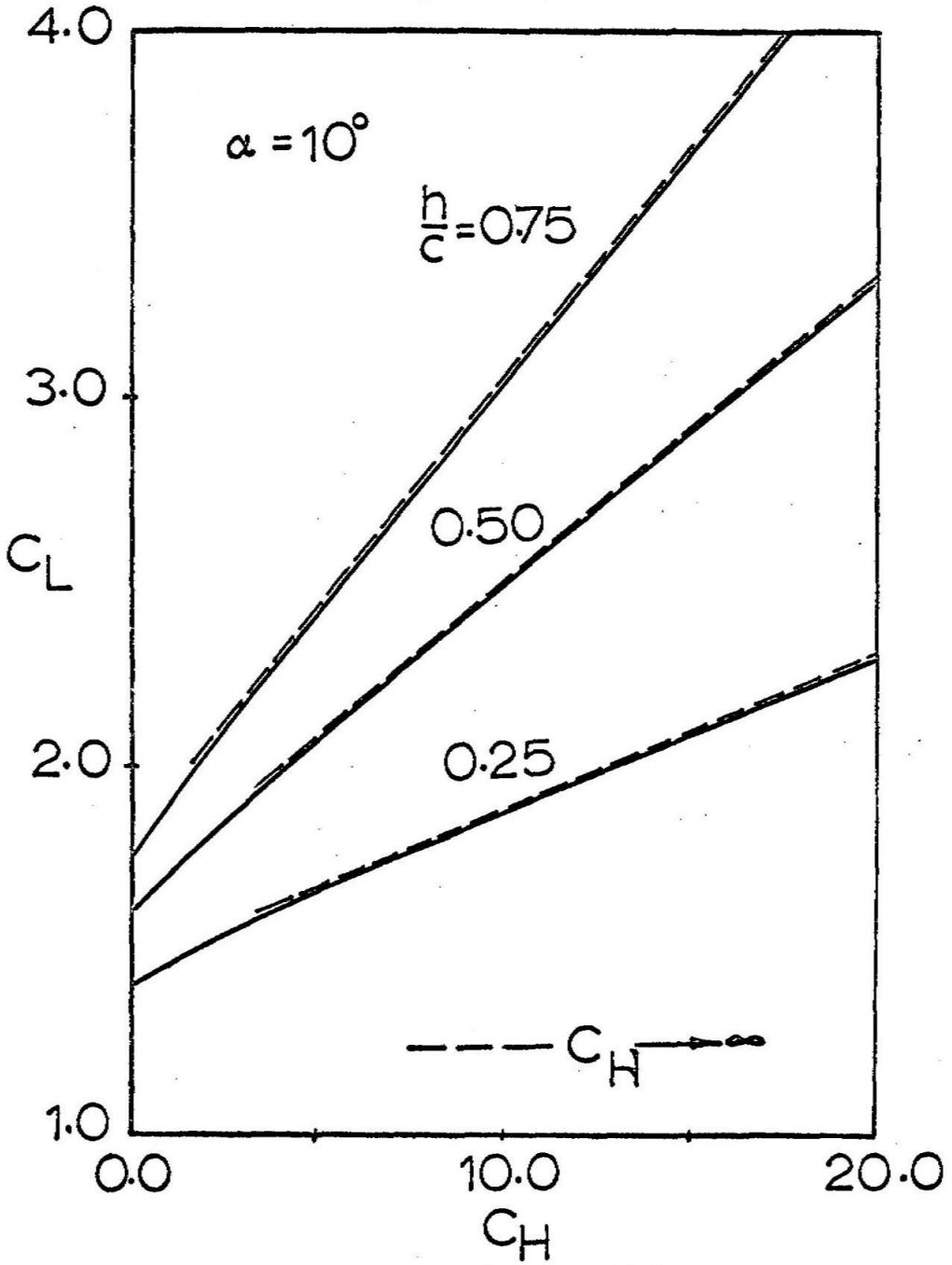

figure 14

SYSTEM THRUST

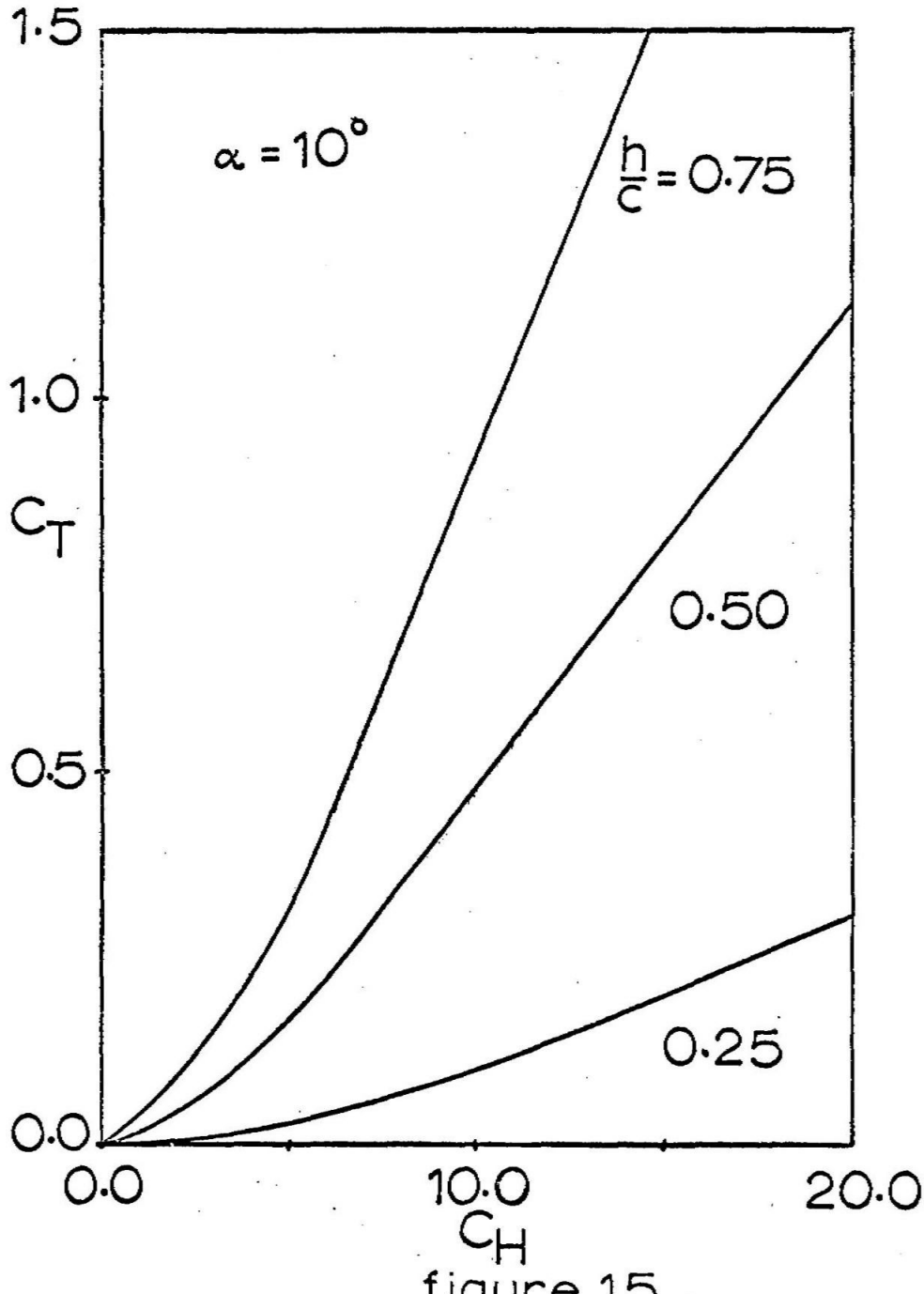

figure 15

LOWER AIRFOIL LIFT

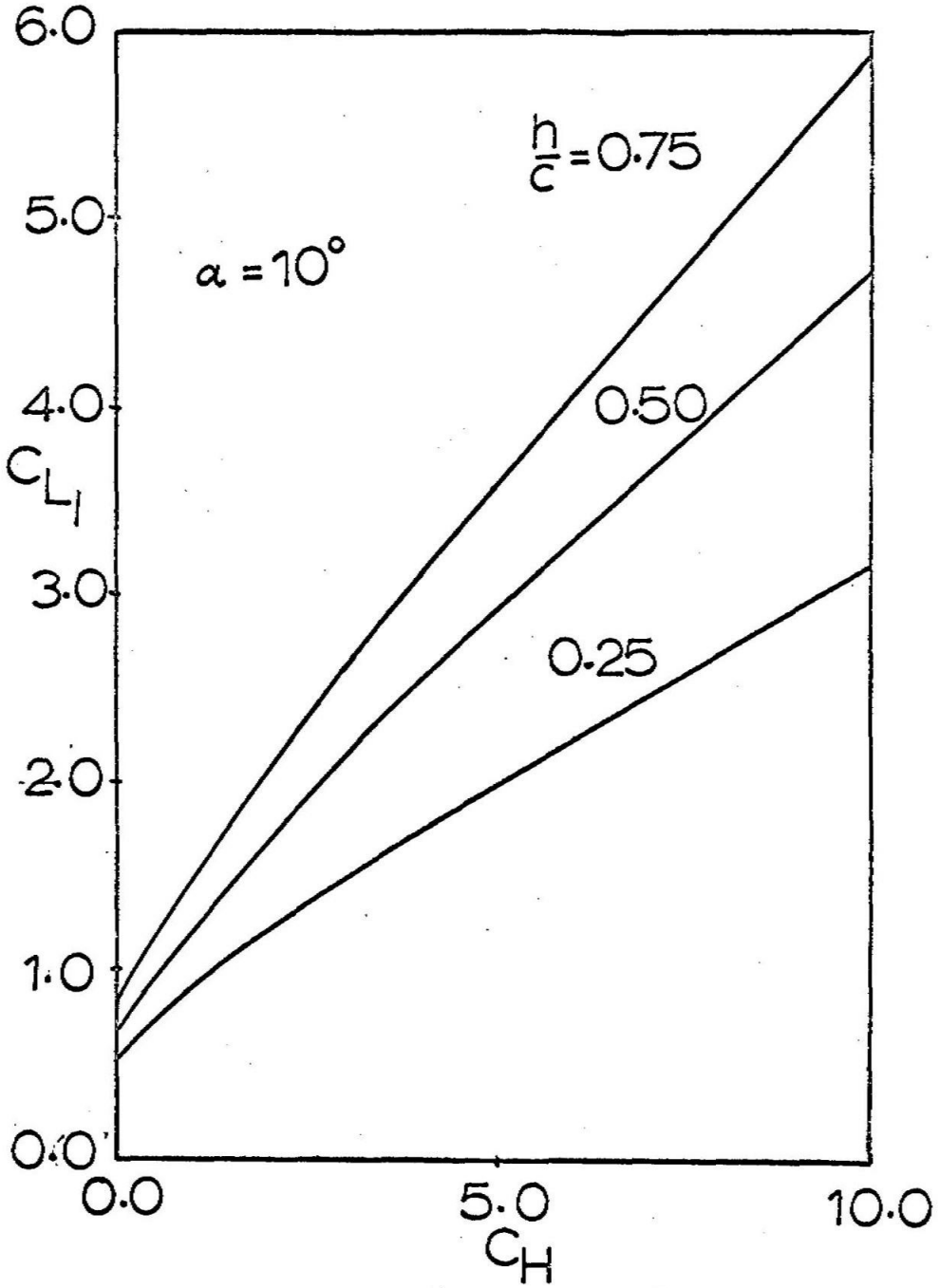

figure 16

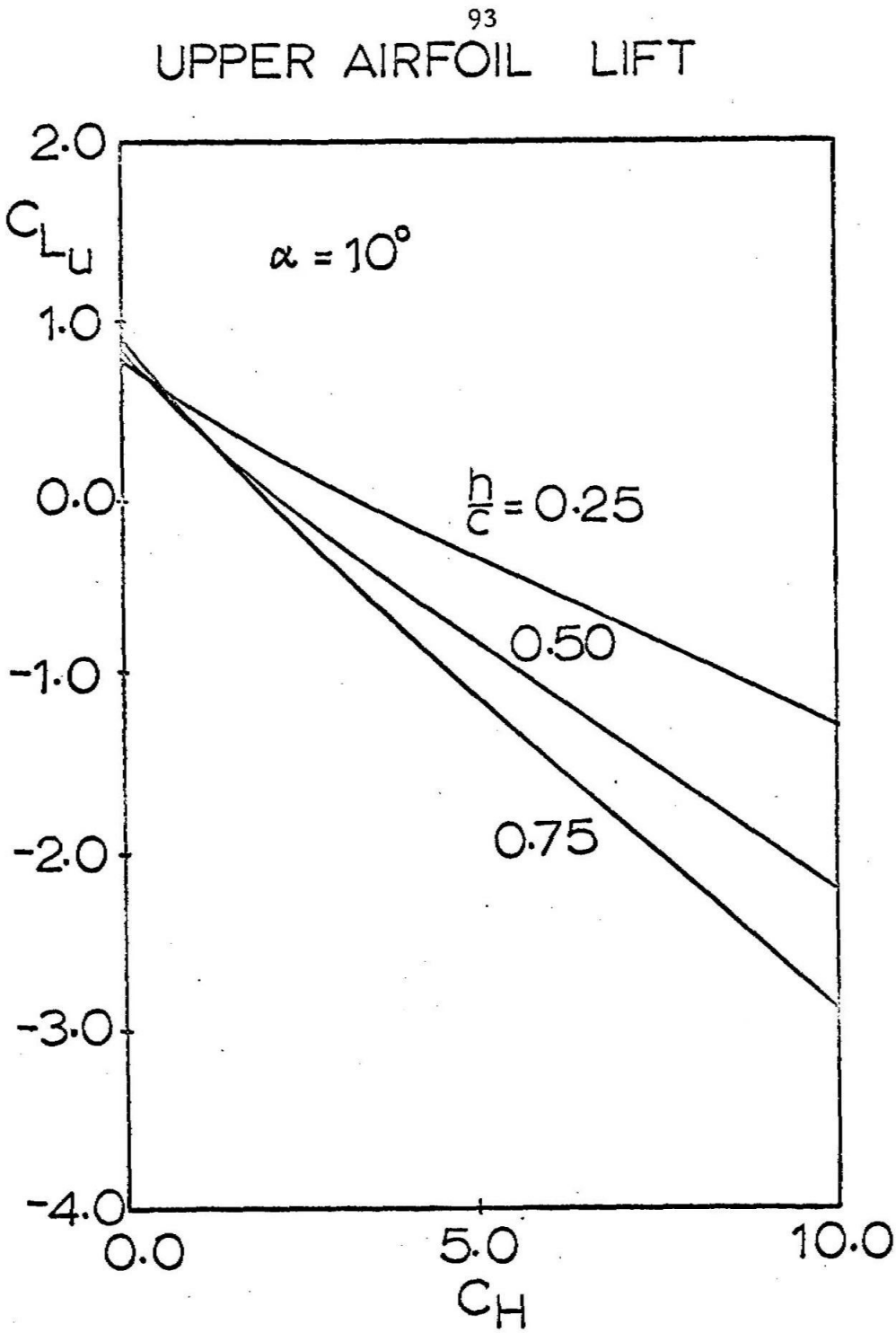
UPPER AIRFOIL LIFT
2.0
C_{L_u}
$\alpha = 10°$
1.0
0.0
$\frac{h}{c} = 0.25$
0.50
-1.0
0.75
-2.0
-3.0
-4.0
0.0
5.0
10.0
C_H

figure 17

LOWER AIRFOIL PITCHING MOMENT

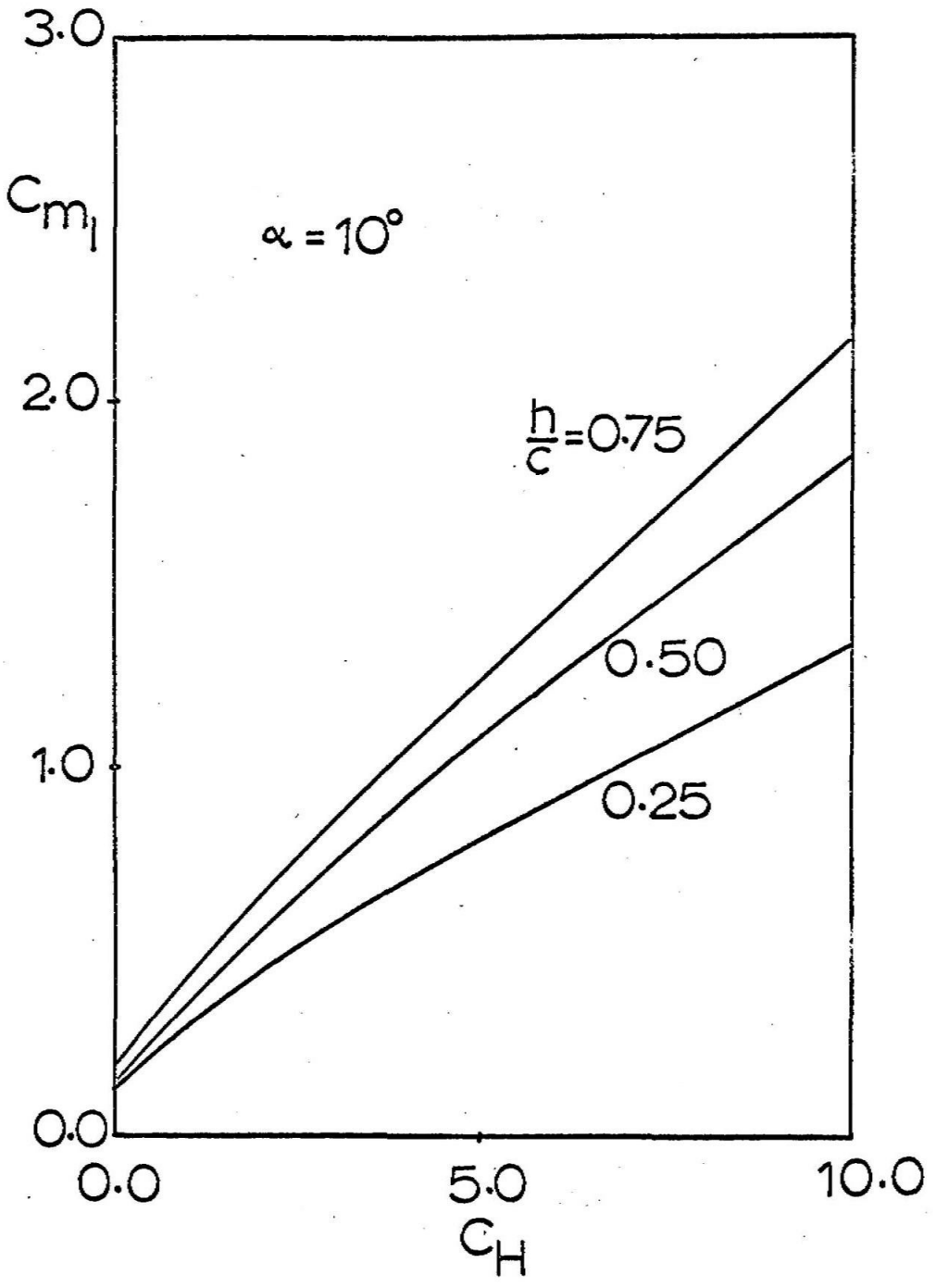

figure 18

UPPER AIRFOIL PITCHING MOMENT

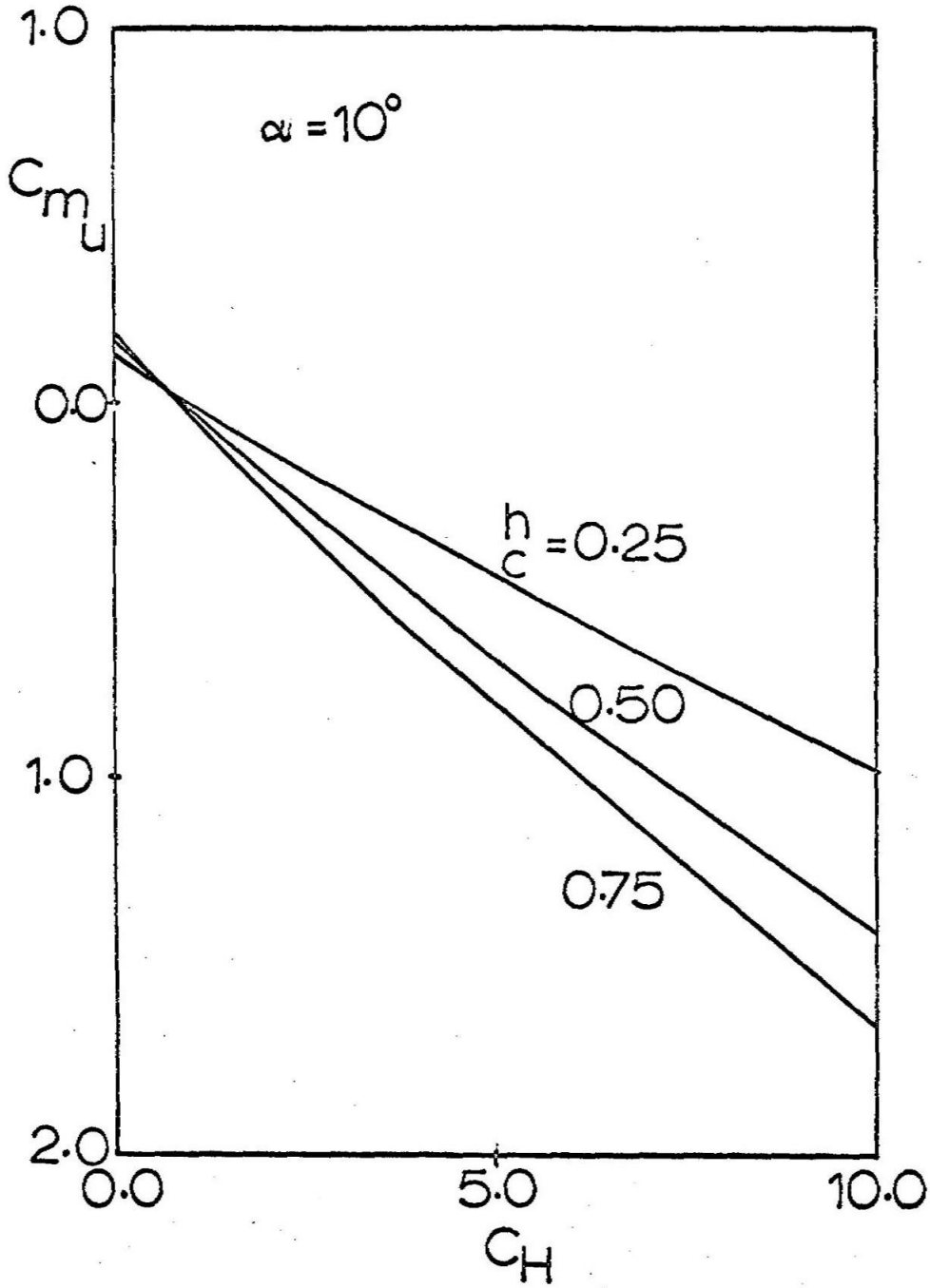

figure 19

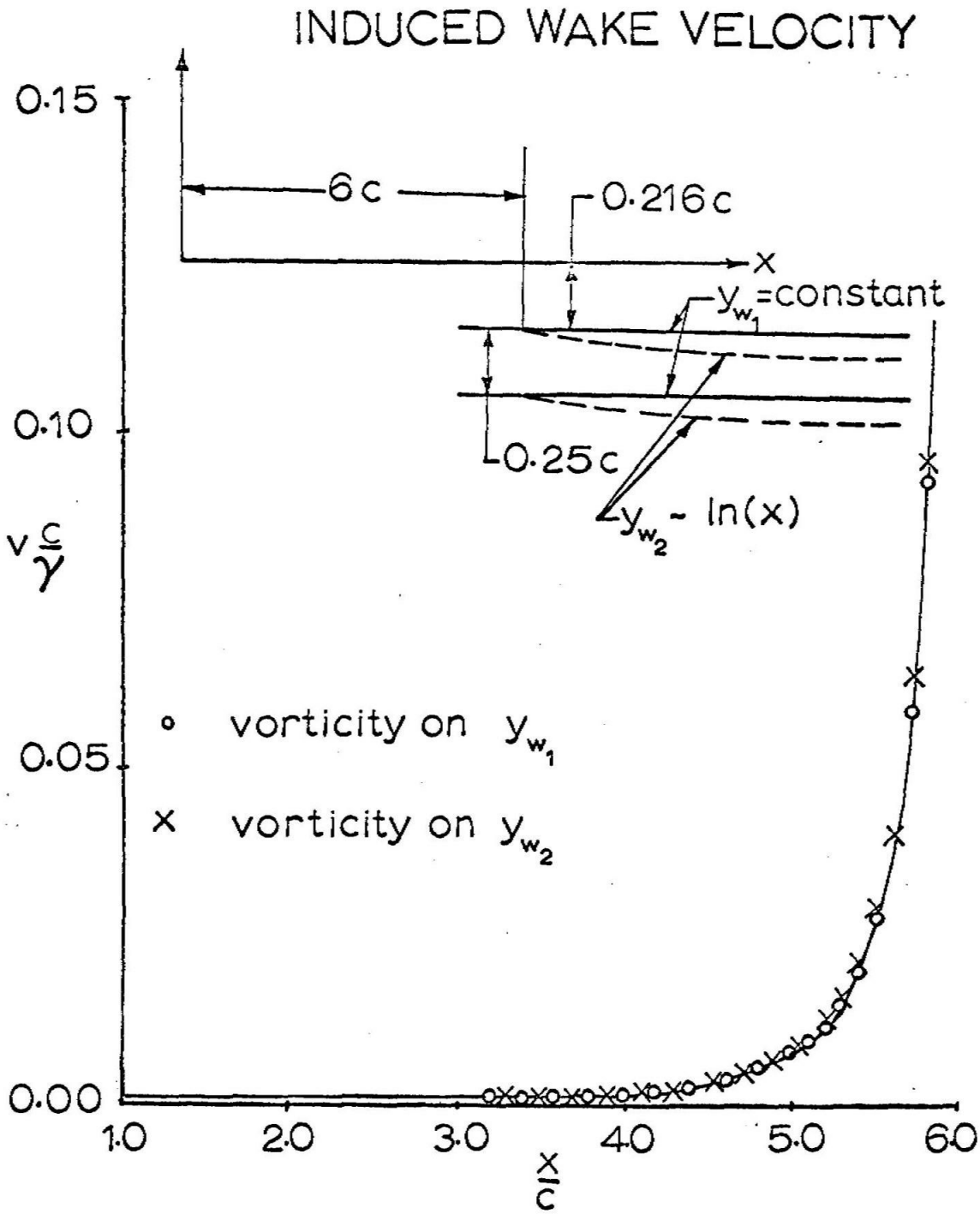
INDUCED WAKE VELOCITY
0.15
0.10
0.05
0.00
6c
0.216c
x
y_{w_1}=constant
0.25c
y_{w_2} ~ ln(x)
$\frac{v}{\gamma}\frac{c}{}$
o vorticity on y_{w_1}
x vorticity on y_{w_2}
1.0
2.0
3.0
4.0
5.0
6.0
$\frac{x}{c}$

figure 20

COMPARISON OF SOLUTIONS

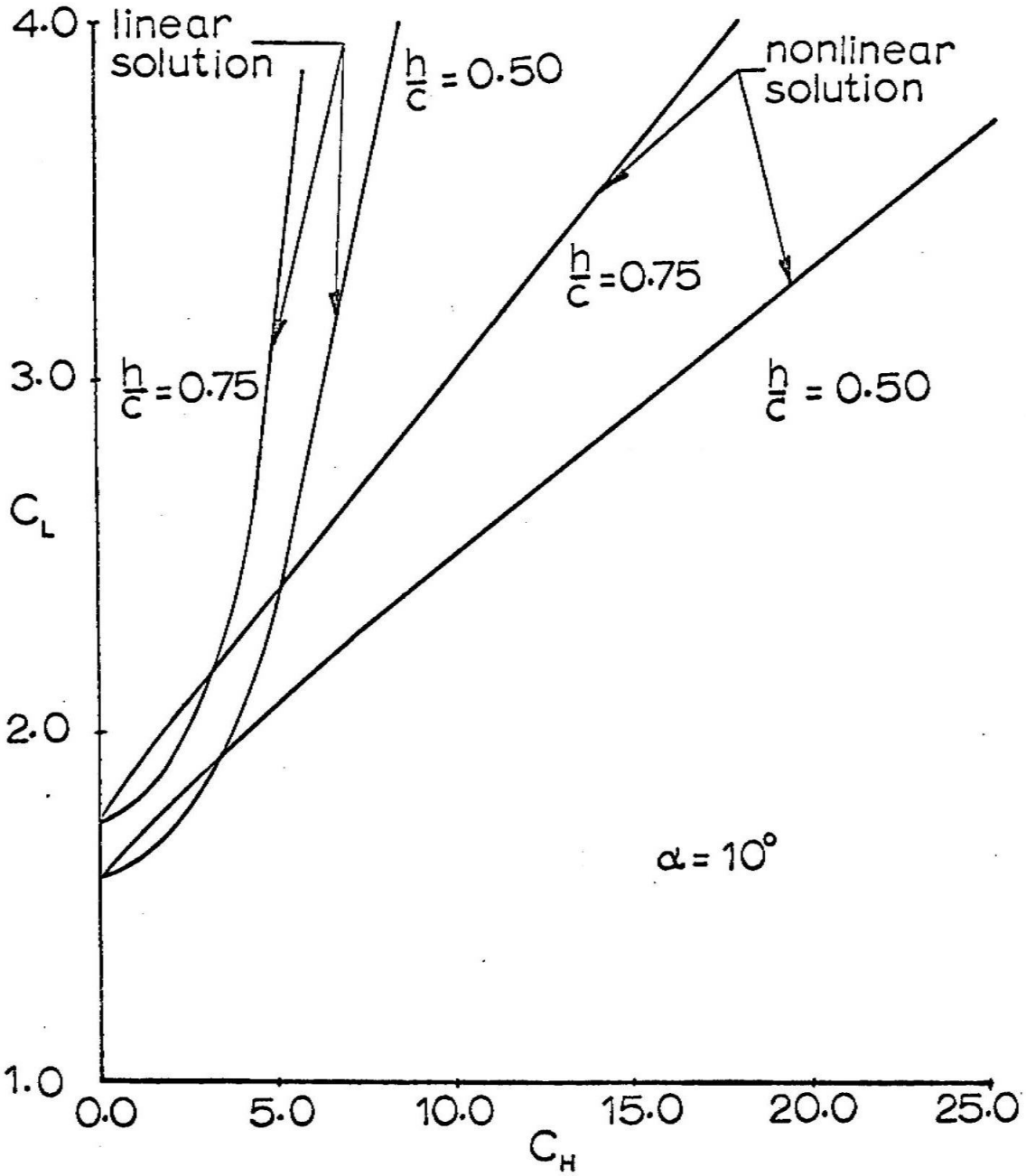

figure 21

UNEQUAL CHORD SYSTEM LIFT

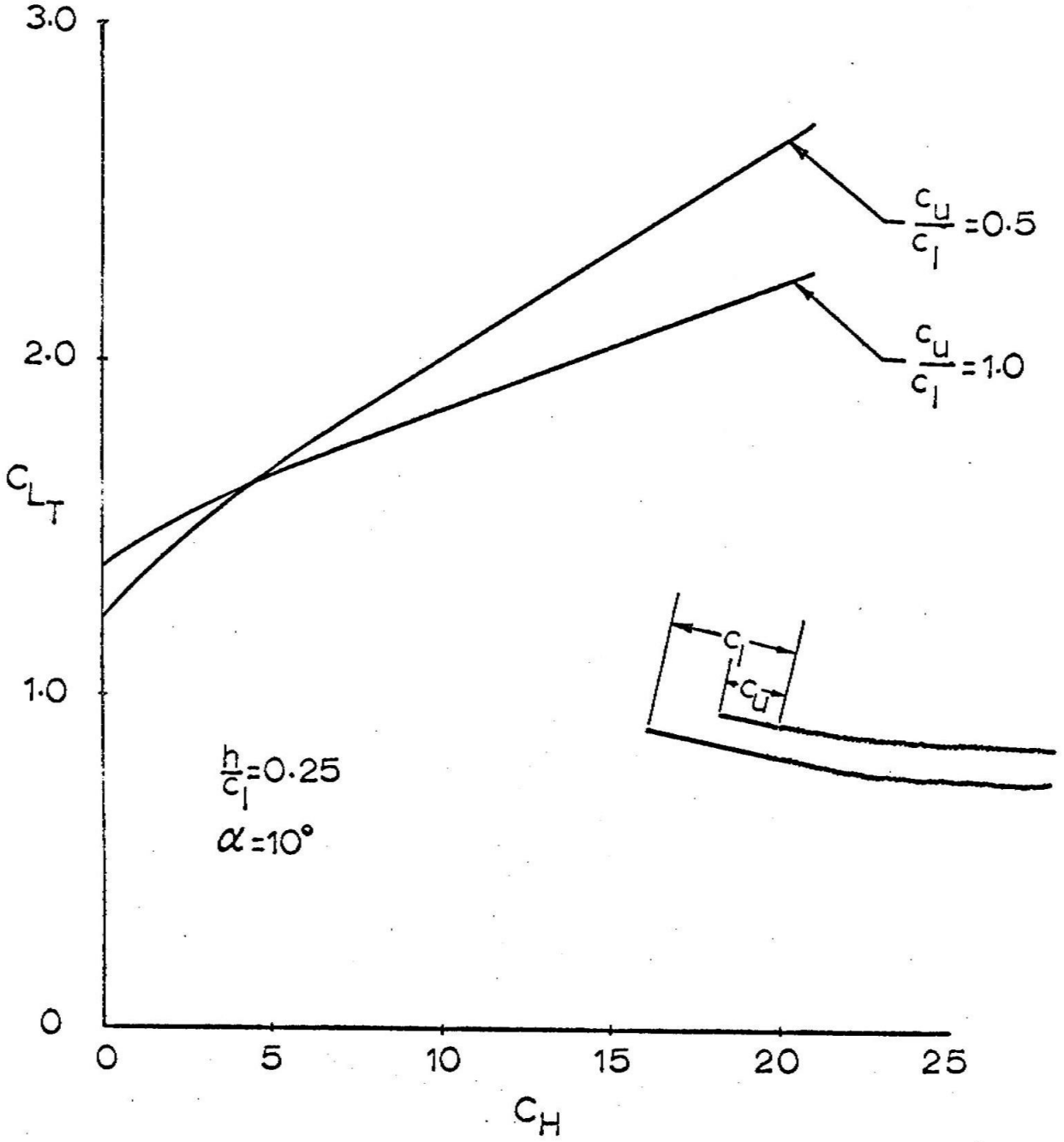

figure 22

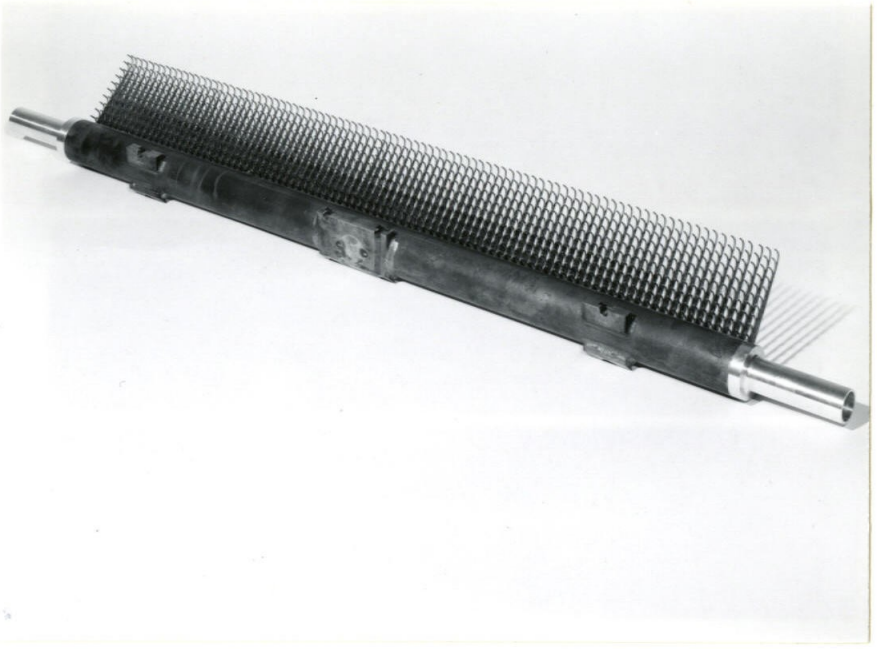

Ejector Assembly

Side View of Wind Tunnel Model

figure 23

WIND TUNNEL MODEL

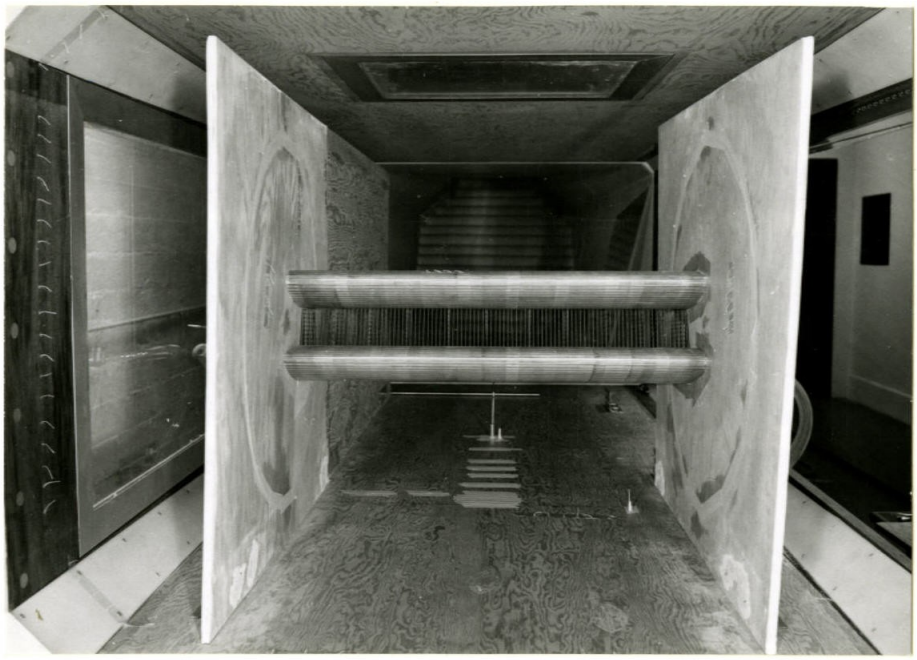

Front View

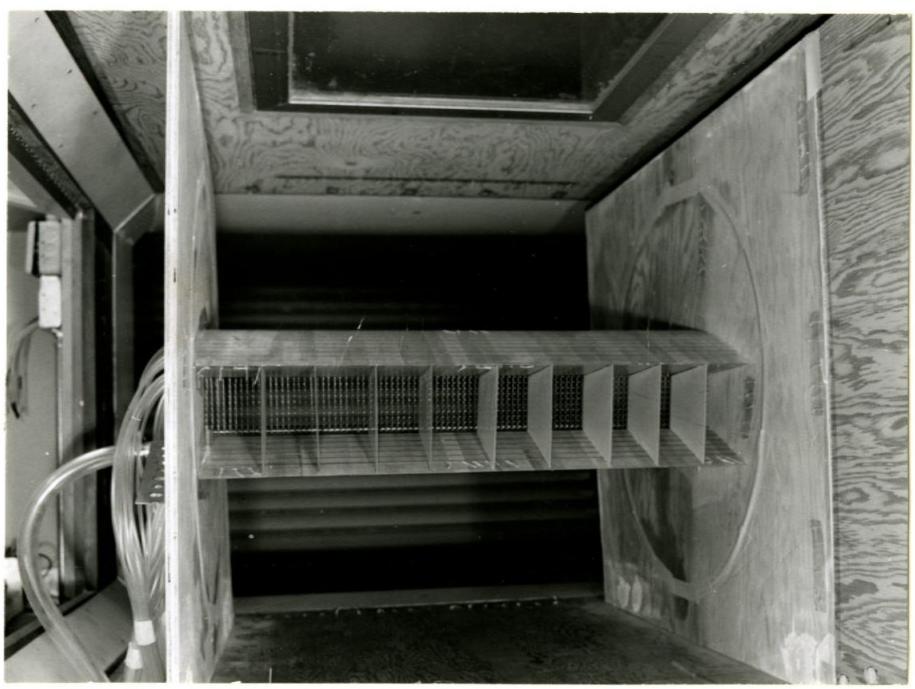

Rear View

figure 24

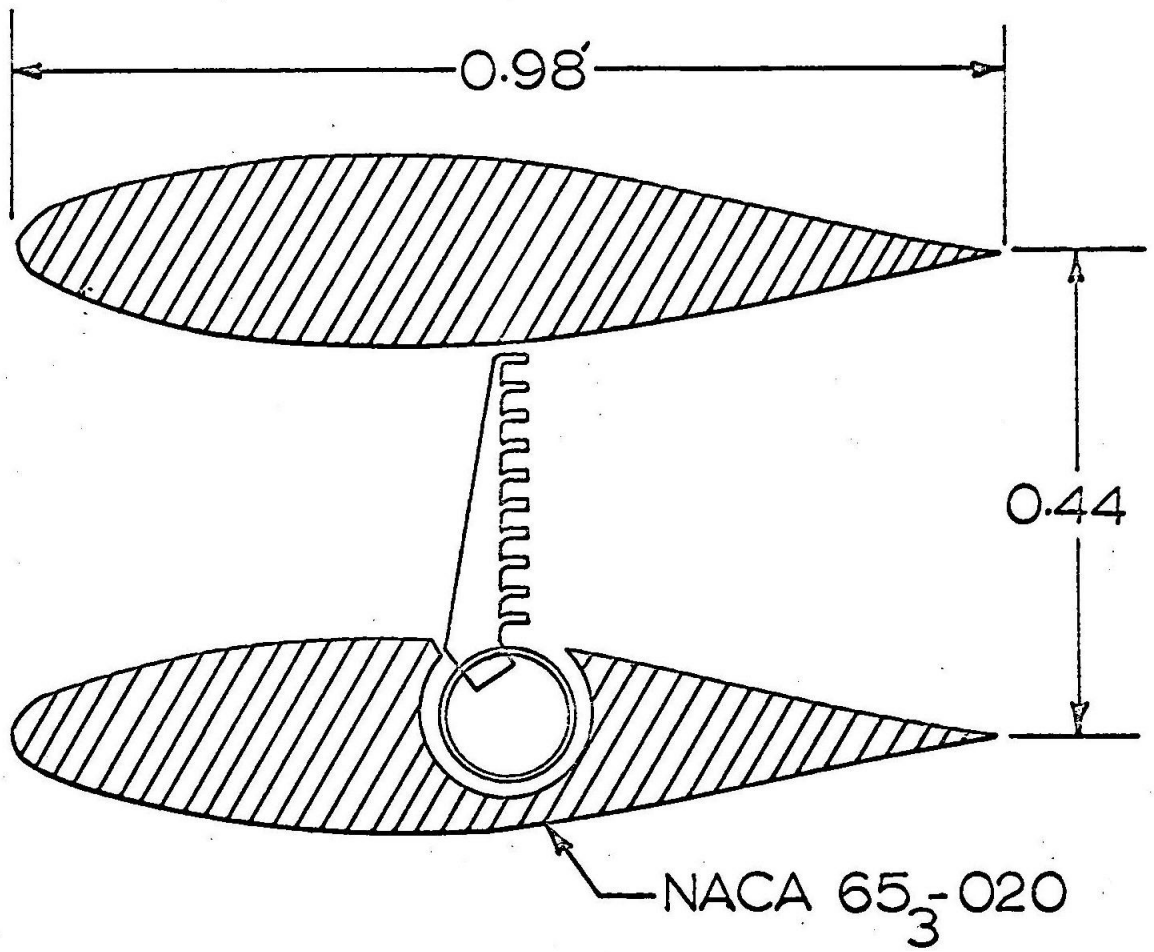

MODEL CROSS SECTION

figure 25

SPANWISE UNIFORMITY

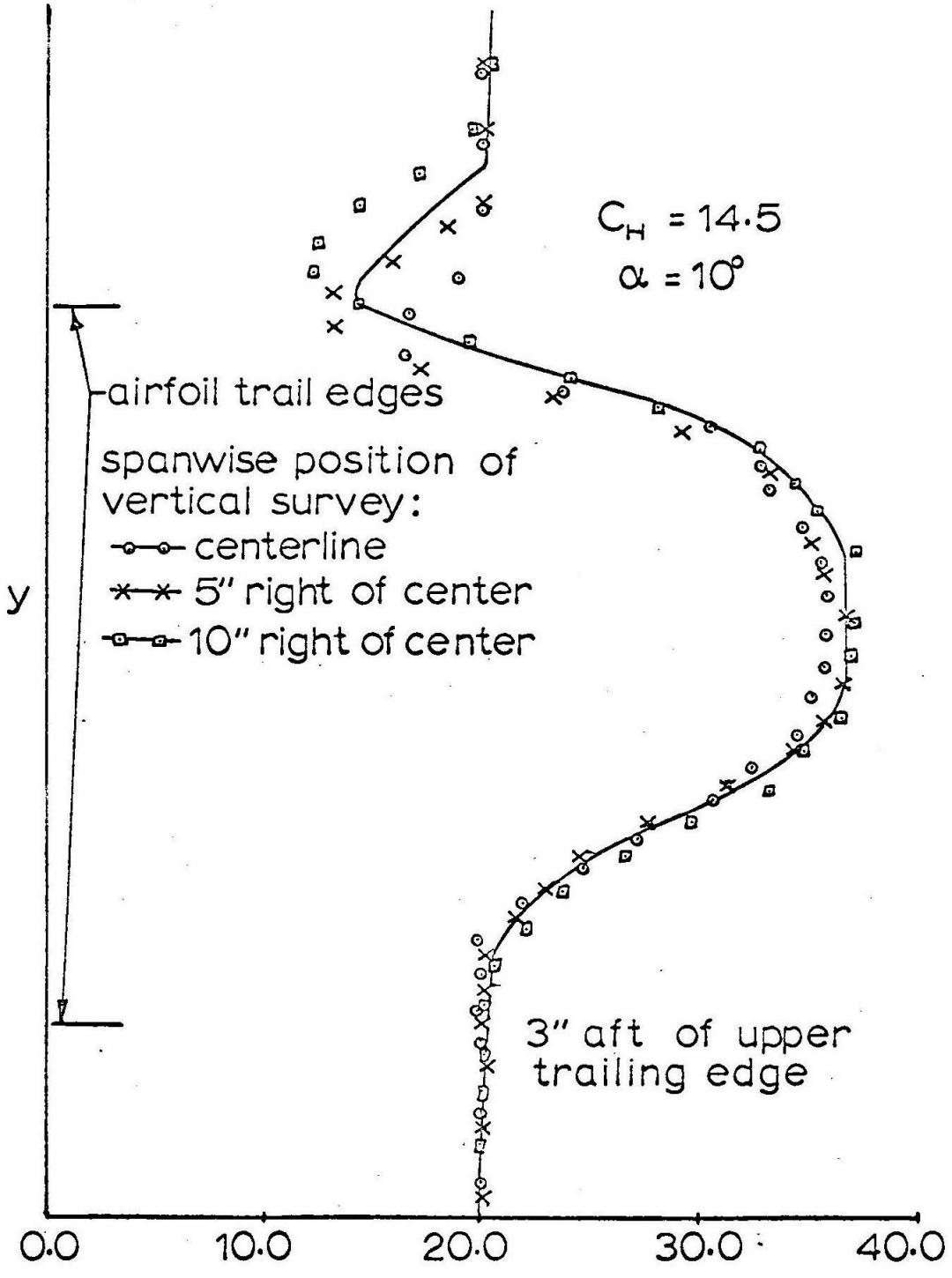

figure 26

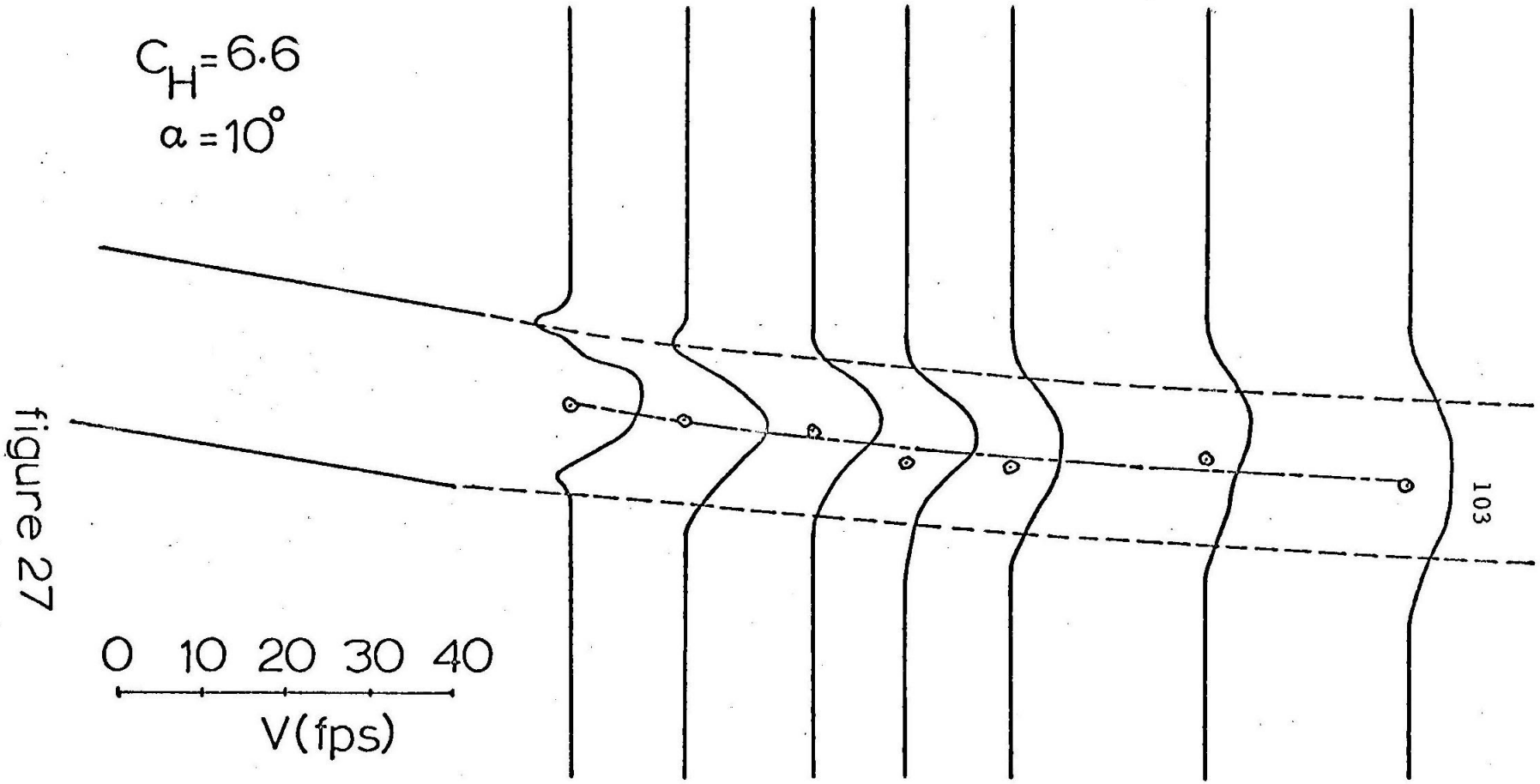

figure 27

calculated boundary

center of momentum

WAKE VELOCITIES

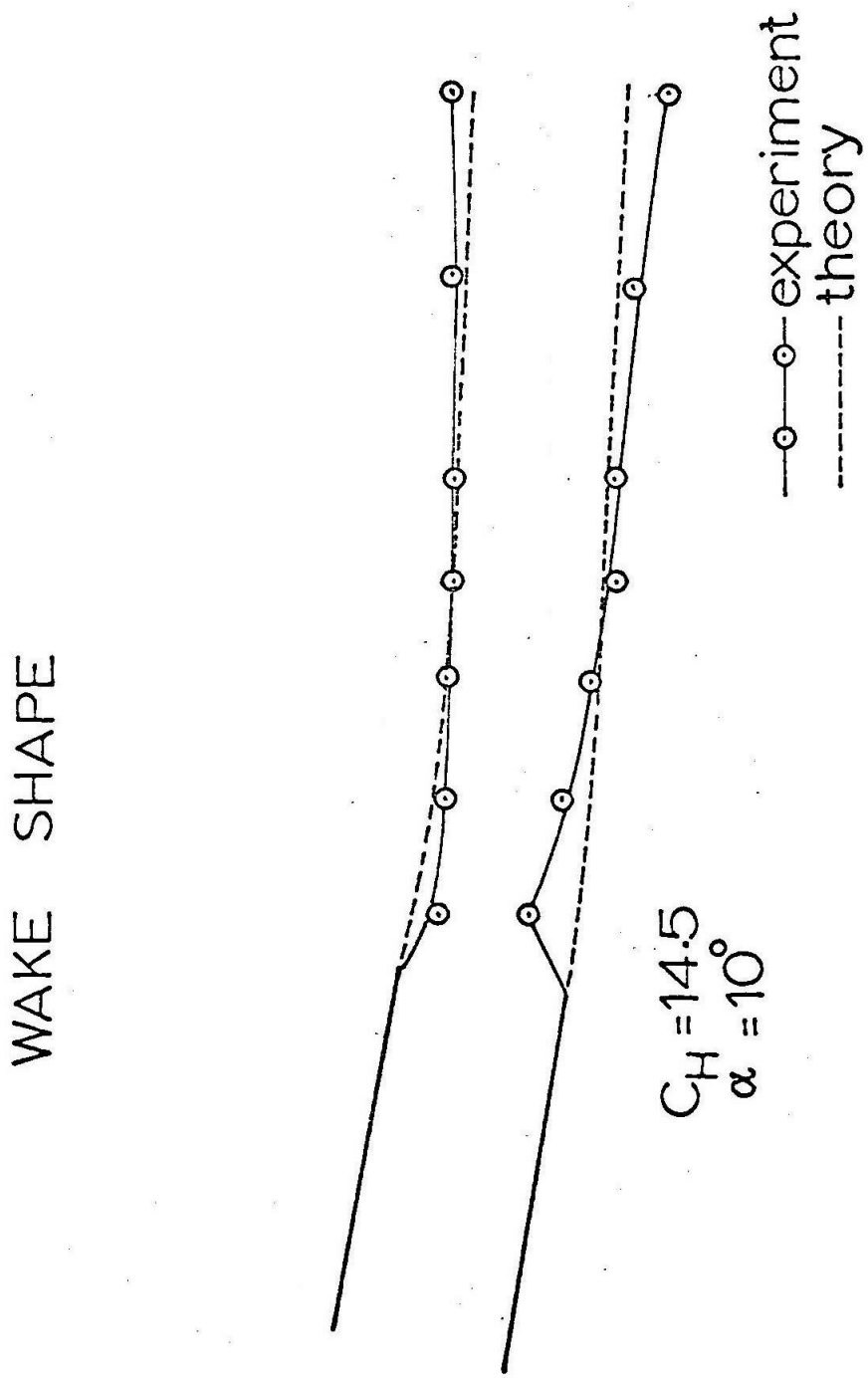

figure 28

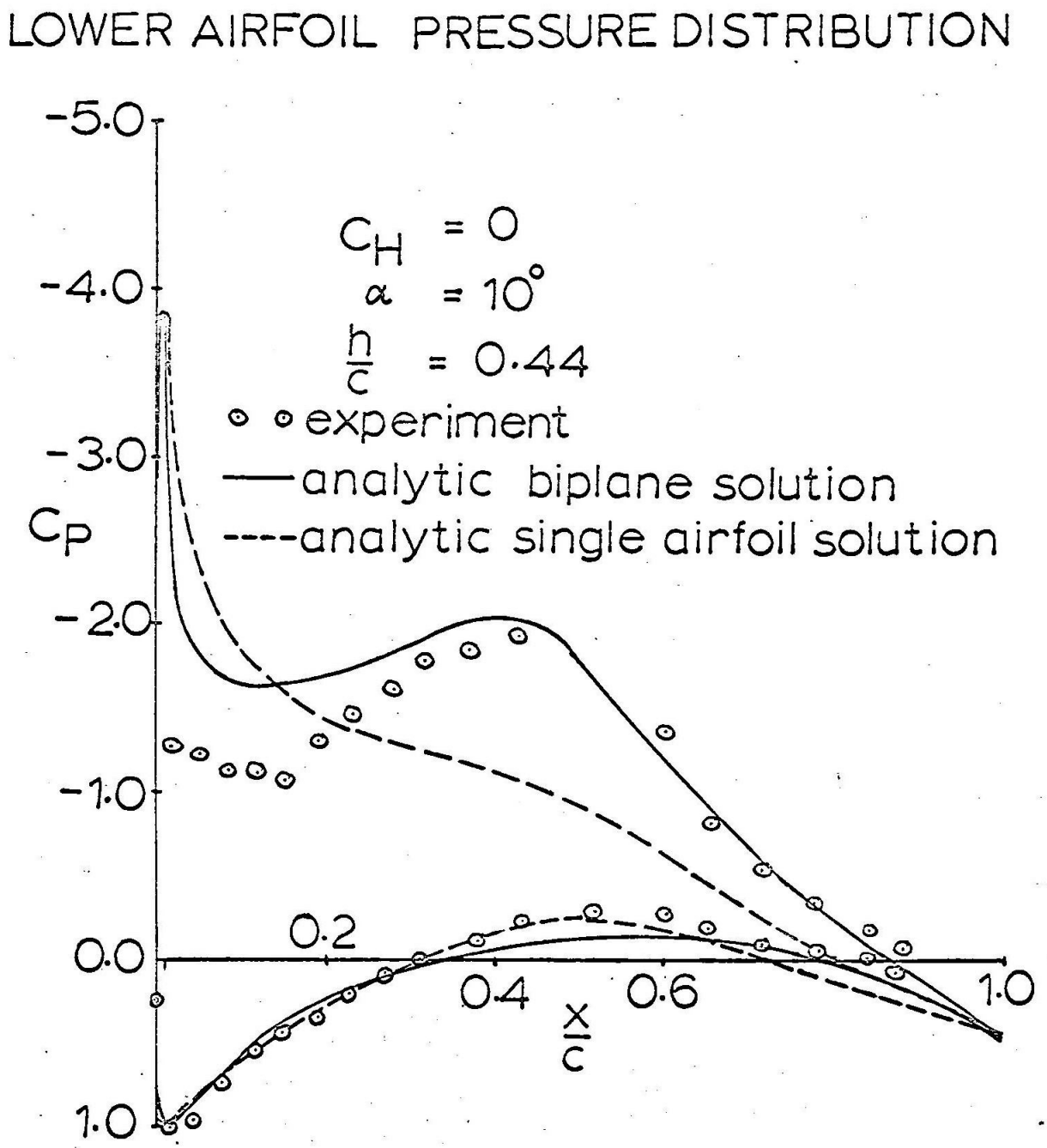
LOWER AIRFOIL PRESSURE DISTRIBUTION
-5.0
-4.0
-3.0
-2.0
-1.0
0.0
1.0
C_P
$C_H = 0$
$\alpha = 10^\circ$
$\frac{h}{c} = 0.44$
experiment
analytic biplane solution
analytic single airfoil solution
0.2
0.4
0.6
1.0
$\frac{x}{c}$

figure 29

UPPER AIRFOIL PRESSURE DISTRIBUTION

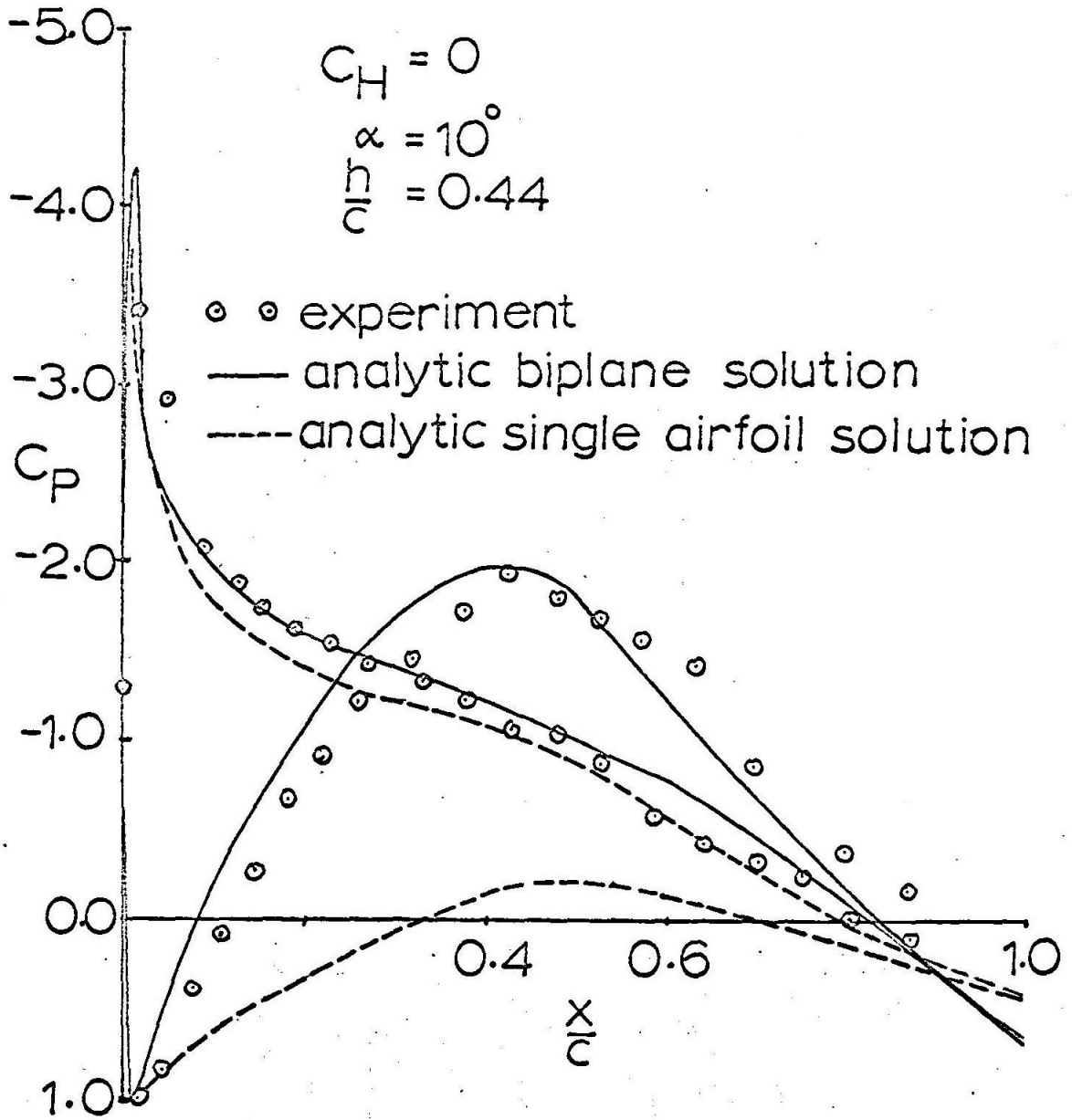

figure 30

LOWER AIRFOIL PRESSURE DISTRIBUTION

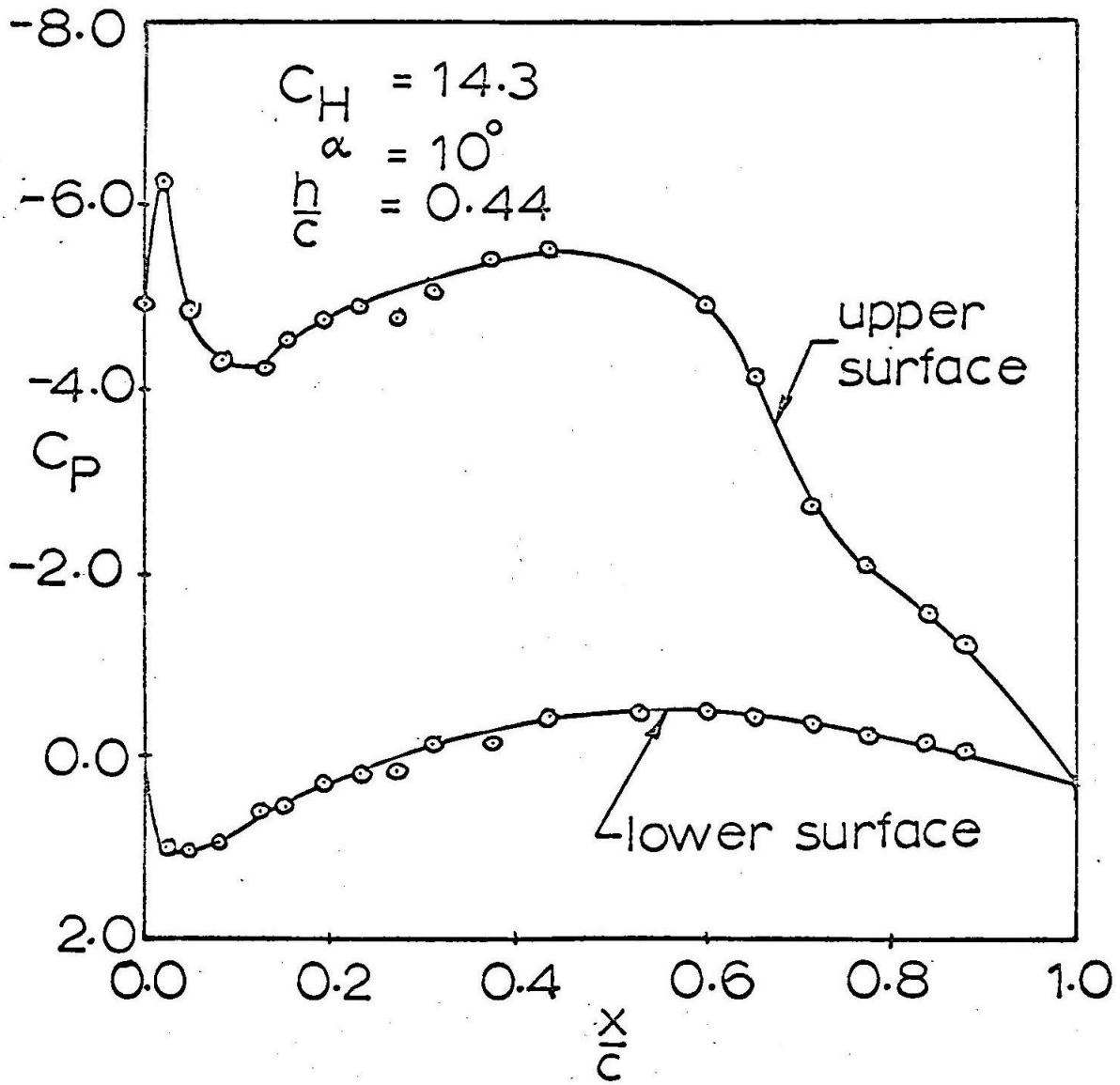

figure 31

UPPER AIRFOIL PRESSURE DISTRIBUTION

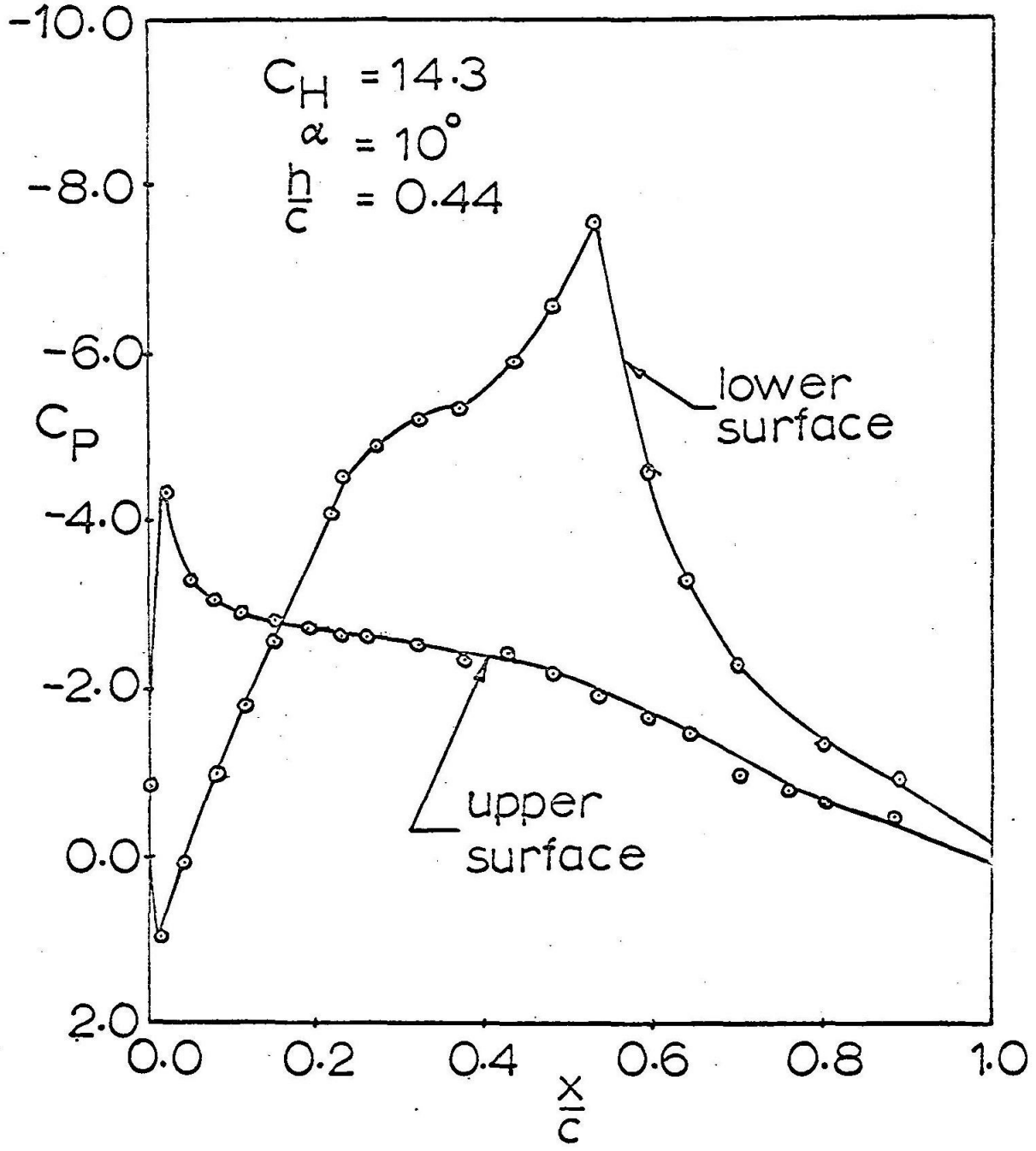

figure 32

LOWER AIRFOIL LOAD DISTRIBUTION

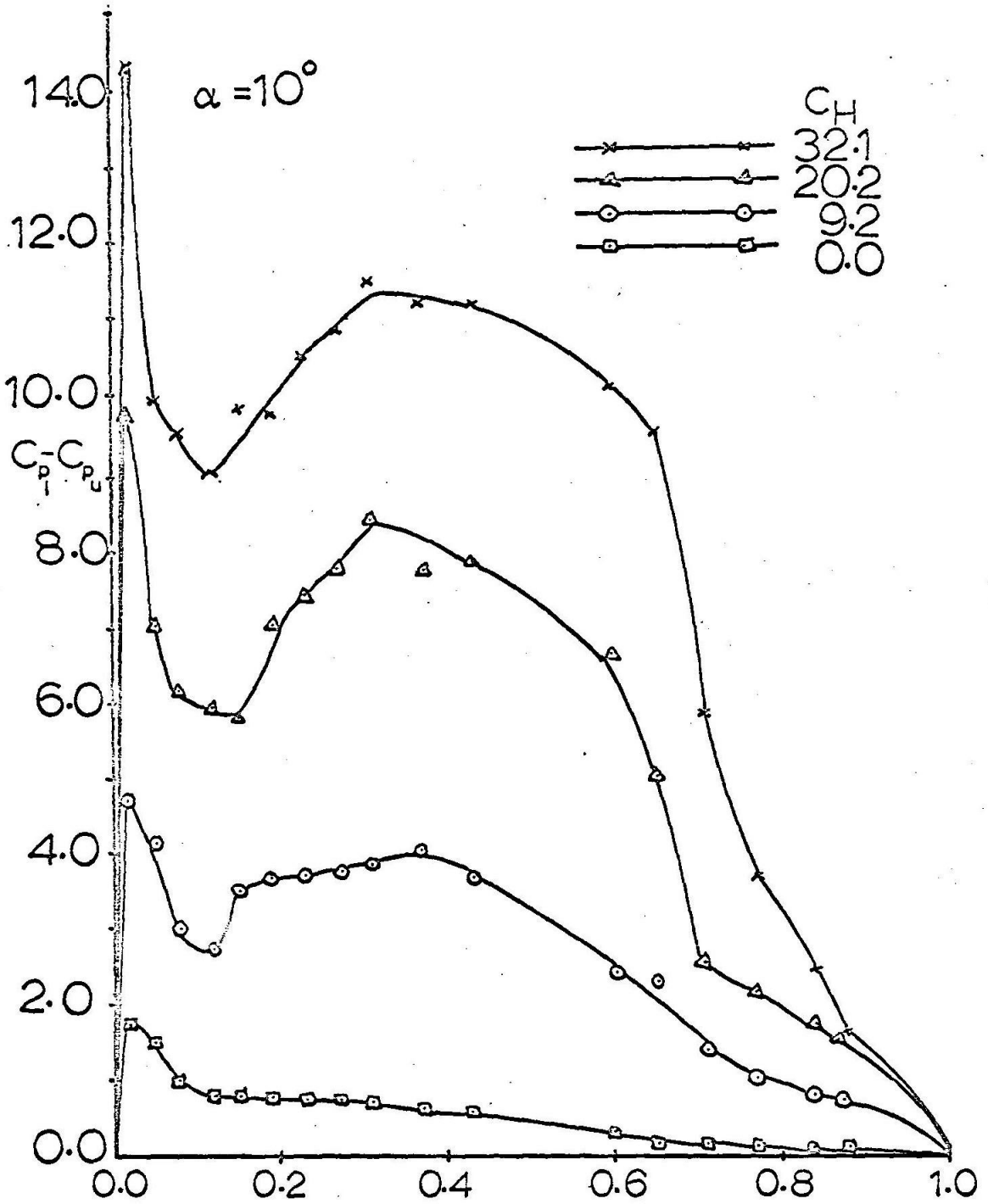

figure 33

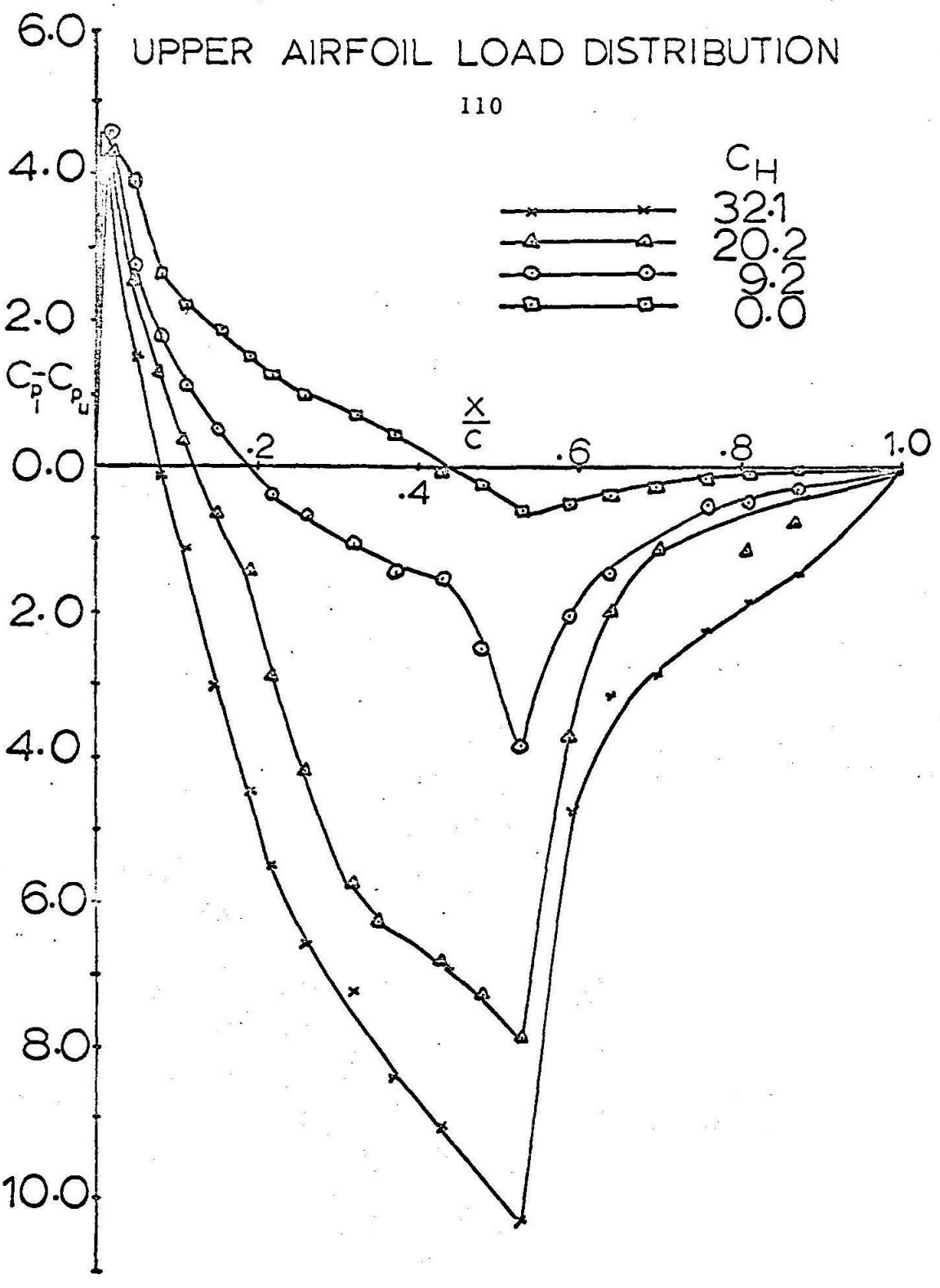
UPPER AIRFOIL LOAD DISTRIBUTION
110
C_H
32.1
20.2
9.2
0.0
$C_{p_l} - C_{p_u}$
$\frac{x}{c}$
6.0
4.0
2.0
0.0
2.0
4.0
6.0
8.0
10.0
.2
.4
.6
.8
1.0

figure 34

TOTAL LIFT

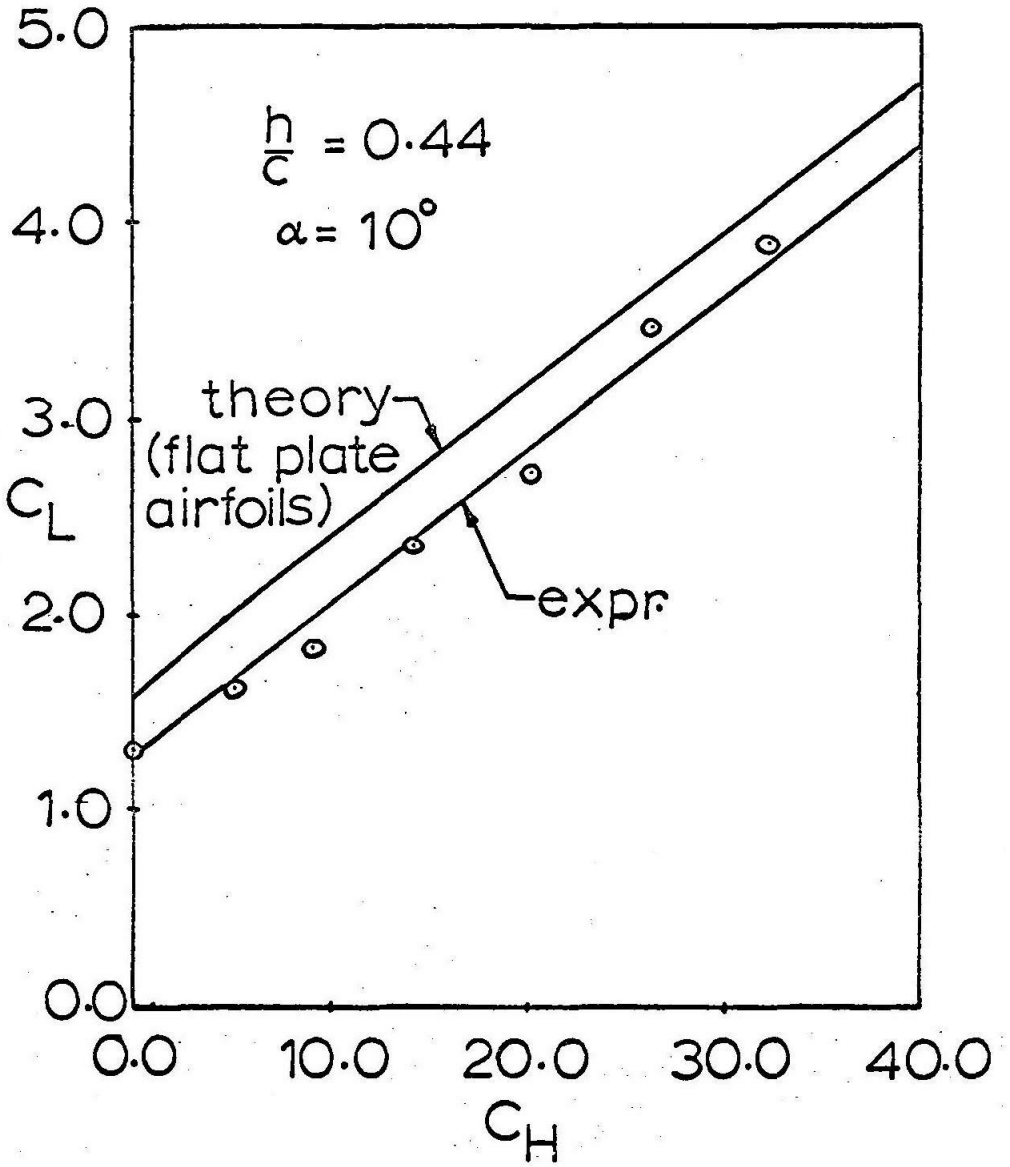

figure 35

LIFT SLOPE

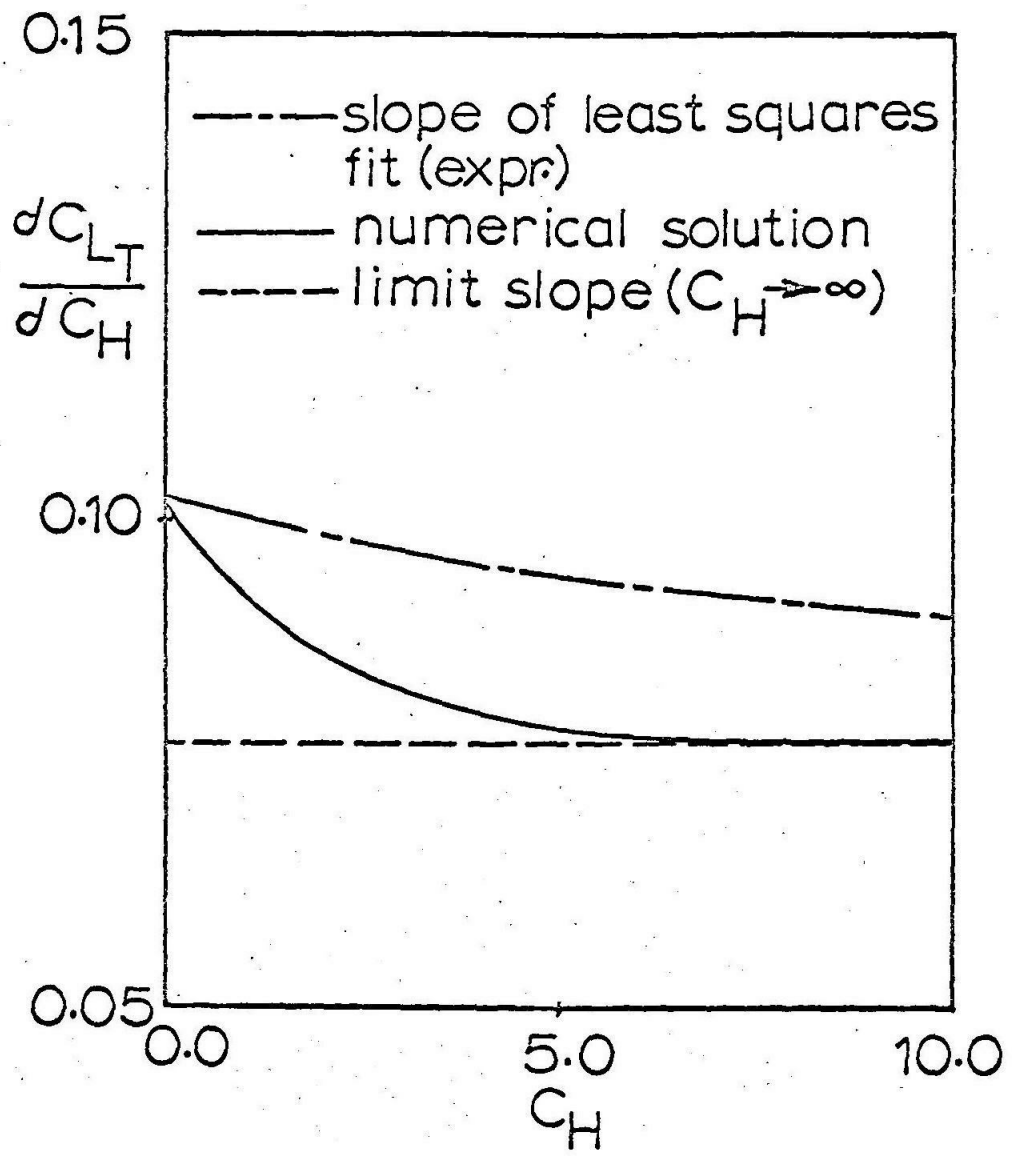

figure 36

LOWER AIRFOIL PITCHING MOMENT

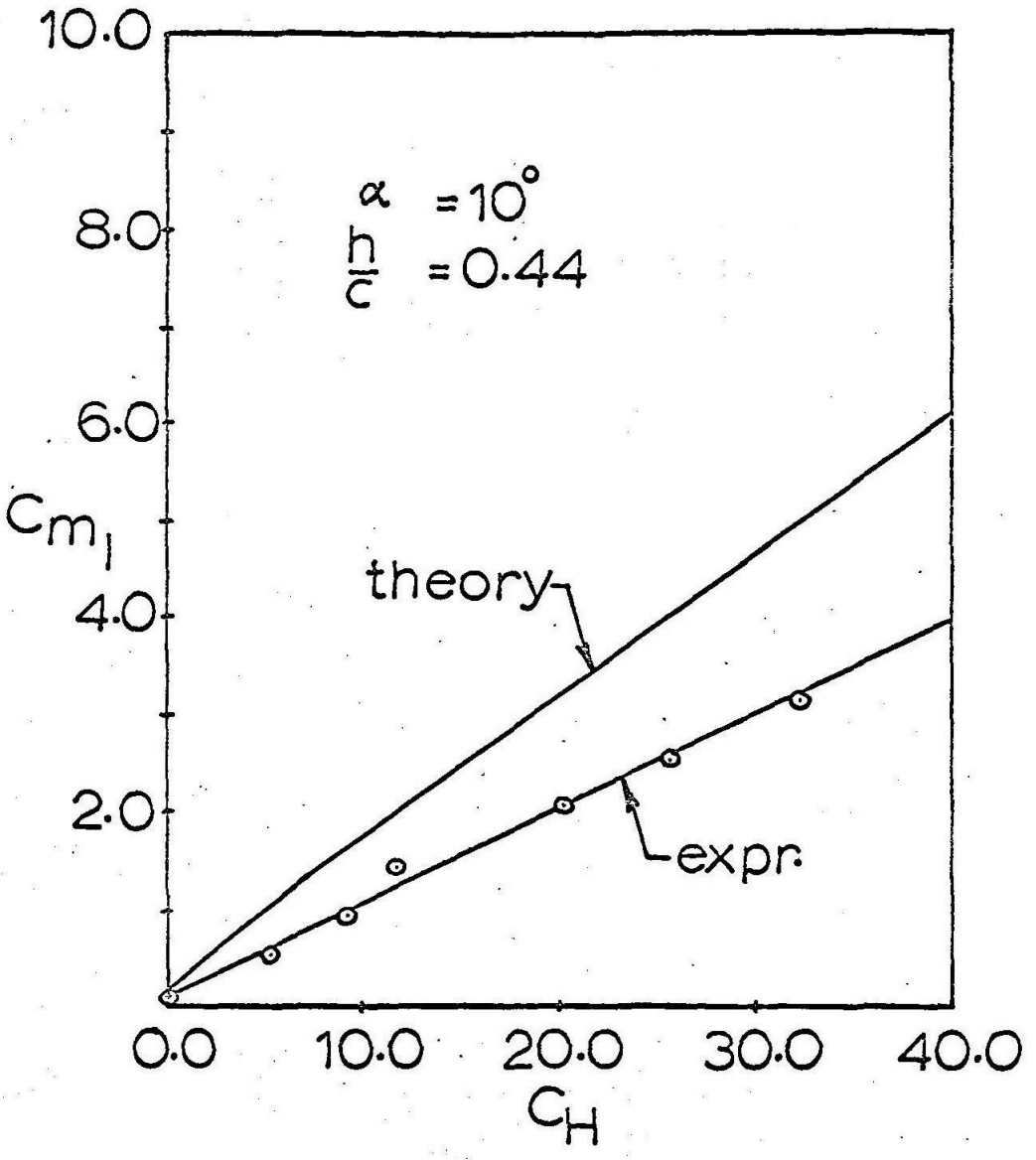

figure 37

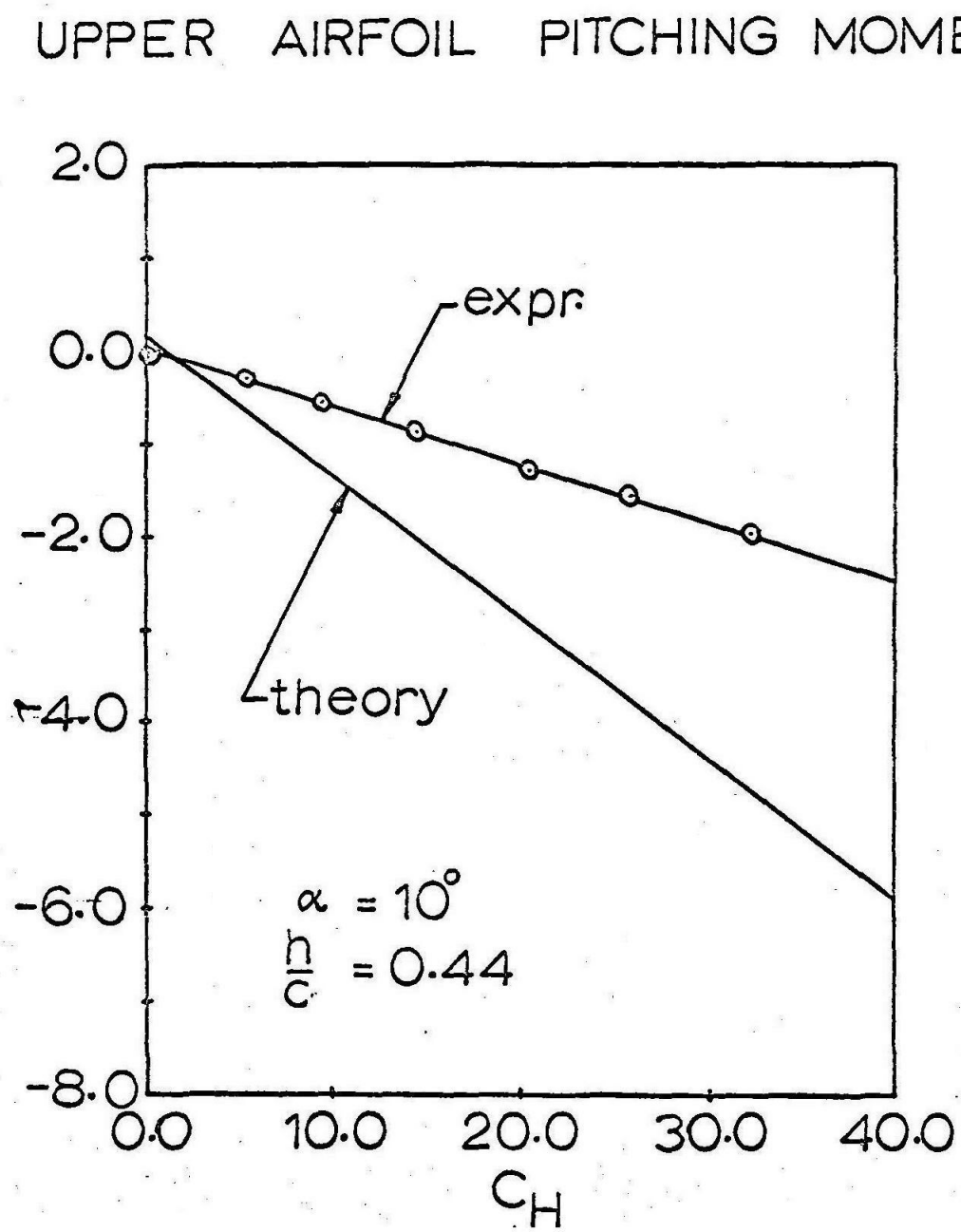
UPPER AIRFOIL PITCHING MOMENT
2.0
0.0
-2.0
-4.0
-6.0
-8.0
expr.
theory
α = 10°
h/c = 0.44
0.0
10.0
20.0
30.0
40.0
C_H

figure 38

TOTAL PITCHING MOMENT

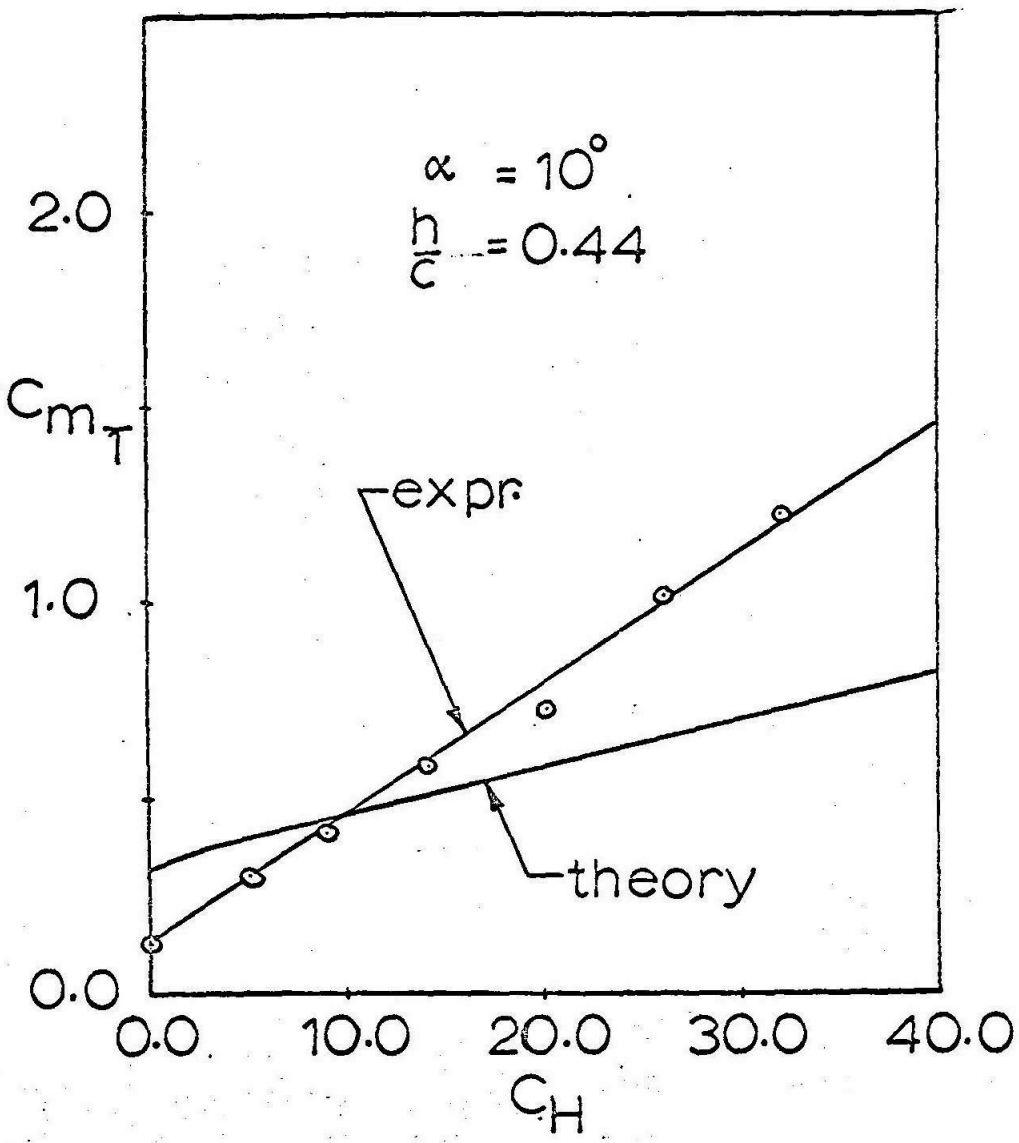

figure 39